

Vortex Sheet Simulations of 3D Flows Using an Adaptive Triangular Panel/Particle Method

by
Hualong Feng

A dissertation submitted in partial fulfillment
of the requirements for the degree of
Doctor of Philosophy
(Mathematics)
in The University of Michigan
2007

Doctoral Committee:

Professor Robert Krasny, Chair
Professor Werner J.A. Dahm
Professor Smadar Karni
Professor Sijue Wu

ACKNOWLEDGEMENTS

I would like to thank my advisor Robert Krasny, without whom this thesis would never have been possible. The highest standard he always sets for himself has been inspiring me over all these years. Beside the knowledge he has taught me, I am particularly grateful for his enormous patience and encouragement during many periods when no progress in was made. I look forward to working with him in the future.

I would also like to thank Professor Smadar Karni for being my second thesis reader, and Professor Werner Dahm and Professor Sijue Wu for agreeing to sit on my thesis committee. I am grateful to Professor August Evrard for letting me use their computer cluster to perform the computations. The staff in the graduate office of mathematics has been of tremendous help in non-academic affairs and I appreciate their assistance.

I have been fortunate to know some good friends in Ann Arbor. I am appreciative to their friendship and hope that it will continue. Last, I would like to thank my family for their emotional support during this seemingly unending project.

TABLE OF CONTENTS

ACKNOWLEDGEMENTS	ii
LIST OF FIGURES	v
CHAPTER	
I. Introduction	1
1.1 Motivation for Thesis	1
1.1.1 Vortex Sheets	2
1.1.2 Vortex Rings	3
1.2 Outline of Thesis	6
II. Mathematical Description and Previous Work	8
2.1 Euler Equations	8
2.2 Vortex Methods in General	10
2.2.1 Lagrangian Methods	10
2.2.2 Vortex-in-Cell Method	10
2.3 Vortex Sheets	11
2.4 Baroclinic Generation of Vorticity	13
2.4.1 Boussinesq Approximation	14
2.4.2 Full Density Jump	16
2.5 Previous Computational Work on Vortex Sheets	17
2.5.1 Two Dimensional Flow	17
2.5.2 Axisymmetric Flow	18
2.5.3 Three Dimensional Flow	19
III. Vortex Sheets in Two Dimensional and Axisymmetric Flow	21
3.1 Two Dimensional Flow	21
3.1.1 2D Euler Equations and Vortex Sheets in 2D Flow	21
3.1.2 Discretization and Numerical Methods for 2D Vortex Sheet Flow	23
3.1.3 Computational Results for 2D Vortex Sheets	27
3.2 Axisymmetric Flow	29
IV. Vortex Sheets in Three Dimensional Flow	36
4.1 Previous Work on Computations of 3D Vortex Sheets	36
4.1.1 Representation of 3D Vortex Sheets	37
4.1.2 Review of Previous Computational Work	39
4.2 Discretization and Quadrature Developed in This Thesis	42
4.2.1 Computation of Vorticity Carried by Panels	42
4.2.2 Data Structure and Evaluation of the Biot-Savart Integral	45

4.3	Adaptive Refinement	46
4.3.1	Barycentric Coordinates	47
4.3.2	Adaptive Panel Subdivision and Particle Insertion	48
4.4	Tree-code for Evaluating the Sheet Velocity	52
V. Vortex Ring Computations		56
5.1	Experiments on a Single Vortex Ring	56
5.2	Computational Results on Vortex Ring Azimuthal Instability	58
5.3	Experiments on Oblique Collision of Two Vortex Rings	66
5.4	Computational Results on Oblique Collision of Two Vortex Rings	69
VI. Vortex Sheet Computations in 3D Density-Stratified Flow		72
6.1	Review of Previous Work on Density-Stratified Flows	72
6.1.1	Rayleigh-Taylor Instability	73
6.1.2	Experimental Work on Density-Stratified Flow	73
6.2	Computational Results	75
VII. Summary and Future Work		79
7.1	Summary	79
7.1.1	Contributions of Thesis	80
7.1.2	Comparison with Previous Methods and Difficulties	81
7.2	Directions of Future Work	82
7.2.1	Higher Order Quadrature	83
7.2.2	Full Density Jump for Density-Stratified Flow in 3D	84
7.2.3	Head-on Collision of Two Vortex Rings	85
BIBLIOGRAPHY		87

LIST OF FIGURES

Figure

1.1	Schematic of a vortex sheet in an otherwise irrotational flow. The tangential component of the velocity has a jump $[\mathbf{u}] = \mathbf{u}_1 - \mathbf{u}_2$ across the sheet surface.	2
1.2	A propagating vortex ring. The vorticity is concentrated in the core and the vortex filaments are closed. Fluid particles rotate around the vortex core, while propagating perpendicular to the core at the same time, if viewed in a fixed reference frame.	3
1.3	A vortex ring forms as fluid is forced out of a circular pipe by a moving piston. A time sequence is shown. As fluid is forced out, a shear layer separates at the edge of the pipe and rolls up into a vortex ring.	4
1.4	A velocity jump is generated across a circular disk as it is given an impulse. Imagine that the disk dissolves, then the bound vortex sheet on it rolls up into a vortex ring.	5
1.5	Schematic of vortex ring formation as a drop of heavy fluid falls in a background of lighter fluid. Pictured is a time sequence of the experiment performed by Thomson and Newall [48].	5
2.1	A three dimensional vortex sheet, the circulation between A to B can be expressed in term of the jump in potential functions.	12
2.2	Schematic of a 2D vortex sheet (a) and its discretization using point vortices (b).	13
3.1	Comparison between (a) the trapezoid rule and (b) Simpson's rule. For the trapezoid rule, the integral of f on interval $[x_0, x_1]$ is approximated by the area of the trapezoid as pictured. For Simpson's rule, the formula is presented in (3.16).	25
3.2	Schematic depicting how point insertion is implemented. A new point is inserted if either $d_1 > \epsilon_1$ or $d_2 > \epsilon_2$. The solid points (\cdot) are existing computational points. The two circled points (\circ) are both candidates for a point to be inserted. l is obtained by a linear interpolant, while c is obtained by a cubic interpolant.	26
3.3	A cylinder of heavy fluid settles in a background of lighter fluid. Presented is a time sequence of $t = 0.0, 1.0, 2.0, 3.0, 4.0, 5.0$. Atwood ratio $A = 0.1$. Initial number of computational points $N = 40$. Initial radius $R = 0.5$. Smoothing parameter $\delta = 0.1$. Time step $\Delta t = 0.1$. Parameters for point-insertion criteria (3.17) $\epsilon_1 = 0.1$, (3.18) $\epsilon_2 = 0.0025$. We note that the terminal number of computational points $N = 352$	28

3.4	Comparison between schemes of different order of accuracy at terminal time $T = 5.0$ as shown in Figure 3.3. They use the same numerical parameters $R = 0.5, \delta = 0.1, \Delta t = 0.1$ as used in the computation presented in Figure 3.3. However, they use different initial number of computational points N , different point insertion parameters ϵ_1, ϵ_2 as printed in the plots. They each use different point insertion scheme or different integration scheme as printed in the sub-captions.	30
3.5	Comparison between the Boussinesq approximation (left) and full density jump(right). The Atwood ratio starts with $A = 0.25$ and reduces by a factor of 4 from each row to the next as printed in the picture, while the terminal time T doubles. It is evident that the results for the full density jump case tend to the results for the Boussinesq approximation case as A tends to 0. This also illustrates the scaling between A and T as shown in equations (3.36) and (3.37) in the Boussinesq approximation . . .	35
4.1	Schematic of a parameter space D and the corresponding physical space S . The sheet surface $\mathbf{x}(\alpha, \beta, t)$ defines a mapping from the parameter space (α, β) to the physical space (x, y, z) . Several vortex filaments are plotted.	37
4.2	Discretization of a circular vortex sheet into vortex filaments. Each filament is discretized using Lagrangian particles [34].	39
4.3	As the vortex sheet evolves, non-uniform stretching may cause two previously parallel vortex filaments to separate far at some point while stay close elsewhere. . . .	40
4.4	Discretization of a circular vortex sheet into quadrilateral panels. Each panel has 4, 5, or 6 (not shown) points [22].	41
4.5	A triangular panel with vertices $\mathbf{a}, \mathbf{b}, \mathbf{c}$. The vortex filaments through the vertices assist in the calculation of the vortex sheet strength γ on the panel \mathbf{abc}	43
4.6	A triangular panel consists of three active points a, b, c and three passive points d, e, f . The linear triangle formed by the active points assists in computation of the vorticity carried by the panel, while the quadratic triangle formed by all points assists in the refinement procedure to be described in the next section.	45
4.7	A triangle in the xy plane. Any point \mathbf{p} in the triangle can be uniquely expressed as a combination of the three vertices $\mathbf{a}, \mathbf{b}, \mathbf{c}$ using barycentric coordinates.	47
4.8	Barycentric space and physical space. On the left is a planar triangle with 6 points on them, labeled by their barycentric coordinates. On the right is the corresponding quadratic panel in the physical space.	49
4.9	Two criteria are checked in the refinement process. d_1 is the edge length. d_2 is the distance between an edge's midpoint and the associated passive point.	50
4.10	Panel subdivision and particle insertion. (a) It is decided that edge \mathbf{ac} will be split, then the panel \mathbf{abc} splits into four new panels and particle \mathbf{p} becomes active for some of the new panels. (b) puts panel \mathbf{abc} in the surrounding panels. Particle \mathbf{p} remains passive for panel \mathbf{acd} after the splitting and is plotted with a thick empty dot. Solid dots (\cdot) are active points. Empty dots (\circ) are passive points.	51
4.11	Tree formation. (a) physical tree in 2D space with four levels. (b) corresponding logical tree represented as a data structure.	53

5.1	Schematic of the experiment by Didden [14]. An axisymmetric vortex ring is generated by forcing fluid out of a pipe. A cross section of the ring is drawn. The ring radius grows like $R \sim t^{2/3}$. The axial distance X between the the vortex core and the pipe exit grows like $X \sim t^{3/2}$	57
5.2	Photo from Van Dyke [17] visualizing an experiment in which the azimuthal instability of a vortex ring is studied. The vortex ring was initially axisymmetric, then the azimuthal perturbations cause it to lose axisymmetry and become turbulent.	58
5.3	A Schematic of the conformal mapping $w(z) = e^z$ as applied to the generation of a triangular mesh on the unit disk. The physical mesh shown on the right is generated after one run of the refinement procedure described in section 4.3. More runs are needed if a finer mesh is desired.	59
5.4	Initial mesh generation by repetitively applying the refinement process. Three repetitions are shown.	60
5.5	Time sequence of azimuthal instability of a single vortex ring at time $t = 0, 1, 2, 3, 4, 5$, ordered top to bottom, then left to right. The perturbation has wave number $k = 5$. As can be seen in the picture, the perturbation does not grow much from $t = 0$ to $t = 5$	62
5.6	Final time $t = 5.0$ from the time sequence in Figure 5.5. (a) Mesh on the surface. (b) Transparent view. Two filaments are shown, the larger one is the outer edge, while the smaller one is inner edge after deleting a small center region in the initial mesh generation. The outer filament expanded by a large amount because circulation is concentrated there. In contrast, the inner filament did not expand much.	63
5.7	Time sequence of azimuthal instability of a single vortex ring at time $t = 0, 1, 2, 3, 4, 5$, ordered top to bottom, then left to right. The perturbation has wave number $k = 8$. As can be seen in the picture, the perturbation grows considerably from $t = 0$ to $t = 5$	64
5.8	Final time $t = 5.0$ from the time sequence in Figure 5.7. (a) Mesh on the surface. (b) Transparent view. Only the outer filament is shown to assist visualization in contrast to the case $k = 5$, the disk center is filled by adding computational points. As can be seen from the picture, hairpins form on the outer edge.	65
5.9	Schematic of experimental set-up for oblique collision of two vortex rings. θ is the collision angle. A top view is shown in (a). At an early time $t = t_e$, the two rings have little effect on each other and are axisymmetric. As the two rings come closer at a later time $t = t_l$, the axisymmetry is lost. A front view at the later time $t = t_l$ is shown in (b), where only the vortex core axes are drawn.	66
5.10	Schematic of two vortex rings colliding obliquely, front view. The dotted line denotes the bisecting plane between the two rings, the plane where collision occurs. As the two rings carrying opposite vorticity come close (a), the first vortex reconnection occurs (b) and they form one single ring (c). As time progresses further, a second reconnection occurs (d) and the single vortex ring splits into two counter rotating rings (e). Each new ring consists of one half from each of the original two rings.	67

5.11	Flow visualization by Lim [30]. Two vortex rings are generated as fluid is forced out of circular pipes. The pipe axes are positioned so that the collision angle $\theta = 17.5^\circ$. The two rings eventually collide and then reconnect to form two new rings propagating in different planes.	68
5.12	Time sequence of simulation of oblique collision of two vortex rings at time $t = 0, 8, 12, 16, 20, 24$, ordered top to bottom, then left to right.	70
5.13	Oblique collision of two vortex rings.	71
6.1	Schematic of an unstable vortex ring from the experiment by Thomson and Newall [48], picture taken from Walther and Koumoutsakos [50]. A drop of heavy fluid is released into water. The drop rolls up into a vortex ring which becomes unstable at a later time and secondary rings form. Only the vortex core is drawn. A time sequence is shown, ordered from top to bottom, and from left to right.	74
6.2	Visualization of the experiment by Estevadeordal et al. [18]. A drop of water suspension of polystyrene is released into water and a time sequence is shown. The drop rolls up into a vortex ring which later develops azimuthal instability and secondary rings form.	75
6.3	Initial mesh on a sphere. Two views are shown, perspective view on the left and top view on the right. The mesh is generated by the advancing front-method which uses the equator as the initial front.	76
6.4	Time sequence of simulation for a spherical drop of heavy fluid settling in a background of lighter fluid using the vortex sheet model. The plotted times are $t = 0, 2, 3, 4, 5, 6$, ordered from top to bottom, then from left to right. An initial perturbation of wave number $k = 5$ is added. The initial spherical drop rolls up into a vortex ring but mode $k = 5$ appears to be stable.	78
7.1	Difficulties in resolving 3D vortex sheets. (a) shows a case in which the sheet is stretched with different rates in different directions, resulting in a slender triangle. (b) shows two filaments that are almost parallel initially, but they may twist around each other at a later time.	82
7.2	Schematic of 4 and 5-point panels. In the refinement process, we may not split a panels into 4 new panels immediately when criterion (4.24) or (4.25) is satisfied on any edge. But rather we can active a passive point when the criterion is satisfied on the corresponding edge. New quadrature schemes need to be derived for 4-point panel (b) and 5-point panel (c).	84
7.3	A panel with three active points and four passive points. The extra passive point corresponds to the centroid of the triangle determined by the three active points.	85
7.4	Visualization of the experiment by Lim and Nickels [31]. In the experiment, two axisymmetric vortex rings are generated by forcing fluid out of circular tubes. The two rings stay axisymmetric initially, but the axisymmetry is lost as they come into contact. After the contact, the two core axes expand rapidly and smaller rings form on the outer edge.	85

CHAPTER I

Introduction

This chapter sketches the problems and introduces the work contained in the thesis. Section 1.1 explains the motivation for writing this thesis, and describes the vortex sheet model and vortex rings. Section 1.2 gives an outline of the thesis and lists the contributions made.

1.1 Motivation for Thesis

Fluid dynamics is important in both mathematics and engineering. In mathematics, the Navier-Stokes equation has been a driving force for new theories. In engineering, manufacturers have been able to make more fuel-efficient aircraft, owing to a profound understanding of fluid dynamics. Researchers study fluids using different methods, including experiments, numerical simulations, theoretical treatment and asymptotics. Numerical studies are presented in this thesis, and a vortex method is used. Recall that if $\mathbf{u}(\mathbf{x}, t)$ is the velocity, then vorticity is defined as

$$(1.1) \quad \boldsymbol{\omega}(\mathbf{x}, t) = \nabla \times \mathbf{u}(\mathbf{x}, t).$$

The vortex method is frequently used to simulate flows in which the vorticity is highly concentrated in space and viscous effects are small.

1.1.1 Vortex Sheets

For flow in which vorticity is concentrated on a surface, one can use the vortex sheet model [6]. A vortex sheet is a material surface in the flow across which the tangential component of the fluid velocity \mathbf{u} is discontinuous, and the jump in velocity reflects how strong the vortex sheet is, in a manner explained below. When using the vortex sheet model, it is often assumed that the flow is irrotational off the sheet, and hence the vorticity appears as a delta-function supported on the sheet surface. Since the flow is irrotational except on the sheet surface, there exist two potential functions $\phi_1(\mathbf{x}, t)$ and $\phi_2(\mathbf{x}, t)$ on the two sides of the sheet such that $\mathbf{u}_1 = \nabla\phi_1$ and $\mathbf{u}_2 = \nabla\phi_2$. See Figure 1.1 for a schematic. The vector-valued vortex sheet strength is $\boldsymbol{\gamma} = \mathbf{n} \times [\mathbf{u}]$, where $[\mathbf{u}] = \mathbf{u}_1 - \mathbf{u}_2$ is the jump in velocity across the sheet.

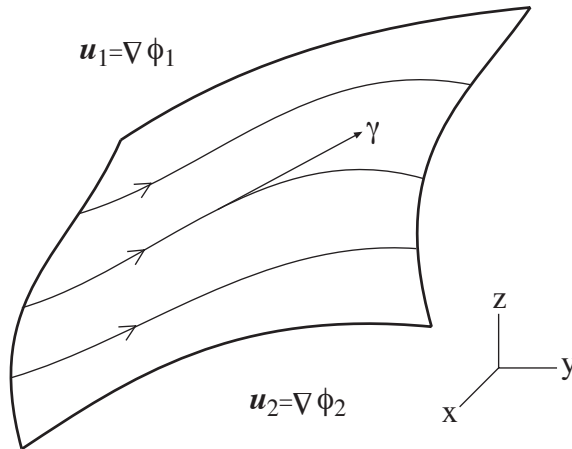


Figure 1.1: Schematic of a vortex sheet in an otherwise irrotational flow. The tangential component of the velocity has a jump $[\mathbf{u}] = \mathbf{u}_1 - \mathbf{u}_2$ across the sheet surface.

We note that the vortex sheet strength is tangent to the sheet surface, and that the normal component of the velocity is continuous across the sheet. The integral curves of the vortex sheet strength $\boldsymbol{\gamma}$ are called vortex filaments, so we can think of a vortex sheet as being formed by vortex filaments. Several vortex filaments are

depicted in Figure 1.1.

1.1.2 Vortex Rings

In this subsection we discuss examples of vortex ring formation and qualitatively explain their dynamics. Vortex rings are studied in Saffman [43] and are reviewed by Shariff and Leonard [45] and Lim and Nickels [32]. A vortex ring is a distribution of vorticity in which the vortex lines are closed curves and are concentrated in a closed tube. Figure 1.2 is the schematic of a vortex ring. This distribution of vorticity induces a velocity that causes the fluid to rotate around the core and propagates perpendicular to the plane determined by the core axis.

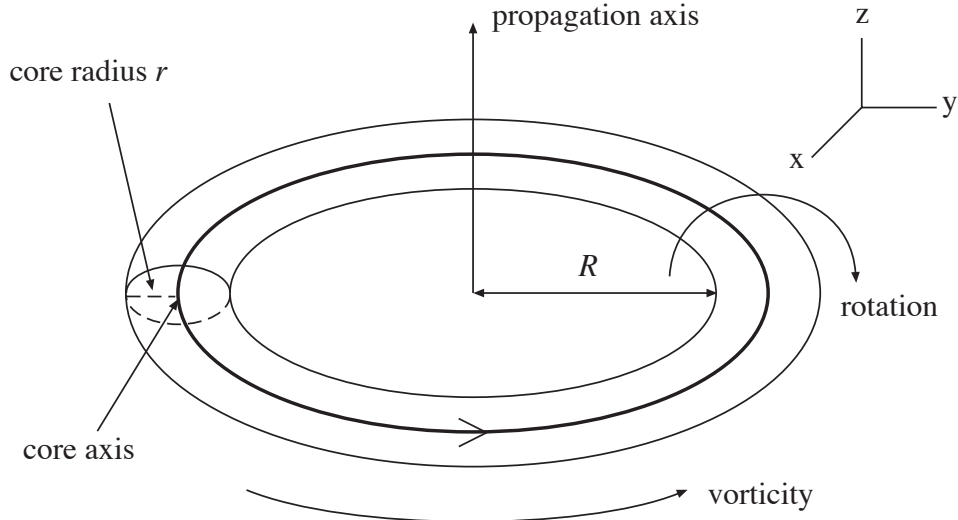


Figure 1.2: A propagating vortex ring. The vorticity is concentrated in the core and the vortex filaments are closed. Fluid particles rotate around the vortex core, while propagating perpendicular to the core at the same time, if viewed in a fixed reference frame.

Vortex rings often occur in high Reynolds number flow, and they can be simulated using vortex sheet model. We are interested in understanding the dynamics of vortex rings, including the stability properties, interaction between vortex rings, etc.

Vortex rings can be generated by forcing fluid out of a circular pipe as illustrated

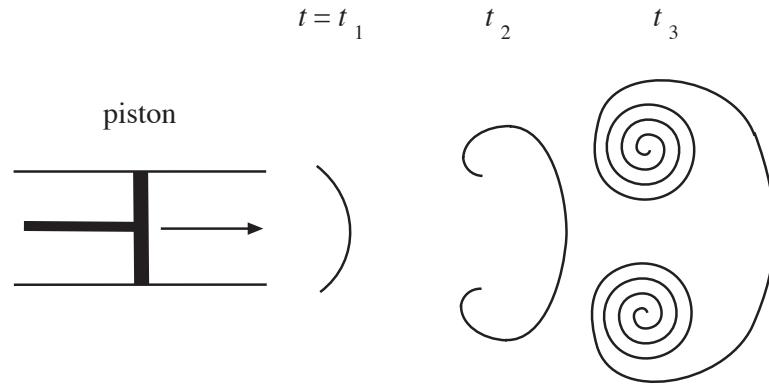


Figure 1.3: A vortex ring forms as fluid is forced out of a circular pipe by a moving piston. A time sequence is shown. As fluid is forced out, a shear layer separates at the edge of the pipe and rolls up into a vortex ring.

in Figure 1.3. This is a schematic of the experiments performed by Didden [14]. As the piston forces out fluid, a shear layer separates at the pipe opening and rolls up into a vortex ring. Nitsche and Krasny [37] reports numerical computations of this experiment, and their results agreed well the experiments.

While the piston/pipe apparatus is widely used to generate vortex rings, we can also look at vortex ring formation in a different way as contained in Taylor [47]. Consider a rigid circular disk in a uniform flow. The fluid approaches the flat disk on one side and it departs on the other side, as illustrated in Figure 1.4. A velocity jump exists across the disk and this is an example of a bound vortex sheet. Now imagine that the disk is dissolved, then the bound vortex sheet will roll up into a vortex ring. This is slightly different than the last approach in that the vorticity is generated instantly. The vortex sheet strength for this case will be explained in Chapter III when simulations are presented.

Another way to generate a vortex ring was put forward by Thomson and Newall [48]. They performed an experiment in which a drop of heavy fluid was released into water, and the drop was dyed to assist in visualization. As the drop settled in the

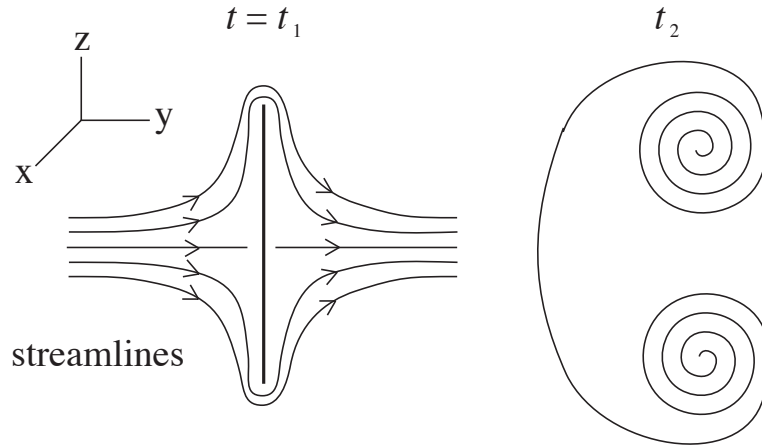


Figure 1.4: A velocity jump is generated across a circular disk as it is given an impulse. Imagine that the disk dissolves, then the bound vortex sheet on it rolls up into a vortex ring.

water, it rolled up and formed a descending vortex ring as depicted in Figure 1.5.

We note that this is still in an early stage of the whole process.

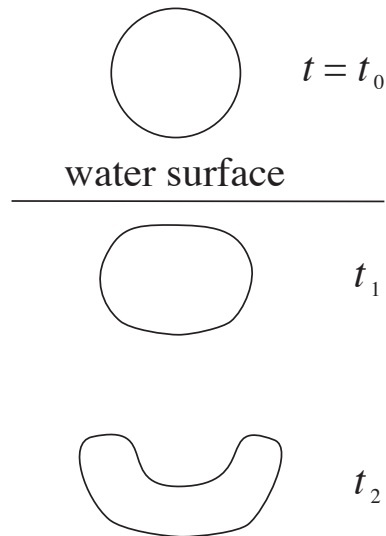


Figure 1.5: Schematic of vortex ring formation as a drop of heavy fluid falls in a background of lighter fluid. Pictured is a time sequence of the experiment performed by Thomson and Newall [48].

Since there is a density jump across the interface, vorticity is generated baroclinically on the interface. An equation governing the generation will be derived in Chapter II. The vortex sheet generated in this experiment is topologically a sphere, and it remains so if we assume that there is a well-defined interface between the two

fluids.

1.2 Outline of Thesis

This thesis addresses computational aspects of vortex sheet dynamics. The computations are motivated by experiments in the literature. A successful computational method must be accurate and efficient. One challenge faced by computational methods is that they are often used to simulate physically unstable problems, when extra caution is needed to make them effective.

Three main contributions are made in this thesis. First, a hierarchical triangular panel-particle representation was developed for vortex sheets. In general, the vortex sheet will stretch and distort as it evolves, so mesh refinement is needed to maintain resolution. The hierarchical panel structure makes the mesh refinement easier to implement, and also makes the code simpler, but still accurate. Second, a local intrinsic quadrature was successfully implemented. Previously, most methods for computing vortex sheets used a global parametric description of the sheet. In contrast to previous schemes that explicitly compute derivatives of the flow map with respect to the global parameters, the scheme developed here avoids the use of a global parameter space in both the quadrature and panel-particle refinement. The algorithm is thus simplified and also has the potential to resolve the sheet surface when the geometry becomes complicated at later times. Third, we made a comparison between the Boussinesq approximation and the full density jump. For density-stratified flow in 2D and axisymmetric case, we showed numerically that the formulation with a full density jump converged to the case when the Boussinesq approximation was made.

The thesis is organized as follows. Chapter I is a concise introduction to vortex

sheets and the work contained in this thesis. Chapter II contains the mathematical formulation of ideal fluids in general, and the mathematical ingredients in the concept of vortex sheets. This chapter also gives a brief review of the literature in computational fluid dynamics devoted to vortex sheets. Chapter III describes the numerical methods and presents results for two dimensional and axisymmetric vortex sheets. Though the focus of the thesis is on three dimensional vortex sheets, a good understanding of the simpler 2D and axisymmetric cases will help us gain insight into fully 3D flow. Chapter IV addresses the discretization of a 3D vortex sheet and the numerical methods to be used in later chapters. The tree-code for evaluating vortex sheet motion is briefly explained. We point out that there are two types of trees in the computational method, one deals with the hierarchical particle-panel formulation, and the other is used in the tree-code. Chapter V presents computational results of vortex rings, including cases in which a single vortex ring undergoes instability, and a case in which two vortex rings collide obliquely. We note that in both cases the vorticity is conserved. Chapter VI presents computational results for density-stratified flow, in which vorticity is generated baroclinically. Chapter VII contains the summary and proposes directions for future research.

CHAPTER II

Mathematical Description and Previous Work

In this chapter, the mathematical equations pertaining to this thesis will be explained in depth, and a brief review of previous work on vortex sheets in both 2D and 3D will be given. This chapter primarily describes equations in three dimensional space, but equations in two dimensional space are also discussed as necessary. This chapter starts in section 2.1 with an introduction to the incompressible Euler equations. This is followed by a review of the vortex methods in section 2.2. The vortex sheet model introduced in Chapter I is expanded upon in section 2.3. Section 2.4 derives equations governing the vorticity generation in density-stratified flow. Finally, a review of previous computational work on vortex sheets is given in section 2.5.

2.1 Euler Equations

In this section, we discuss the Euler equations of incompressible fluids. In three space dimensions, the Euler equations of an incompressible variable density flow are

$$(2.1) \quad \frac{\partial \rho}{\partial t} + \mathbf{u} \cdot \nabla \rho = 0,$$

$$(2.2) \quad \frac{\partial \mathbf{u}}{\partial t} + \mathbf{u} \cdot \nabla \mathbf{u} = -\nabla p + \rho \mathbf{F},$$

$$(2.3) \quad \nabla \cdot \mathbf{u} = 0,$$

where $t, \rho, \mathbf{u}, p, \mathbf{F}$ are the time, density, velocity, pressure, and the external force, respectively [11]. They are derived by assuming the conservation of mass, conservation of momentum, incompressibility, and that the flow is inviscid. The equations have to satisfy appropriate initial and boundary conditions, in particular, they have to satisfy the zero normal velocity boundary condition when solved in a bounded domain. The pressure appears explicitly, but it is often cumbersome to track the pressure, and now we show that this can be avoided by using the Euler equations in vorticity form.

There are many flows in which the vorticity is highly concentrated, for example, in the wake of an aircraft on takeoff. For such flows, it is beneficial to derive a system with vorticity as a primary variable. With $\boldsymbol{\omega} = \nabla \times \mathbf{u}$ denoting the vorticity and taking the curl of (2.2), we arrive at the Euler equations in vorticity form,

$$(2.4) \quad \frac{\partial \rho}{\partial t} + \mathbf{u} \cdot \nabla \rho = 0,$$

$$(2.5) \quad \frac{\partial \boldsymbol{\omega}}{\partial t} + (\mathbf{u} \cdot \nabla) \boldsymbol{\omega} = (\boldsymbol{\omega} \cdot \nabla) \mathbf{u} - \nabla \times (\rho \mathbf{F})$$

$$(2.6) \quad \nabla^2 \mathbf{u} = -\nabla \times \boldsymbol{\omega}.$$

Now the pressure term is not present, and the vorticity $\boldsymbol{\omega}$ becomes a primary variable. The velocity field \mathbf{u} can be obtained from vorticity $\boldsymbol{\omega}$ by solving the Poisson equation (2.6) using the Biot-Savart law:

$$(2.7) \quad \mathbf{u}(\mathbf{x}) = \int_V \mathbf{K}(\mathbf{x} - \tilde{\mathbf{x}}) \times \boldsymbol{\omega}(\tilde{\mathbf{x}}) d\tilde{\mathbf{x}}, \quad \mathbf{K}(\mathbf{x}) = -\frac{\mathbf{x}}{4\pi|\mathbf{x}|^3},$$

where V is the vorticity containing region and $\mathbf{K}(\mathbf{x})$ is the Biot-Savart kernel [6].

We note that $\mathbf{K}(\mathbf{x})$ is the gradient of the Newtonian potential

$$(2.8) \quad \mathbf{G}(\mathbf{x}) = -\frac{\mathbf{1}}{4\pi|\mathbf{x}|}, \quad \text{and so } \mathbf{K}(\mathbf{x}) = \nabla \mathbf{G}(\mathbf{x}).$$

2.2 Vortex Methods in General

As noted in the previous section, in an incompressible flow, the fluid velocity is related to the vorticity distribution through the Biot-Savart law (2.7). The last several decades have seen rapid growth of research in vortex dynamics and computational vortex methods. Saffman [43] is primarily concerned with theoretical vortex dynamics. Leonard [28, 29] are review papers devoted to computational vortex methods. The book of Cottet and Koumoutsakos [12] addresses both vortex dynamics in general and computational methods. In this section, we briefly review those aspects of vortex methods that are relevant to our work.

2.2.1 Lagrangian Methods

Rosenhead [42] was a pioneering contribution in vortex methods. He used point vortices and studied vortex generation from a surface of discontinuity. Since vortex methods are based on the Lagrangian description of the fluid equations, one of the difficulties faced by vortex methods is to incorporate viscous effects accurately and efficiently in a grid-free setting. One solution was put forward by Chorin [9] in which he simulated the viscous effect by letting each vortex undergo a random walk. The step size of the random walk depends on the kinetic viscosity coefficient.

2.2.2 Vortex-in-Cell Method

The vortex-in-cell method (VIC) is a hybrid approach which combines both Eulerian methods and Lagrangian methods. The VIC method is one of the major approaches currently used in vortex simulations. In a VIC method, both a regular Eulerian grid and a grid-free Lagrangian particle distribution are used. The grid is

used to compute the velocity using a fast Poisson solver, and the particle distribution is used to account for the convection of vorticity. In a VIC implementation, quantities are interpolated back and forth between the grid and the Lagrangian particles. This process in general introduces dissipation effects faced by many Eulerian methods and the extent of this problem depends on the interpolation schemes used.

2.3 Vortex Sheets

This section contains a detailed description of the vortex sheet model and relevant formulae. For cases where the vorticity is concentrated in a thin layer, we can idealize the flow by letting the layer thickness ϵ go to zero and vorticity $\boldsymbol{\omega}$ go to infinity in a manner that keeps $\epsilon\boldsymbol{\omega}$ constant. This process yields the vortex sheet model and $\boldsymbol{\gamma} = \epsilon\boldsymbol{\omega}$ is the vortex sheet strength [6]. This singular distribution of vorticity is a delta-function supported on the sheet. The vorticity lies tangent to the surface and is given by $\boldsymbol{\gamma}\delta(n)$, where n is the normal distance to the surface and δ is the delta-function. As noted in Chapter I, the vortex sheet strength is also given by $\boldsymbol{\gamma} = \mathbf{n} \times [\mathbf{u}]$, where \mathbf{n} is the unit normal vector and $[\mathbf{u}] = \mathbf{u}^+ - \mathbf{u}^-$ is the velocity jump across the sheet [6].

With the vortex sheet model, the Biot-Savart law (2.7) reduces to a surface integral,

$$(2.9) \quad \frac{\partial \mathbf{x}}{\partial t} = \int_S \mathbf{K}(\mathbf{x} - \tilde{\mathbf{x}}) \times \boldsymbol{\gamma} dS, \quad \mathbf{K}(\mathbf{x}) = -\frac{\mathbf{x}}{4\pi|\mathbf{x}|^3},$$

where dS is an area element on the sheet S . Because of stability considerations, the following regularized kernel $\mathbf{K}_\delta(\mathbf{x})$ is used in the numerical computations,

$$(2.10) \quad \mathbf{K}_\delta(\mathbf{x}) = -\frac{\mathbf{x}}{4\pi(|\mathbf{x}|^2 + \delta^2)^{\frac{3}{2}}},$$

where δ controls how much the vorticity is smeared out [10].

Using Lagrangian variable $\boldsymbol{\alpha}$ to parametrize the vortex sheet, we have the flow map $\boldsymbol{x} = \boldsymbol{x}(\boldsymbol{\alpha}, t)$ and the vortex sheet strength $\boldsymbol{\gamma} = \boldsymbol{\gamma}(\boldsymbol{\alpha}, t)$. Related to the vectorial sheet strength $\boldsymbol{\gamma}$, another important variable is the scalar circulation $\Gamma(\boldsymbol{\alpha}, t)$. Here we follow the treatment by Brady, Leonard, and Pullin [7] to explain Γ . The circulation Γ_{AB}^C around a closed path $C = C_1 \cup C_2$ piercing the sheet through A and B , as shown in Figure 2.1, can be computed as follows,

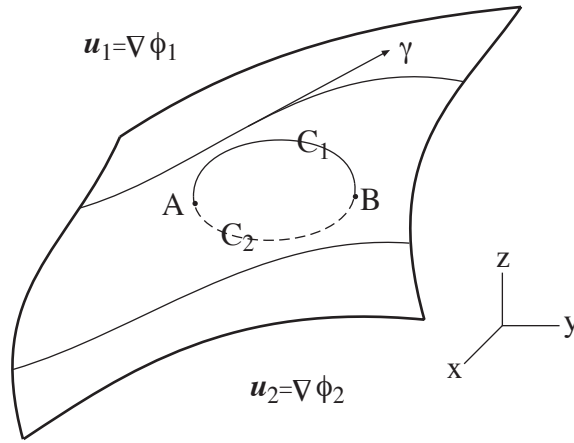


Figure 2.1: A three dimensional vortex sheet, the circulation between A to B can be expressed in term of the jump in potential functions.

$$\begin{aligned}
 (2.11) \quad \Gamma_{AB}^C &= \int_C \mathbf{u} \cdot d\mathbf{s} = \int_{C_1} \mathbf{u} \cdot d\mathbf{s} + \int_{C_2} \mathbf{u} \cdot d\mathbf{s} \\
 &= \phi_1(A) - \phi_1(B) + \phi_2(B) - \phi_2(A) = [\phi](A) - [\phi](B),
 \end{aligned}$$

where $d\mathbf{s}$ is an arc element on the curve C . Equation (2.11) will be referred to later in the thesis. Γ_{AB}^C is independent of the path C chosen because the flow is irrotational off the sheet, and hence we will just denote it by Γ_{AB} . With A as a base point, we define $\Gamma(\boldsymbol{\alpha}, t) = \Gamma_{\boldsymbol{\alpha}A} = [\phi](\boldsymbol{\alpha}) - [\phi](A)$. Since ϕ_1 and ϕ_2 are potential functions and hence can be modified by a constant, we can assume $[\phi](A) = 0$ and so we have

$$(2.12) \quad \Gamma(\boldsymbol{\alpha}, t) = [\phi](\boldsymbol{\alpha}, t).$$

In other words, circulation equals the jump in potential function across the sheet.

Recall that vortex filaments on the sheet surface are integral curve of the vortex sheet strength γ as described in Chapter I. We note that points on a vortex filament have the same Γ value. In computations of 3D flow it is sometimes convenient to discretize a vortex sheet using vortex filaments.

When flow quantities only depend on two of the three spatial dimensions, we have a 2D flow. Vorticity in a 2D flow only has one non-zero component, hence a vortex sheet in a 2D flow has straight vortex filaments extending to infinity. To illustrate, in Figure 2.2 we draw a schematic of a 2D vortex sheet and its discretization using point vortices. Figure 2.2(a) is a continuous sheet of those filaments, while each dot in Figure 2.2(b) represents a filament.

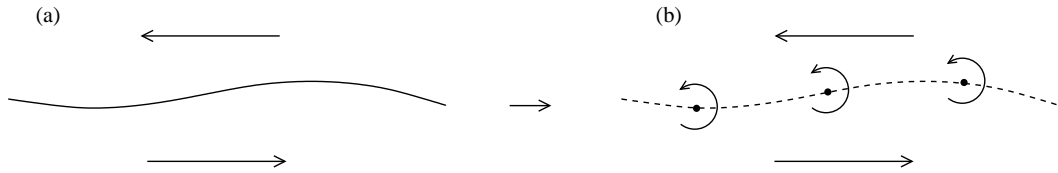


Figure 2.2: Schematic of a 2D vortex sheet (a) and its discretization using point vortices (b).

2.4 Baroclinic Generation of Vorticity

We point out that circulation and vorticity are used interchangeably in this thesis. In homogeneous flow, vorticity is conserved at material points. Referring to equation (2.12), this means that the circulation $\Gamma(\boldsymbol{\alpha}, t)$ does not depend on t . One example we will simulate is a flow with density stratification, in which $\Gamma(\boldsymbol{\alpha}, t)$ is not conserved. Vorticity is generated baroclinically on the interface between the two fluids, and the interface is simulated using the vortex sheet model. Now we derive the equations governing the generation of vorticity on the interface. First, we make the Boussinesq approximation and derive an equation in subsection 2.4.1. We follow Anderson [1]

for this case. The equation for the case of a full density jump is derived in subsection 2.4.2. We follow Baker, Meiron and Orszag [3] for this case.

2.4.1 Boussinesq Approximation

Assume that the densities ρ_1 and ρ_2 are uniform on each side of the interface, and assume that the density jump is small in the sense that the non-dimensional Atwood ratio

$$(2.13) \quad A = \frac{\rho_1 - \rho_2}{\rho_1 + \rho_2}$$

is small. The Boussinesq approximation can be made in this case, and this simplifies the problem as explained below.

Because the flow is irrotational off the interface, there exist potential functions ϕ_1 and ϕ_2 on each side such that $\mathbf{u}_1 = \nabla\phi_1$ and $\mathbf{u}_2 = \nabla\phi_2$. Bernoulli's theorem can be applied to yield

$$(2.14) \quad \rho_1 \frac{\partial\phi_1}{\partial t} + \rho_1 \frac{|\mathbf{u}_1|^2}{2} = -p + \rho_1 gz,$$

$$(2.15) \quad \rho_2 \frac{\partial\phi_2}{\partial t} + \rho_2 \frac{|\mathbf{u}_2|^2}{2} = -p + \rho_2 gz$$

on each side of the interface, where g is gravity and z is the vertical component in the spatial variable $\mathbf{x} = (x, y, z)$. Choosing $\rho = (\rho_1 + \rho_2)/2$ as the scale for density, we divide both equations (2.14) and (2.15) by ρ to non-dimensionalize the density,

$$(2.16) \quad \frac{\rho_1}{\rho} \frac{\partial\phi_1}{\partial t} + \frac{\rho_1}{\rho} \frac{|\mathbf{u}_1|^2}{2} = -\frac{p}{\rho} + \frac{\rho_1}{\rho} gz,$$

$$(2.17) \quad \frac{\rho_2}{\rho} \frac{\partial\phi_2}{\partial t} + \frac{\rho_2}{\rho} \frac{|\mathbf{u}_2|^2}{2} = -\frac{p}{\rho} + \frac{\rho_2}{\rho} gz.$$

Since the density jump is small, ρ_1 and ρ_2 are close to ρ . The Boussinesq approximation is made by setting the non-dimensional density on the left side equal to

unity,

$$(2.18) \quad \frac{\partial \phi_1}{\partial t} + \frac{|\mathbf{u}_1|^2}{2} = -\frac{p}{\rho} + \frac{\rho_1}{\rho}gz,$$

$$(2.19) \quad \frac{\partial \phi_2}{\partial t} + \frac{|\mathbf{u}_2|^2}{2} = -\frac{p}{\rho} + \frac{\rho_2}{\rho}gz.$$

Let the density interface be $\mathbf{x} = \mathbf{x}(\boldsymbol{\alpha}, t)$, and recall from section 2.3 that circulation $\Gamma(\boldsymbol{\alpha}, t) = \phi_1(\mathbf{x}(\boldsymbol{\alpha}, t), t) - \phi_2(\mathbf{x}(\boldsymbol{\alpha}, t), t)$ is simply the jump in potential across the interface. Let $\mathbf{u} = \mathbf{u}(\mathbf{x}(\boldsymbol{\alpha}, t), t)$ be the velocity of the interface, then the time derivative of Γ is,

$$(2.20) \quad \begin{aligned} \frac{\partial \Gamma}{\partial t} &= (\mathbf{u} \cdot \nabla \phi_1 + \frac{\partial \phi_1}{\partial t}) - (\mathbf{u} \cdot \nabla \phi_2 + \frac{\partial \phi_2}{\partial t}) \\ &= (\mathbf{u} \cdot \nabla \phi_1 - \mathbf{u} \cdot \nabla \phi_2) + (\frac{\partial \phi_1}{\partial t} - \frac{\partial \phi_2}{\partial t}), \end{aligned}$$

Since \mathbf{u}_1 and \mathbf{u}_2 are the limiting velocities on each side of the interface, it is reasonable to assume that the interface moves at the average velocity $\mathbf{u} = (\mathbf{u}_1 + \mathbf{u}_2)/2$. With this assumption, equation (2.20) becomes

$$(2.21) \quad \begin{aligned} \frac{\partial \Gamma}{\partial t} &= \frac{(\mathbf{u}_1 + \mathbf{u}_2) \cdot (\mathbf{u}_1 - \mathbf{u}_2)}{2} + (\frac{\partial \phi_1}{\partial t} - \frac{\partial \phi_2}{\partial t}) \\ &= \frac{|\mathbf{u}_1|^2}{2} - \frac{|\mathbf{u}_2|^2}{2} + (\frac{\partial \phi_1}{\partial t} - \frac{\partial \phi_2}{\partial t}) \\ &= \left[\frac{\partial \phi}{\partial t} \right] + \left[\frac{|\mathbf{u}|^2}{2} \right] = \frac{\rho_1 - \rho_2}{\rho}gz = 2Agz, \end{aligned}$$

where the last equality comes from taking the difference between equations (2.18) and (2.19). We note that equation (2.21) can be simplified as

$$(2.22) \quad \frac{\partial \Gamma}{\partial t} = -2Agz.$$

2.4.2 Full Density Jump

For large density jump, the Boussinesq approximation is not valid, and a different equation for vorticity generation needs to be derived. The derivation is similar to the case when the Boussinesq approximation was made. We take (2.14) and (2.15) and divide them by each density to obtain

$$(2.23) \quad \frac{\partial \phi_1}{\partial t} + \frac{|\mathbf{u}_1|^2}{2} = -\frac{p}{\rho_1} + gz,$$

$$(2.24) \quad \frac{\partial \phi_2}{\partial t} + \frac{|\mathbf{u}_2|^2}{2} = -\frac{p}{\rho_2} + gz.$$

Taking the difference between (2.23) and (2.24), we obtain

$$(2.25) \quad \frac{\partial \Gamma}{\partial t} = -\frac{\rho_2 - \rho_1}{\rho_1 \rho_2} p,$$

Defining the average potential $\phi = (\phi_1 + \phi_2)/2$ and taking the sum of (2.23) and (2.24), we obtain

$$(2.26) \quad 2\frac{\partial \phi}{\partial t} + |\mathbf{u}|^2 = -\frac{1}{4}\gamma^2 - \frac{\rho_1 + \rho_2}{\rho_1 \rho_2} p + 2gz,$$

where $\mathbf{u} = (\mathbf{u}_1 + \mathbf{u}_2)/2$ and the vortex sheet strength γ is the arc length derivative of circulation Γ ,

$$(2.27) \quad \gamma = \frac{d\Gamma}{ds}.$$

Now, we use equations (2.25) and (2.26) to eliminate the pressure term p to obtain

$$(2.28) \quad \frac{\partial \Gamma}{\partial t} = -2A\left(\frac{\partial \phi}{\partial t} - \frac{1}{2}|\mathbf{u}|^2 + \frac{1}{8}\gamma^2 + gz\right).$$

Γ and ϕ are related as follows. The density interface is a layer of doublets of strength Γ , hence the average potential ϕ is given by a surface integral of Γ over the interface,

$$(2.29) \quad \phi = \iint \Gamma \frac{\partial G}{\partial \mathbf{n}} dS,$$

where $\partial G/\partial \mathbf{n}$ is the normal derivative of the Newtonian potential

$$(2.30) \quad G(\mathbf{x} - \tilde{\mathbf{x}}) = \frac{1}{4\pi} \frac{1}{|\mathbf{x} - \tilde{\mathbf{x}}|}.$$

(2.28) and (2.29) are combined to give an implicit equation for the baroclinic generation of circulation Γ on the density interface,

$$(2.31) \quad \frac{\partial \Gamma}{\partial t} = -2A \left(\frac{\partial}{\partial t} \int \int \Gamma \frac{\partial G}{\partial \mathbf{n}} dS - \frac{1}{2} \mathbf{u} \cdot \mathbf{u} + \frac{1}{8} \gamma^2 + gz \right).$$

This equation will be solved using an iterative method and the numerical methods will be described in Chapter III.

2.5 Previous Computational Work on Vortex Sheets

The concept of vortex sheets has been in existence for more than a century, yet there are still many related questions that need answers. The following review of previous work on vortex sheets focuses on the computational aspects.

2.5.1 Two Dimensional Flow

Much has been done on vortex sheets in two dimensional flow and only the portion pertaining to this thesis is reviewed here. Rosenhead [42] performed the first numerical computation of vortex sheets in a 2D flow. He used point vortices and manually did a calculation using several point vortices. Moore [35] showed that a singularity forms at in finite time, the reason being that the growth rate of modes becomes unbounded as the wave number goes to infinity for a vortex sheet model. The nature of the singularity was that the curvature became unbounded in finite time.

Intensive computations of vortex sheets became possible with computers. However, not much was known about the behavior of vortex sheets beyond the critical time when a singularity forms. Krasny [26] used vortex blobs to smooth the vorticity field and was able to compute the evolution of a 2D vortex sheet past the critical time. He also presented numerical evidence showing that without roundoff error, the evolution of an analytic vortex sheet converges as the smoothing parameter δ goes to 0, even beyond the critical time. However, Krasny and Nitsche [27] presented numerical evidence showing that chaos may develop at later times as the sheet evolves, and computations are conducted in both 2D and axisymmetric flows. A computation using Eulerian method was performed by Tryggvason, Dahm, and Sbeih [49], showing that the result agrees well with the vortex blob method by Krasny [26].

Making the Boussinesq approximation, Anderson [1] computed a rising plume. A cylinder of light fluid is immersed in a heavy surrounding fluid, and he computed the evolution of the cylinder numerically. Baker, Meiron, and Orszag [3] studied the stability of surface waves in a two-phase density-stratified flow. They derived the equations governing the vorticity generation on a density interface separating two fluids, as shown in equation (2.31), without making the Boussinesq approximation.

2.5.2 Axisymmetric Flow

In the cylindrical coordinate system (r, θ, z) , a flow is called axisymmetric if the flow quantities do not depend on θ . Axisymmetric flow has some three dimensional features but it remains in a simple form and can be more easily studied than fully 3D flow, and it is also less costly to compute. The computation of vortex sheets in an axisymmetric flow involves line integrals along circles, which can be re-formulated in terms of elliptic integrals. Since there is a simple recursive algorithm for evalu-

ating elliptic integrals, the computational cost can be significantly reduced. Nitsche and Krasny [37] presented both numerical methods and results for vortex sheets in axisymmetric flow. In one of their computations, they simulated the vortex sheet formed at the edge of a circular pipe as fluid is forced out as was illustrated in Figure 1.3.

2.5.3 Three Dimensional Flow

There is increasing interest in computing three dimensional vortex sheet flow. Pozrikidis [41] used a triangular mesh and an advancing-front method. The focus was on making the advancing-front method stable in generating a new mesh after each time step. Computational results were presented of a self-pinching vortex sheet. A triangular mesh was also used by Brady, Leonard, and Pullin [7], in which the main focus was on remeshing the vortex sheet so each triangle on the sheet surface remains as close to equilateral as possible after each time step. They used Bezier patches defined over a global parameter space as interpolants in the remeshing procedure. Lindsay and Krasny [34] developed a fast tree-code to evaluate the velocities of points on a 3D vortex sheet, reducing the computational cost from the traditional $O(N^2)$ to $O(N\log N)$. In [34], the vortex sheet was discretized using vortex filaments, and a new filament was added when two adjacent ones separated too far. In contrast to the work in Lindsay and Krasny [34], Kagnovskiy [22] introduced a quadrilateral panel method for both the quadrature and the refinement schemes. An entire filament did not have to be added for refinement. The panel method reduced the computational cost further, because it adds points only where needed. Extending the work by Dahm, Scheil, and Tryggvason [13], Stock [46] implemented a vortex-in-cell method to study a vortex ring hitting a density interface, among other problems. The above

is only a brief introduction to computations of 3D vortex sheets, in Chapter IV we will point out the similarities and differences between these prior methods and the method developed in this thesis.

CHAPTER III

Vortex Sheets in Two Dimensional and Axisymmetric Flow

In this chapter, the computational method for vortex sheets in two dimensional and axisymmetric flow is described in detail and results are presented. The computational cost of vortex sheets in 2D and axisymmetric flow is much lower than in fully 3D flow, and an $O(N^2)$ direct summation algorithm is often sufficient. Section 3.1 describes the numerical methods and results of vortex sheets in 2D flow, while section 3.2 treats axisymmetric vortex sheet flow.

3.1 Two Dimensional Flow

In some flows, for example, a thin layer of soap in the plane $z = 0$, we can assume that the flow properties depend only on x and y . 2D flow is important in various applications. For instance, the atmosphere on a global scale is a locally 2D flow since its thickness is small compared to the radius of the earth. Moreover, studying 2D flow in detail is a step towards better understanding of 3D flow.

3.1.1 2D Euler Equations and Vortex Sheets in 2D Flow

Consider the following 2D version of the Euler equations (2.1) – (2.3),

$$(3.1) \quad \frac{\partial \rho}{\partial t} + \mathbf{u} \cdot \nabla \rho = 0,$$

$$(3.2) \quad \frac{\partial \mathbf{u}}{\partial t} + \mathbf{u} \cdot \nabla \mathbf{u} = -\nabla p + \rho \mathbf{F},$$

$$(3.3) \quad \nabla \cdot \mathbf{u} = 0,$$

where now $\mathbf{u} = \mathbf{u}(x, y, t)$ has only two components. In a 2D flow, the vorticity $\boldsymbol{\omega} = (0, 0, \omega_3)$ only has one non-zero component and will be denoted ω in this chapter since it is essentially a scalar. The velocity satisfies the no-penetration boundary condition if solved in a bounded domain. If the vorticity is concentrated in some region, it is convenient to work with the Euler equations in vorticity form:

$$(3.4) \quad \frac{\partial \rho}{\partial t} + \mathbf{u} \cdot \nabla \rho = 0,$$

$$(3.5) \quad \frac{\partial \omega}{\partial t} + (\mathbf{u} \cdot \nabla) \omega = -\nabla \times (\rho \mathbf{F}),$$

$$(3.6) \quad \nabla^2 \psi = -\omega, \quad u = \psi_y, \quad v = -\psi_x,$$

where ∇^2 is the Laplace operator and ψ is the stream function.

This system may be solved with an Eulerian method, and in this case, the computational domain is discretized using a fixed and usually uniform grid. The stream function ψ is obtained by solving the Poisson equation $\nabla^2 \psi = -\omega$ in (3.6), and the stream function is differentiated to obtain the velocity \mathbf{u} , which is in turn used to advect both density ρ in (3.4) and vorticity ω in (3.5). Appropriate boundary conditions have to be enforced.

If a Lagrangian method is used to solve the system in free space, the stream function ψ can be obtained using the Green's function,

$$(3.7) \quad \psi = -G * \omega, \quad G = \frac{1}{2\pi} \log \sqrt{x^2 + y^2},$$

where $*$ denotes convolution and G is the Green's function for the 2D Laplace oper-

ator. Then, (3.6) implies that

$$(3.8) \quad u = -\frac{\partial G}{\partial y} * \omega, \quad v = \frac{\partial G}{\partial x} * \omega,$$

which can be written more compactly,

$$(3.9) \quad \mathbf{u} = (u, v) = \mathbf{K} * \omega,$$

where

$$(3.10) \quad \mathbf{K} = \frac{(-y, x)}{2\pi r^2}, \quad r^2 = x^2 + y^2.$$

With this formulation, a Lagrangian method can be implemented in a grid-free setting.

For a 2D flow, the vortex sheet is a curve in the xy plane and the vorticity is a delta function supported on the curve. The normal component of velocity is continuous across the vortex sheet but the tangential component is discontinuous.

In applications, one may consider both bounded and unbounded vortex sheets. In the latter case, a commonly studied example is a spatially periodic vortex sheet. In 2D, we can use the complex notation $z = x + iy$ for convenience. Assume that the flow is homogeneous so that vorticity is not generated in time. Then the vortex sheet satisfies the Birkhoff-Rott equation [43],

$$(3.11) \quad \frac{\bar{\partial} z}{\partial t}(\Gamma, t) = \frac{1}{2\pi i} \text{PV} \int_a^b \frac{d\tilde{\Gamma}}{z(\Gamma, t) - z(\tilde{\Gamma}, t)},$$

where PV denotes principal value, and the circulation Γ is a Lagrangian parameter. Note that the integral is taken over all the circulation.

3.1.2 Discretization and Numerical Methods for 2D Vortex Sheet Flow

Rewriting equation (3.11) using cartesian coordinates (x, y) , we obtain

$$(3.12) \quad \mathbf{u}(\mathbf{x}, t) = \text{PV} \int_a^b \frac{(-(y - \tilde{y}), (x - \tilde{x}))}{2\pi((x - \tilde{x})^2 + (y - \tilde{y})^2)} d\tilde{\Gamma}, \quad \text{where } \mathbf{x} = (x, y).$$

The circulation Γ can not be used as a Lagrangian parameter if it is not monotonic along the curve or circulation is generated in time. Instead, we use an alternative Lagrangian parameter α to parametrize the curve, so that the position and circulation are

$$(3.13) \quad \mathbf{x} = \mathbf{x}(\alpha, t) \quad \text{and} \quad \Gamma = \Gamma(\alpha, t).$$

Choose a set of points $\mathbf{x}_i(t), i = 1, \dots, N$ to represent the sheet. Then we can write down the following discretized form of equation (3.12),

$$(3.14) \quad \frac{\partial \mathbf{x}_i}{\partial t} = \sum_{j=1}^N \mathbf{K}(x_i - x_j) w_j, \quad i = 1, \dots, N,$$

where \mathbf{K} is the kernel in (3.10) and the weight w_j is the circulation carried by each computational point. In computations, the following regularized kernel is used because of stability considerations,

$$(3.15) \quad \mathbf{K}_\delta = \frac{(-y, x)}{2\pi(r^2 + \delta^2)},$$

where $\delta > 0$ is the smoothing parameter. There is also an evolution equation for circulation generation if the flow is not homogeneous, but we defer it to the end of this subsection and focus on equation (3.14) now.

There are a variety of methods for choosing the weight w_j in the discretized equation (3.14). We have compared the second-order trapezoid rule and the fourth-order Simpson's rule. Figure 3.1(a) illustrates the trapezoid rule and Figure 3.1(b) illustrates Simpson's rule. For Simpson's rule, the integral of f on interval $[x_0, x_1]$ is approximated by

$$(3.16) \quad \int_{x_0}^{x_1} f(x) dx \approx \frac{f_0 + 4f_{01} + f_1}{6} h,$$

where h is the step size $x_1 - x_0$. Data is needed at the center of each interval to implement Simpson's rule. Since we do not always have analytical data, cubic

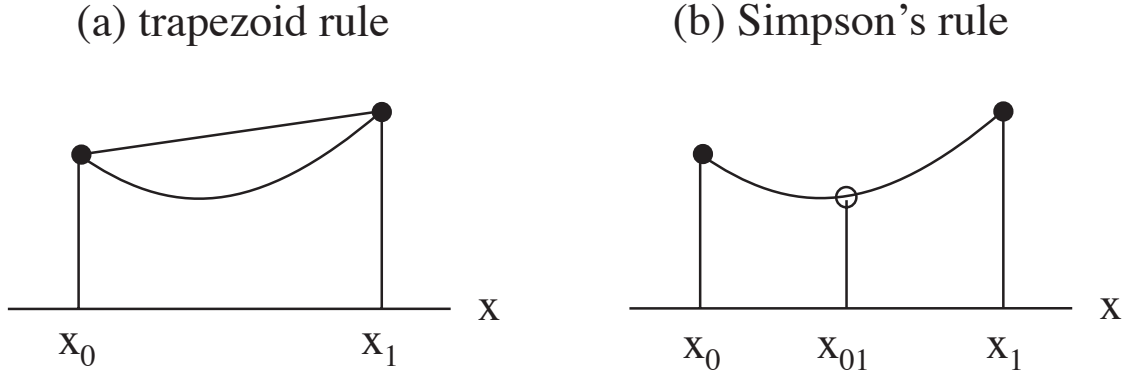


Figure 3.1: Comparison between (a) the trapezoid rule and (b) Simpson's rule. For the trapezoid rule, the integral of f on interval $[x_0, x_1]$ is approximated by the area of the trapezoid as pictured. For Simpson's rule, the formula is presented in (3.16).

polynomials are used to interpolate the data needed. We used cubic polynomials because they are fourth-order accurate, and hence sufficient for the fourth-order Simpson's rule. In the time domain, a standard fourth-order Runge-Kutta scheme is used.

As the sheet evolves, roll-up occurs and hence point insertion is needed to maintain resolution. We tested two schemes for point insertion, linear interpolation and cubic interpolation as illustrated in Figure 3.2. Both methods of interpolation are performed using the parameter α . There are two criteria for point insertion. First, the distance d_1 between two adjacent points is greater than a tolerance ϵ_1 ,

$$(3.17) \quad d_1 > \epsilon_1.$$

Second, the distance d_2 between a tentative linear interpolation and a cubic interpolation is greater than a tolerance ϵ_2 ,

$$(3.18) \quad d_2 > \epsilon_2.$$

If either of these criteria is satisfied, a new particle is inserted and its α value is the average α value of the two adjacent particles.

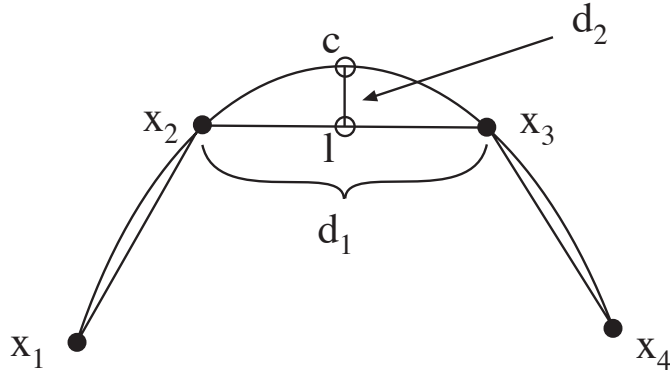


Figure 3.2: Schematic depicting how point insertion is implemented. A new point is inserted if either $d_1 > \epsilon_1$ or $d_2 > \epsilon_2$. The solid points (\cdot) are existing computational points. The two circled points (\circ) are both candidates for a point to be inserted. l is obtained by a linear interpolant, while c is obtained by a cubic interpolant.

In the results presented below we simulate a 2D flow in which a cylinder of heavy fluid settles in a background of lighter fluid. Circulation is generated baroclinically on the interface. The equations (2.21) and (2.31) governing the circulation generation were derived in Chapter II, and they correspond to the Boussinesq approximation and the full density jump case, respectively. We make the Boussinesq approximation in 2D and combine equation (2.21) with the equation (3.12) that governs the vortex sheet motion to obtain

$$(3.19) \quad \frac{\partial \mathbf{x}}{\partial t}(\alpha, t) = \int \mathbf{K}(\mathbf{x}(\alpha, t) - \mathbf{x}(\tilde{\alpha}, t)) d\Gamma(\tilde{\alpha}, t)$$

$$(3.20) \quad \frac{\partial \Gamma}{\partial t}(\alpha, t) = -2Agy(\alpha, t),$$

where A is the Atwood ratio and g is gravity. In the next section when the numerical results are presented for axisymmetric flow, we will make a comparison between the Boussinesq approximation and full density jump. We point out that coordinate z used in equation 2.21 is changed to y here because we will use y as the vertical coordinate for a 2D flow.

Equation (3.20) is solved using a fourth-order Runge-Kutta scheme. To summarize, we have schemes that are fourth-order accurate in time, and either second-order

or fourth-order accurate in space. In space, both quadrature and point insertion can be either second or fourth order accurate.

3.1.3 Computational Results for 2D Vortex Sheets

A cylinder of heavy fluid is immersed in a lighter background. The cross section starts as a perfect disk, and then it sinks and rolls up into a vortex pair. The interface is modeled using a vortex sheet. We make the Boussinesq approximation, so the system (3.19) – (3.20) is being solved. We remark that the initial conditions are $\mathbf{x}(\alpha, 0) = 0.5(\cos \alpha, \sin \alpha)$, $\Gamma(\alpha, 0) = 0$, $\alpha \in [0, 2\pi)$. Presented in Figure 3.3 is a time sequence of the process. The non-dimensional times chosen are $t = 0, 1, 2, 3, 4, 5$. The computation is performed using Simpson’s rule for quadrature, and a cubic interpolant for point insertion, both of which are fourth-order accurate. In the time domain, the fourth-order Runge-Kutta scheme is used.

We list the numerical parameters used in this computation. The Atwood ratio is $A = 0.1$. The initial radius of the cylinder is $R = 0.5$. The initial number of computational points is $N = 40$. We point out that numerical experiments have shown that to ensure numerical stability, the smoothing parameter δ should be larger than the distance between neighboring computational points. The smoothing parameter is $\delta = 0.1$. The time step is $\Delta t = 0.1$. The parameter in the first criterion for point insertion (3.17) is $\epsilon_1 = 0.1$. The parameter in the second criterion (3.18) for point insertion is $\epsilon_2 = 0.0025$. We have tested the numerical parameters to make sure that with the current choices, the computations presented are fully resolved to within plotting error. The running time is negligible, and hence will not be documented in this case.

We can see that as time progresses, the circular cylinder of heavy fluid is com-

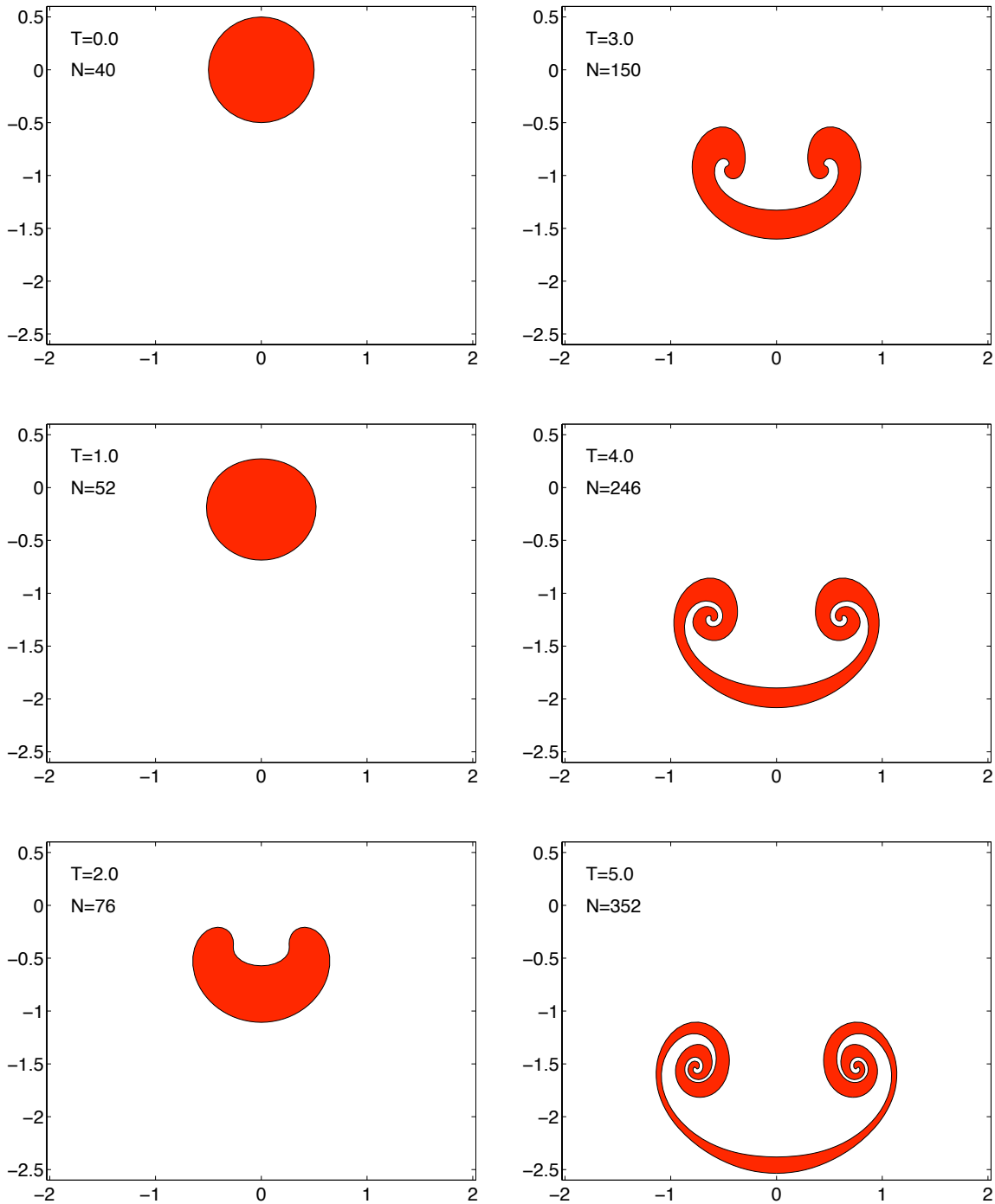


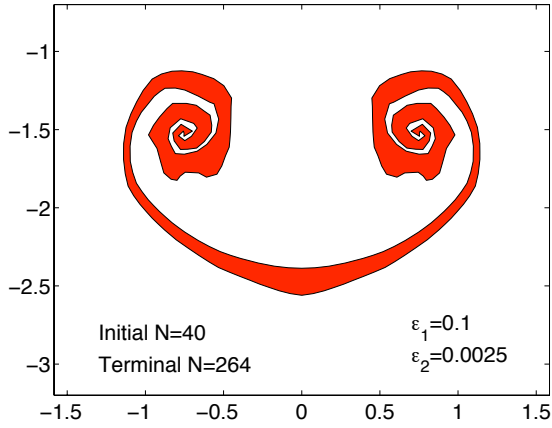
Figure 3.3: A cylinder of heavy fluid settles in a background of lighter fluid. Presented is a time sequence of $t = 0.0, 1.0, 2.0, 3.0, 4.0, 5.0$. Atwood ratio $A = 0.1$. Initial number of computational points $N = 40$. Initial radius $R = 0.5$. Smoothing parameter $\delta = 0.1$. Time step $\Delta t = 0.1$. Parameters for point-insertion criteria (3.17) $\epsilon_1 = 0.1$, (3.18) $\epsilon_2 = 0.0025$. We note that the terminal number of computational points $N = 352$.

pressed in the vertical direction and the shape becomes elliptical. As time progresses further, the cylinder rolls up into two counter-rotating vortices, and the heavy fluid is drawn into the two vortex cores. We note that the number of computational points $N = 352$ at the terminal time $T = 5.0$ is almost 10 times the initial $N = 40$ due to a large amount of stretching between filaments as the sheet evolves.

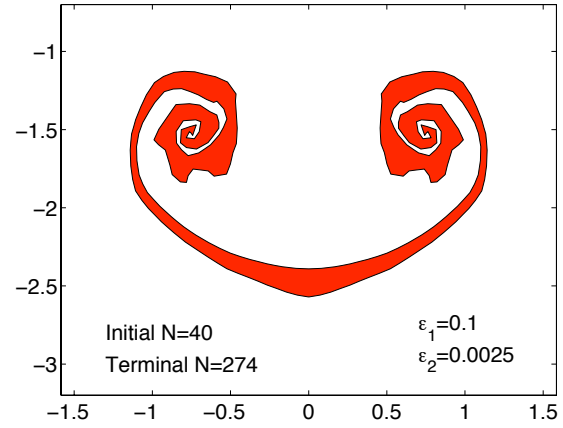
Next we make a comparison between different quadratures and different schemes for point insertion. Presented in Figure 3.4 is the final time $T = 5.0$ of the time sequence in Figure 3.3, obtained using different point insertion schemes or different quadratures and different initial number of computational points. We observe that in Figure 3.4(c), the initial number of computational points is $N = 20$ and the terminal number is $N = 236$. In Figure 3.4(b), the initial number of computational points is $N = 40$ and the terminal $N = 274$. However, the result in Figure 3.4(c) is well resolved, while the one in Figure 3.4(b) is not. The other drawback of the computation in Figure 3.4(b) is that both point insertion thresholds ϵ_1 and ϵ_2 used are lower than those used in the computation in Figure 3.4(c), yet the result in Figure 3.4(b) is still less accurate than the one in Figure 3.4(c). Based on these observations, we conclude that using a higher-order point insertion scheme is more effective than using a higher-order quadrature.

3.2 Axisymmetric Flow

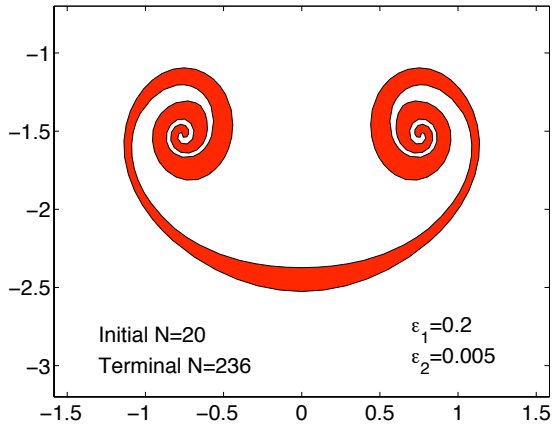
In this section we present numerical results for an initially spherical drop of high density settling in a background of lighter fluid. The drop is assumed to be axisymmetric in the whole process. Axisymmetric flow has some 3D effects, but it is simpler to compute than fully 3D flow. We follow the approach by Nitsche and Krasny [37]



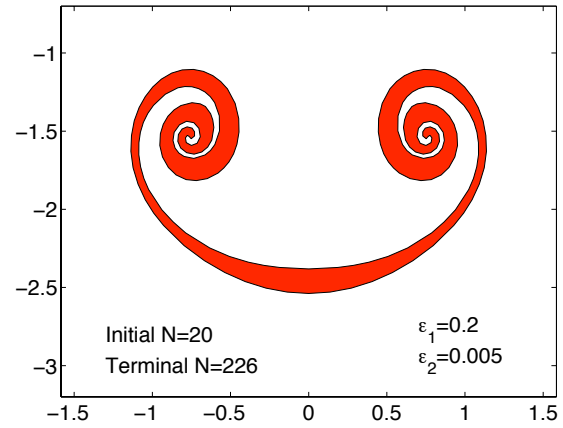
(a) 2nd order insertion, 2nd order integration



(b) 2nd order insertion, 4th order integration



(c) 4th order insertion, 2nd order integration



(d) 4th order insertion, 4th order integration

Figure 3.4: Comparison between schemes of different order of accuracy at terminal time $T = 5.0$ as shown in Figure 3.3. They use the same numerical parameters $R = 0.5$, $\delta = 0.1$, $\Delta t = 0.1$ as used in the computation presented in Figure 3.3. However, they use different initial number of computational points N , different point insertion parameters ϵ_1, ϵ_2 as printed in the plots. They each use different point insertion scheme or different integration scheme as printed in the sub-captions.

and Nitsche [36] to use elliptic functions in evaluating the velocity of an axisymmetric vortex sheet.

We will make a comparison between the Boussinesq approximation and full density jump. The numerical methods for the case when the Boussinesq approximation were

described in the previous section for 2D flow. Since it is similar for an axisymmetric flow, they will not be repeated. Now we describe how the equation for vorticity generation for the full density jump case, which is implicit, is solved. We combine equation (2.31) with the equation (3.12) that governs the vortex sheet motion to obtain the system,

$$(3.21) \quad \frac{\partial \mathbf{x}}{\partial t} = \int \mathbf{K}(\mathbf{x} - \tilde{\mathbf{x}}) d\tilde{\Gamma}$$

$$(3.22) \quad \frac{\partial \Gamma}{\partial t} = -2A \left(\frac{\partial}{\partial t} \int \Gamma \frac{\partial G}{\partial \mathbf{n}} dS - \frac{1}{2} |\mathbf{u}|^2 + \frac{1}{8} \gamma^2 + gy \right),$$

where $\partial G / \partial \mathbf{n}$ is the normal derivative of the Newtonian potential

$$(3.23) \quad G = \frac{1}{4\pi} \frac{1}{|\mathbf{x} - \tilde{\mathbf{x}}|},$$

dS is an area element on the sheet, \mathbf{u} is the velocity of the sheet, and $\gamma = d\Gamma/ds$ is the vortex sheet strength.

Equation (3.22) is solved using a fourth-order Runge-Kutta scheme, and each stage in the Runge-Kutta method is solved with an iterative method as explained below. We need $\partial \Gamma / \partial t$ so that Γ can be updated. Let the sheet surface be $\mathbf{x} = (x, y, z) = \mathbf{x}(\alpha, \theta, t)$, $0 \leq \alpha \leq \pi$, $0 \leq \theta \leq 2\pi$, then the integral on the right hand side of equation (3.22), which is simply the average potential ϕ as defined in subsection 2.4.2, can be computed to be

$$(3.24) \quad \phi = \frac{1}{4\pi} \int_0^\pi \int_0^{2\pi} \frac{(x - \tilde{x})y_\theta z_\alpha + (y - \tilde{y})x_\theta z_\alpha + (z - \tilde{z})(x_\alpha y_\theta - y_\alpha x_\theta)}{|\mathbf{x} - \tilde{\mathbf{x}}|^3} \Gamma d\theta d\alpha.$$

In an axisymmetric flow, \mathbf{x} and $\tilde{\mathbf{x}}$ can be written as

$$(3.25) \quad \mathbf{x} = (x \cos \theta_1, x \sin \theta_2, y) \quad \text{and} \quad \tilde{\mathbf{x}} = (\tilde{x} \cos \theta_1, \tilde{x} \sin \theta_2, \tilde{y})$$

Now, let $\theta = \theta_1 - \theta_2$, then $|\mathbf{x} - \tilde{\mathbf{x}}| = \sqrt{x^2 + \tilde{x}^2 - 2x\tilde{x}\cos\theta + (y - \tilde{y})^2}$ and (3.24)

becomes

$$(3.26) \quad \phi = \frac{1}{4\pi} \int_0^\pi \int_0^{2\pi} \frac{\tilde{x}\tilde{y}_\alpha(\tilde{x} - x\cos\theta) + \tilde{x}\tilde{x}_\alpha(y - \tilde{y})}{(x^2 + \tilde{x}^2 - 2x\tilde{x}\cos\theta + (y - \tilde{y})^2)^{3/2}} \Gamma d\theta d\alpha.$$

Now we introduce the elliptic functions to simplify (3.26). Let $k_1 = \sqrt{(x - \tilde{x})^2 + (y - \tilde{y})^2}$ and $k_2 = \sqrt{(x - \tilde{x})^2 + (y + \tilde{y})^2}$. Let $k = \sqrt{1 - k_1^2/k_2^2}$, then we define the two elliptic functions

$$(3.27) \quad F(k) = \int_0^{\pi/2} \frac{1}{\sqrt{1 - k^2 \sin^2 \theta}} d\theta$$

and

$$(3.28) \quad E(k) = \int_0^{\pi/2} \sqrt{1 - k^2 \sin^2 \theta} d\theta.$$

With these definitions, (3.26) can be simplified to be

$$(3.29) \quad \phi = \frac{1}{\pi} \int_0^\pi \left[\frac{\tilde{x}\tilde{y}_\alpha(\tilde{x} - x) + \tilde{x}\tilde{x}_\alpha(y - \tilde{y})}{k_1^2 k_2} E(k) + \frac{\tilde{y}_\alpha}{2k_2} F(k) \right] \Gamma d\alpha.$$

Letting

$$(3.30) \quad f_1 = \frac{\tilde{x}\tilde{y}_\alpha(\tilde{x} - x) + \tilde{x}\tilde{x}_\alpha(y - \tilde{y})}{k_1^2 k_2}$$

and

$$(3.31) \quad f_2 = \frac{\tilde{y}_\alpha}{2k_2},$$

equation (3.29) becomes

$$(3.32) \quad \phi = \frac{1}{\pi} \int_0^\pi (f_1 E(k) + f_2 F(k)) \Gamma d\alpha.$$

Finally,

$$(3.33) \quad \begin{aligned} \frac{\partial \phi}{\partial t} &= \frac{\partial}{\partial t} \int \Gamma \frac{\partial G}{\partial \mathbf{n}} dS \\ &= \frac{1}{\pi} \int_0^\pi \left[\frac{d}{dt} (f_1 E(k)) + \frac{d}{dt} (f_2 (F(k) - F(k))) \right] \Gamma \\ &\quad + [f_1 E(k) + f_2 (F(k) - F(k))] \frac{\partial \Gamma}{\partial t} d\alpha. \end{aligned}$$

This equation is in the right hand side of equation (3.22) to do the iteration. The algorithm starts with a guess of $\partial\Gamma/\partial t$, which is 0 for the first time step, and the value of $\partial\Gamma/\partial t$ from previous step for later time steps. All the derivatives that appear are computed with a central difference scheme. The iteration is repeated until the L_1 norm of $\partial\Gamma/\partial t$ does not change by more than a threshold $\epsilon = 0.001$ between two consecutive iterations. We restate that the converged $\partial\Gamma/\partial t$ will be used as the initial guess for the next time step.

For the Boussinesq approximation case there is a scaling law, which will be explained now. This law holds for both 2D flow and 3D flow, but it will only be explained here for the 3D case as the reasoning is similar for both cases. Take the system (3.19) – (3.20), let $t' = t/S$ and $\Gamma' = S\Gamma$, where S is a scaling constant. After substituting these two new variables into the system, we obtain

$$(3.34) \quad \frac{\partial \mathbf{x}}{\partial t'}(\alpha, t') = \int \mathbf{K}(\mathbf{x} - \tilde{\mathbf{x}}) d\tilde{\Gamma}'$$

$$(3.35) \quad \frac{\partial \Gamma'}{\partial t'}(\alpha, t') = -2S^2 Agy(\alpha, t'),$$

Removing the primes, we have

$$(3.36) \quad \frac{\partial \mathbf{x}}{\partial t}(\alpha, t) = \int \mathbf{K}(\mathbf{x} - \tilde{\mathbf{x}}) d\tilde{\Gamma}$$

$$(3.37) \quad \frac{\partial \Gamma}{\partial t}(\alpha, t) = -2S^2 Agy(\alpha, t),$$

This means that in the Boussinesq approximation, changing the Atwood ratio amounts to changing the time scale. We now illustrate this computationally. In Figure 3.5 we present results for axisymmetric flow. The Boussinesq approximation is made in the left column, while the full density jump is accounted for in the right column. We can see that the scaling law as shown in equations (3.36) – (3.37) is verified in the left column. Every time the Atwood ratio decreases by a factor of 4, we only need to double the terminal time to obtain the same result.

The right column in Figure 3.5 shows that at a fixed time, the full density jump formulation converges to the Boussinesq approximation as the Atwood ratio A tends to 0.

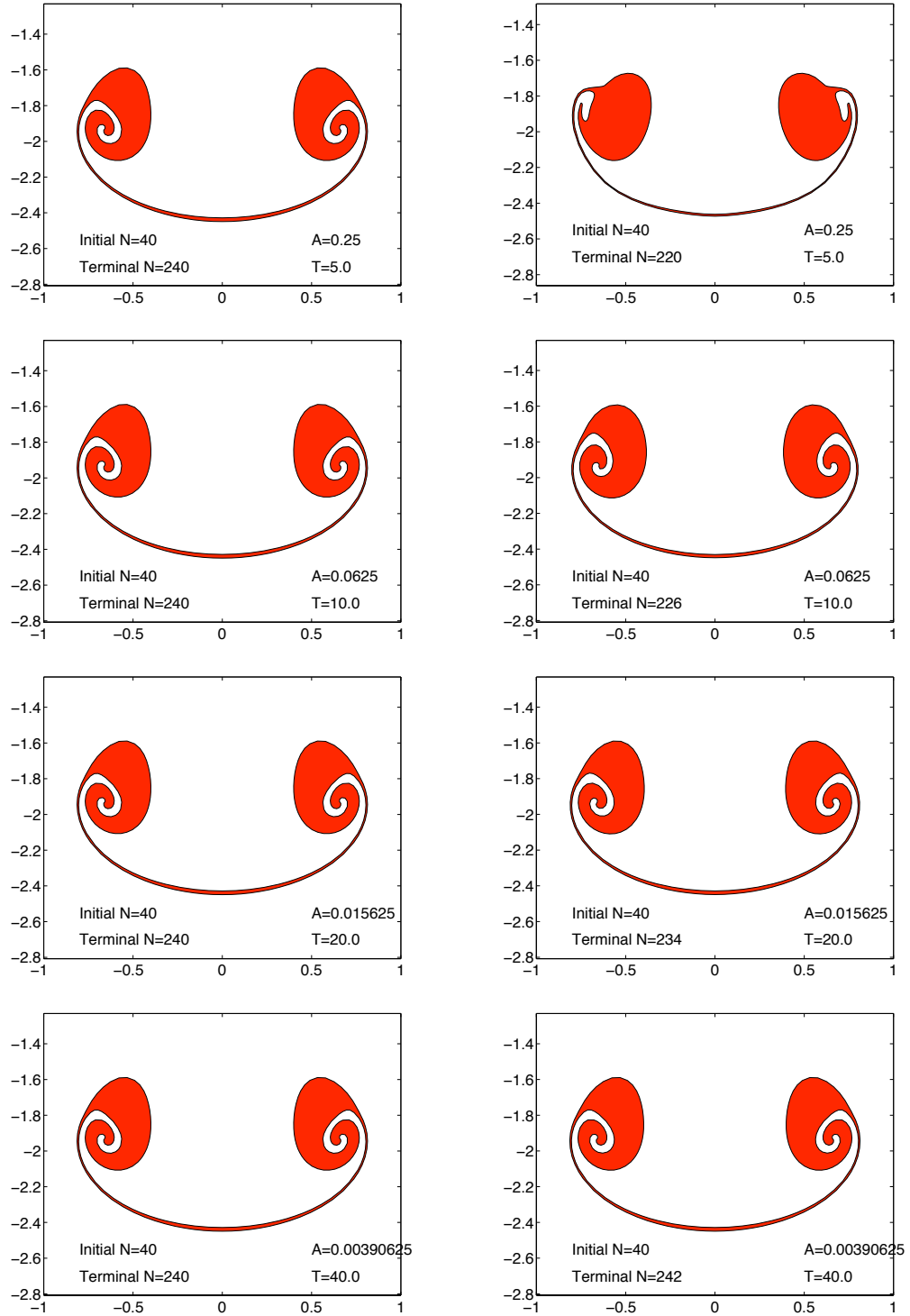


Figure 3.5: Comparison between the Boussinesq approximation (left) and full density jump(right). The Atwood ratio starts with $A = 0.25$ and reduces by a factor of 4 from each row to the next as printed in the picture, while the terminal time T doubles. It is evident that the results for the full density jump case tend to the results for the Boussinesq approximation case as A tends to 0. This also illustrates the scaling between A and T as shown in equations (3.36) and (3.37) in the Boussinesq approximation

CHAPTER IV

Vortex Sheets in Three Dimensional Flow

The dynamics of 3D vortex sheets is considerably more complicated than the 2D or axisymmetric case, and this chapter is devoted to describing the relevant numerical methods. The chapter starts in section 4.1 with a review of previous work on computations of 3D vortex sheets. This is followed by a description in section 4.2 of discretization and quadrature schemes developed for the computations. The refinement schemes are described in section 4.3 and barycentric coordinates as used in the refinement strategy are also explained. Finally, section 4.4 reviews the fast multipole method and tree-code as applied to vortex sheets.

4.1 Previous Work on Computations of 3D Vortex Sheets

In three dimensions, the discretization of a vortex sheet is a rather difficult issue due to stretching and twisting. The sheet is represented using a surface and material points are put on the surface. In the literature, the sheet has been discretized with either quadrilateral or triangular mesh. We start by describing how a 3D vortex sheet has been represented previously in the literature, and this is followed by a subsection on review of previous computational work.

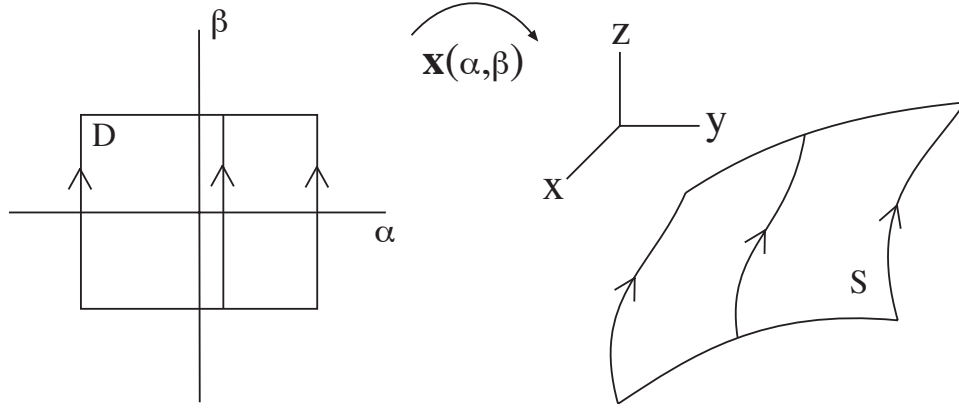


Figure 4.1: Schematic of a parameter space D and the corresponding physical space S . The sheet surface $\mathbf{x}(\alpha, \beta, t)$ defines a mapping from the parameter space (α, β) to the physical space (x, y, z) . Several vortex filaments are plotted.

4.1.1 Representation of 3D Vortex Sheets

If α and β are used to parametrize the vortex sheet, then we have the position $\mathbf{x} = \mathbf{x}(\alpha, \beta, t)$ and the vortex sheet strength $\gamma(\alpha, \beta, t)$. As was shown in equation (2.9), the velocity is obtained from the vorticity using the Biot-Savart integral,

$$(4.1) \quad \mathbf{u}(\mathbf{x}, t) = \int_S \mathbf{K}(\mathbf{x} - \tilde{\mathbf{x}}) \times \gamma dS, \quad \mathbf{K}(\mathbf{x}) = -\frac{\mathbf{x}}{4\pi|\mathbf{x}|^3}.$$

Recall that the related scalar circulation $\Gamma(\alpha, \beta, t)$ is equal to the potential jump $[\phi](\alpha, \beta, t)$ across the sheet, and we will see next how Γ enters in equation (4.1).

We follow the treatment of Caffisch [8] and Kaneda [24] to convert the integral in (4.1), which is an integral over the sheet surface, into an integral over the parameter space (α, β) . As shown in Figure 4.1, we draw a schematic of the map from the planar parameter space D to the sheet surface. This transformation is important as it was used in many computations of 3D vortex sheets. In doing this conversion, we will make use of the relation between γ and $\Gamma(\alpha, \beta, t)$ as illustrated below. Recall that the vortex sheet strength γ is related to the velocity jump $[\mathbf{u}]$ across the sheet as follows [6],

$$(4.2) \quad \gamma = \mathbf{n} \times [\mathbf{u}].$$

We replace \mathbf{n} with $\mathbf{x}_\alpha \times \mathbf{x}_\beta / |\mathbf{x}_\alpha \times \mathbf{x}_\beta|$ and $[\mathbf{u}]$ with $[\nabla\phi]$ to obtain

$$(4.3) \quad \gamma = \frac{\mathbf{x}_\alpha \times \mathbf{x}_\beta}{|\mathbf{x}_\alpha \times \mathbf{x}_\beta|} \times [\nabla\phi],$$

As noted at the beginning of this section, $[\phi](\alpha, \beta, t) = \Gamma(\alpha, \beta, t)$. This implies that

(4.3) can be transformed as

$$(4.4) \quad \gamma = \frac{(\mathbf{x}_\alpha \times \mathbf{x}_\beta) \times [\nabla\phi]}{|\mathbf{x}_\alpha \times \mathbf{x}_\beta|} = \frac{([\nabla\phi] \cdot \mathbf{x}_\alpha)\mathbf{x}_\beta - ([\nabla\phi] \cdot \mathbf{x}_\beta)\mathbf{x}_\alpha}{|\mathbf{x}_\alpha \times \mathbf{x}_\beta|} = \frac{\Gamma_\alpha \mathbf{x}_\beta - \Gamma_\beta \mathbf{x}_\alpha}{|\mathbf{x}_\alpha \times \mathbf{x}_\beta|}.$$

Let $J = |\mathbf{x}_\alpha \times \mathbf{x}_\beta|$ be the Jacobian of the parametrization $\mathbf{x} = \mathbf{x}(\alpha, \beta, t)$. Then the area element dS becomes

$$(4.5) \quad dS = J d\alpha d\beta = |\mathbf{x}_\alpha \times \mathbf{x}_\beta| d\alpha d\beta.$$

Combining (4.4) and (4.5), we obtain

$$(4.6) \quad \gamma dS = \frac{\Gamma_\alpha \mathbf{x}_\beta - \Gamma_\beta \mathbf{x}_\alpha}{|\mathbf{x}_\alpha \times \mathbf{x}_\beta|} |\mathbf{x}_\alpha \times \mathbf{x}_\beta| d\alpha d\beta = (\Gamma_\alpha \mathbf{x}_\beta - \Gamma_\beta \mathbf{x}_\alpha) d\alpha d\beta$$

and (4.1) becomes

$$(4.7) \quad \mathbf{u}(\mathbf{x}, t) = \int_D \mathbf{K}(\mathbf{x} - \tilde{\mathbf{x}}) \times (\tilde{\Gamma}_\alpha \tilde{\mathbf{x}}_\beta - \tilde{\Gamma}_\beta \tilde{\mathbf{x}}_\alpha) d\tilde{\alpha} d\tilde{\beta},$$

which is an integral over the parameter space D .

Recall that vortex filaments on a vortex sheet are curves tangential to the vortex sheet strength γ . Another way to characterize vortex filaments is that the circulation $\Gamma = \Gamma(\alpha, \beta, t)$ is constant along a vortex filament. Several vortex filaments are drawn on the sheet surface in Figure 4.1, and in this case they correspond to straight lines in the parameter space.

We have given a general 3D vortex sheet formulation. Next we give a survey of previous computations of 3D vortex sheets as related to our work, and we will see how the formulation described above was used. In particular, attention will be given to how the $(\Gamma_\alpha \mathbf{x}_\beta - \Gamma_\beta \mathbf{x}_\alpha) d\tilde{\alpha} d\tilde{\beta}$ term in equation (4.7) was discretized in previous work.

4.1.2 Review of Previous Computational Work

Brady, Leonard, and Pullin [7] used a triangular mesh to discretize a vortex sheet supported on a torus. Their algorithm tried to make each triangle on the sheet as close to equilateral as possible, which requires a remeshing strategy after each time step. For this purpose, an advancing-front method was used, and the algorithm interpolated over the parameter space to put points on the sheet surface where needed. It is ideal to have as small a number of computational points as possible to reduce the computational cost, yet at the same time accuracy of the algorithm also has to be considered. With both of these in mind, it is important to have triangles on the physical sheet surface as close to equilateral as possible. However, as time progresses, even though the triangles in physical space are close to equilateral, the corresponding triangles in the parameter space become highly distorted and many slender triangles appear as shown in Brady et al.[7]. This may cause loss of accuracy when equation (4.7) is used to evaluate the velocity of the sheet surface because it is an integral over the parameter space $D = (\alpha, \beta)$.

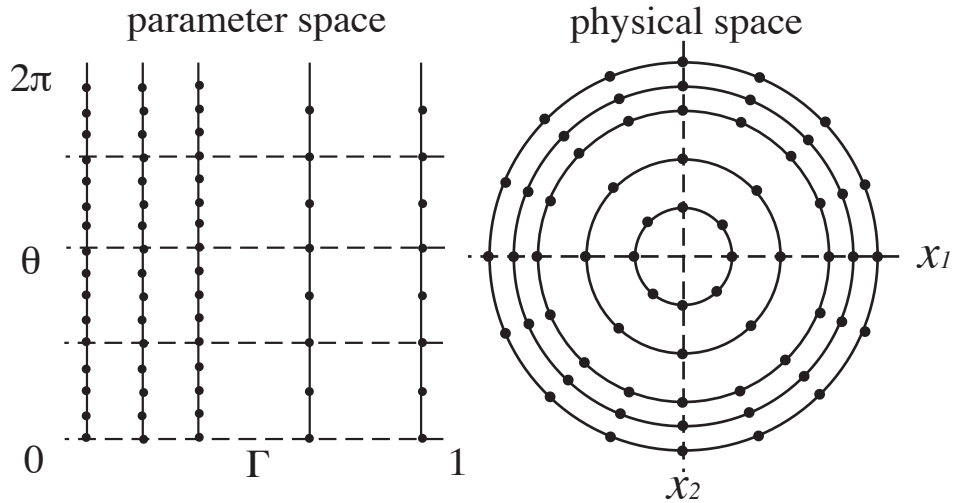


Figure 4.2: Discretization of a circular vortex sheet into vortex filaments. Each filament is discretized using Lagrangian particles [34].

Lindsay and Krasny [34] developed a tree-code to evaluate the self-induced velocity of a 3D vortex sheet and performed numerical computations of vortex rings. In their simulations vortex rings were simulated as vortex sheets which started as circular disks of radius 1. In Figure 4.2 we draw a schematic of their parametrization. On the left is the parameter space $(\alpha, \beta) = [0, \pi/2] \times [0, 2\pi]$ and on the right is the physical space. The initial parametrization is $\mathbf{x}(\alpha, \beta, 0) = (\sin \alpha \cos \beta, \sin \alpha \sin \beta, 0)$ and the initial circulation is $\Gamma(\alpha, \beta, 0) = \cos \alpha$, so a constant α value in the parameter space corresponds to a circle in the physical space as shown in Figure 4.2, and hence each of the concentric circles in the physical space is a filament.

They discretized the vortex sheet into filaments and each filament was discretized into particles. Since each vortex filament has a constant Γ value dependent only on α , the $(\Gamma_\alpha \mathbf{x}_\beta - \Gamma_\beta \mathbf{x}_\alpha) d\tilde{\alpha} d\tilde{\beta}$ term in equation (4.7) becomes $(\Gamma_\alpha \mathbf{x}_\beta) d\tilde{\alpha} d\tilde{\beta}$. Equivalently, they think of each vortex filament as an object carrying a certain amount of circulation and each filament is discretized using the Lagrangian parameter β .

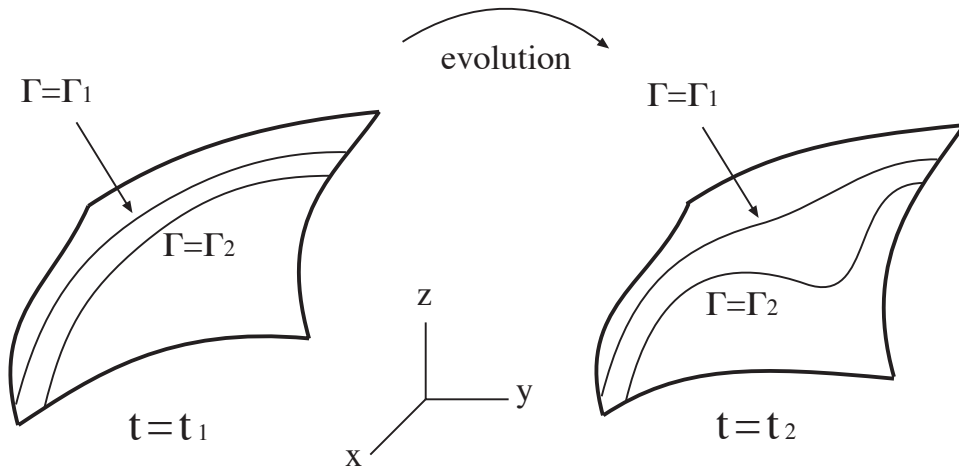


Figure 4.3: As the vortex sheet evolves, non-uniform stretching may cause two previously parallel vortex filaments to separate far at some point while stay close elsewhere.

As the sheet surface evolves, stretching and twisting occur and hence refinement is needed to maintain resolution. Their refinement strategy has two parts. First,

they check the shortest distance between each pair of adjacent vortex filaments. If the distance is greater than a tolerance, an entire new filament is inserted. Second, they check the particles on each filament and if two adjacent particles separate too far from each other, a new particle is inserted so that resolution is also maintained along each filament.

The merit of this approach is that it is simple to implement. However, as illustrated in Figure 4.3, two adjacent vortex filaments may separate far from each other locally, but stay relatively close elsewhere. A new filament is added in this case and this is a waste of computational resources. This difficulty was alleviated by using a panel method developed by Kaganovskiy [22], as reviewed below.

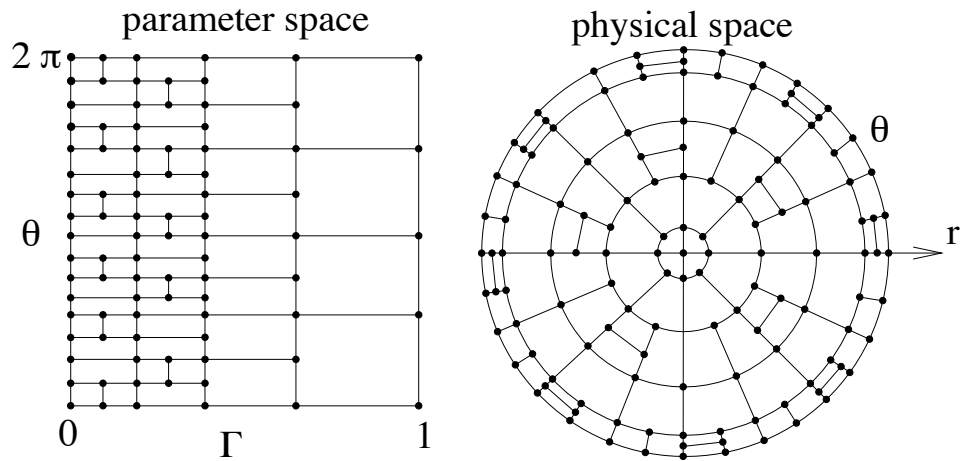


Figure 4.4: Discretization of a circular vortex sheet into quadrilateral panels. Each panel has 4, 5, or 6 (not shown) points [22].

Kaganovskiy [22] developed a quadrilateral panel method for 3D vortex sheet simulations and applied the method to vortex rings. He discretized the vortex sheet into quadrilateral panels, each of which has 4, 5, or 6 points. Figure 4.4 is a schematic of his discretization. The panels have a tree structure which helps in both the quadrature and the refinement schemes. When information from neighboring panels is needed, the algorithm starts from the root and searches for neighboring panels.

This is naturally adaptive because as panels are split and new particles are added, it would be difficult to keep track of neighbors without a tree structure. Quadratures with different orders of accuracy were also developed. Since the refinement scheme is locally adaptive, an entire filament did not have to be inserted as in Lindsay [34]. This saves computational cost.

4.2 Discretization and Quadrature Developed in This Thesis

A triangulation, similar to the one used by Brady et al. [7], is also used in our computations. However, the discretization we developed is different than in previous work in that we do not use the global Lagrangian parameters (α, β) . We note that in equation (4.7), there are derivatives of the flow map $\mathbf{x} = \mathbf{x}(\alpha, \beta, t)$ with respect to the parameters α and β . As the vortex sheet evolves, those derivatives will grow rapidly in amplitude. We avoid computing these derivatives by discretizing equation (4.1) rather than equation (4.7). Next we describe how this is done. First, we show how the γdS term in equation (4.1) is computed. Then, we explain the underlying data structure in the representation of the vortex sheet and how the integral in (4.1) is evaluated. The numerical method we developed is a panel method, for which Katz and Plotkin [25] is a comprehensive reference.

4.2.1 Computation of Vorticity Carried by Panels

We use triangular panels to discretize the vortex sheet surface. Figure 4.5 shows a triangular panel abc . We need to compute the vorticity γdS carried by abc as the Biot-Savart integral (4.1) requires this quantity. We will compute γ and dS separately and then take the product. Without loss of generality, assume that the

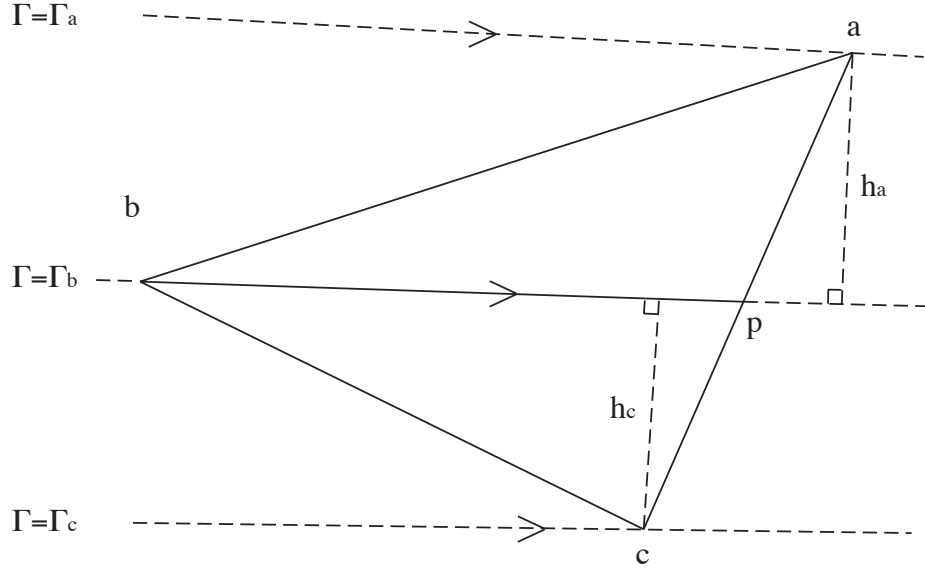


Figure 4.5: A triangular panel with vertices \mathbf{a} , \mathbf{b} , \mathbf{c} . The vortex filaments through the vertices assist in the calculation of the vortex sheet strength γ on the panel \mathbf{abc} .

circulation satisfies $\Gamma_{\mathbf{a}} < \Gamma_{\mathbf{b}} < \Gamma_{\mathbf{c}}$. Then there is a point \mathbf{p} on edge \mathbf{ac} such that $\Gamma_{\mathbf{p}} = \Gamma_{\mathbf{b}}$, so $\overrightarrow{\mathbf{bp}}$ lies on a vortex filament. We also draw the two vortex filaments through point \mathbf{a} and point \mathbf{c} as they will be used in the calculations below. With the auxiliary point \mathbf{p} , the triangle \mathbf{abc} can be split into two triangles \mathbf{abp} and \mathbf{bcp} . With $\overrightarrow{\mathbf{bp}}$ as the base, \mathbf{abp} and \mathbf{bcp} have heights $h_{\mathbf{a}}$ and $h_{\mathbf{c}}$ respectively.

From equation (2.11) it can be derived that the circulation $\Gamma(A, B)$ between two points A and B on the vortex sheet is

$$(4.8) \quad \Gamma(A, B) = \int_C [\mathbf{u}] \cdot d\mathbf{s},$$

where C is any curve on the sheet connecting A to B , and $d\mathbf{s}$ is an arc element on the curve. If A and B are such that a curve C parallel to $[\mathbf{u}]$ can be chosen, then the above integral becomes

$$(4.9) \quad \Gamma(A, B) = \int_C |[\mathbf{u}]| ds,$$

where ds is an arc-length element on C , and hence $|[\mathbf{u}]| = d\Gamma/ds$. However, $|[\mathbf{u}]|$ is exactly the magnitude of the vortex sheet strength $\gamma = \mathbf{n} \times [\mathbf{u}]$. So we conclude that

the magnitude of the vortex sheet strength is

$$(4.10) \quad |\boldsymbol{\gamma}| = \frac{d\Gamma}{ds},$$

where ds is an arc-length element in a direction parallel to the velocity jump $[\mathbf{u}]$, which is normal to $\boldsymbol{\gamma}$ since $\boldsymbol{\gamma} = \mathbf{n} \times [\mathbf{u}]$. On triangle \mathbf{abc} , $d\Gamma$ is $\Gamma_c - \Gamma_a$ and ds is $h_c + h_a$ since both h_c and h_a are normal to $\boldsymbol{\gamma}$. The magnitude of the vortex sheet strength $\boldsymbol{\gamma}$ is then approximated by

$$(4.11) \quad |\boldsymbol{\gamma}| = \frac{\Gamma_c - \Gamma_a}{h_c + h_a},$$

and the direction is determined by the vector $\overrightarrow{\mathbf{bp}}$ since it lies on a filament. Then, the vortex sheet strength $\boldsymbol{\gamma}$ on this triangle is approximated by

$$(4.12) \quad \frac{\Gamma_c - \Gamma_a}{h_c + h_a} \frac{\overrightarrow{\mathbf{bp}}}{|\overrightarrow{\mathbf{bp}}|}.$$

It remains to calculate the vorticity $\boldsymbol{\gamma} dS$ carried by the triangle, which is simply the product of $\boldsymbol{\gamma}$ and the triangle's area in this case. We have the following,

$$(4.13) \quad \boldsymbol{\gamma} dS = \frac{\Gamma_c - \Gamma_a}{h_c + h_a} \frac{\overrightarrow{\mathbf{bp}}}{|\overrightarrow{\mathbf{bp}}|} |\overrightarrow{\mathbf{bp}}| \frac{h_c + h_a}{2} = \frac{\Gamma_c - \Gamma_a}{2} \overrightarrow{\mathbf{bp}}.$$

We observe that since $\Gamma_p = \Gamma_b$, with the assumption that the circulation Γ varies linearly on edge \mathbf{ac} , \mathbf{p} can be interpolated as a weighted average of \mathbf{a} and \mathbf{c} ,

$$(4.14) \quad \mathbf{p} = \frac{(\Gamma_c - \Gamma_b) \mathbf{a} + (\Gamma_b - \Gamma_a) \mathbf{c}}{\Gamma_c - \Gamma_a}.$$

Using this to compute $\overrightarrow{\mathbf{bp}}$ and substituting it into equation (4.13), we obtain the vorticity $\boldsymbol{\gamma} dS$ carried by the triangle \mathbf{abc} ,

$$(4.15) \quad \boldsymbol{\gamma} dS = \frac{1}{2}(\Gamma_a(\mathbf{b} - \mathbf{c}) + \Gamma_b(\mathbf{c} - \mathbf{a}) + \Gamma_c(\mathbf{a} - \mathbf{b})),$$

which is a 3D vector. Now we realize that \mathbf{p} was only an auxiliary point as it does not appear in the final expression. Note that if we orient the triangle \mathbf{abc} in the

opposite direction \mathbf{acb} , the sign of its vorticity γdS would be reversed. But this does not cause a problem, because the triangle's orientation is determined by the surface orientation, which in turn depends on the underlying physics.

4.2.2 Data Structure and Evaluation of the Biot-Savart Integral

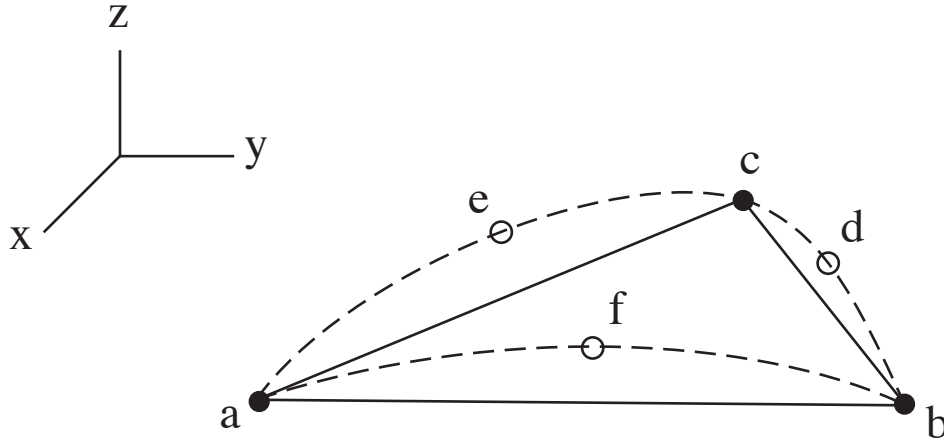


Figure 4.6: A triangular panel consists of three active points a, b, c and three passive points d, e, f . The linear triangle formed by the active points assists in computation of the vorticity carried by the panel, while the quadratic triangle formed by all points assists in the refinement procedure to be described in the next section.

In this thesis, we use the terms points and particles interchangeably. The vortex sheet is discretized as a set of panels, and each panel has vertices and edges. As shown in Figure 4.6, a panel consists of three active points a, b, c and three passive points d, e, f . The three active points form a linear triangle (solid lines), which is used to compute the vorticity carried by this panel. This quantity is used in the Biot-Savart integral (4.1) as explained in the previous section. The active and passive points together determine a quadratic curved triangle (dotted curves), which will be used in the refinement procedure to be described in the next section. The passive points are not used in the quadrature to evaluate the Biot-Savart integral, however, but we include them in the picture for future reference.

In the computations, we discretize the vortex sheet using M panels p_i , $i = 1, \dots, M$ and N particles x_j , $j = 1, \dots, N$. We may consider two options for implementing the Biot-Savart integral (4.1). First, we can write down the following trapezoid-like rule for evaluating the sheet velocity (with N particles after discretization),

$$(4.16) \quad \frac{\partial \mathbf{x}_i}{\partial t} = \frac{1}{3} \sum_{j=1}^N \mathbf{K}_\delta(\mathbf{x}_i - \mathbf{x}_j) \times \mathbf{w}_j, \quad i = 1, \dots, N,$$

where \mathbf{w}_j is the summation of vorticity carried by all panels incident to particle j . Recall that the vorticity carried by a panel is computed by formula (4.15). Tests were conducted to show that this scheme is second-order accurate in space like the one-dimensional trapezoid rule.

Second, we can also write down the following midpoint-like rule (with M panels after discretization),

$$(4.17) \quad \frac{\partial \mathbf{x}_i}{\partial t} = \sum_{j=1}^M \mathbf{K}_\delta(\mathbf{x}_i - \mathbf{C}_j) \times \mathbf{w}_j, \quad i = 1, \dots, N,$$

where \mathbf{C}_j is the centroid of the j -th triangular panel and \mathbf{w}_j is the vorticity carried by it. This scheme is also second-order accurate in space. We used the first scheme in the computations and consider the second scheme as a direction for future research.

4.3 Adaptive Refinement

As the vortex sheet stretches and twists, some method of refinement is needed to maintain resolution. In this section we explain how the refinement was implemented in this thesis. The section starts with an introduction to barycentric coordinates, followed by a description of adaptive panel subdivision and particle insertion.

4.3.1 Barycentric Coordinates

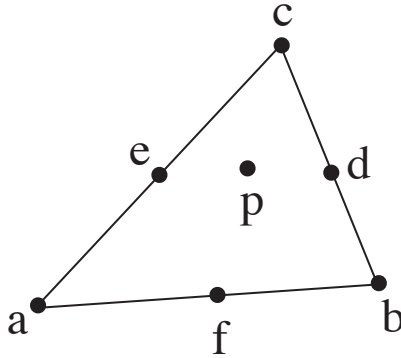


Figure 4.7: A triangle in the xy plane. Any point p in the triangle can be uniquely expressed as a combination of the three vertices a, b, c using barycentric coordinates.

In Figure 4.7 we draw a triangle abc in the xy plane with a, b, c as vertices and d, e, f as midpoints of the three edges bc, ca, ab , respectively. Any point p in the triangle can be defined by barycentric coordinates u, v, w with respect to the three vertices a, b, c such that we have a unique expression,

$$(4.18) \quad \mathbf{p} = u\mathbf{a} + v\mathbf{b} + w\mathbf{c}, \quad \text{where } u, v, w \in [0, 1] \text{ and } u + v + w = 1.$$

For instance, with respect to vertices a, b, c , the six points a, b, c, d, e, f in the figure have barycentric coordinates

$$(4.19) \quad (1, 0, 0), (0, 1, 0), (0, 0, 1), (0, 1/2, 1/2), (1/2, 0, 1/2), (1/2, 1/2, 0),$$

respectively.

Since a quadratic function in two variables

$$(4.20) \quad f(x, y) = c_{20}x^2 + c_{02}y^2 + c_{11}xy + c_{10}x + c_{01}y + c_{00}$$

has 6 free coefficients, it is uniquely determined by 6 function values. Strictly speaking, it can be shown in approximation theory that it is not always possible to determine a two-variable quadratic function over a plane with 6 points. The degenerate

case occurs when the 6 points lie on a quadratic planar curve, which does not arise in our context because the 6 points as depicted in Figure 4.7 do not lie on a quadratic planar curve.

It is also possible to write down a quadratic function using barycentric coordinates,

$$(4.21) \quad f(u, v, w) = c_{200}u^2 + c_{020}v^2 + c_{002}w^2 + c_{110}uv + c_{101}uw + c_{011}vw.$$

where the c 's are free coefficients and u, v, w are the barycentric coordinates. We note that although this function has three variables, they are not independent and the function can be interpreted as a quadratic function over the xy plane in Cartesian coordinates. It is also worth pointing out that every term in (4.21) is of second order, while only the first two term in (4.20) are of second order. The quadratic functions in (4.20) and (4.21) are called Bezier patches, and there is a detailed treatment of Bezier patches in Goodman and Said [20].

The reason for using barycentric coordinates rather than Cartesian coordinates is because it is much simpler to interpolate over a triangle using barycentric coordinates. To uniquely determine a quadratic Bezier patch over a triangle, 6 function values on the patch are required. In the special case when the function values are prescribed at the three vertices and three midpoints of the edges as shown in Figure 4.7, the Bezier patch as an interpolant can be written down easily as can be found in Goodman and Said [20].

4.3.2 Adaptive Panel Subdivision and Particle Insertion

We restate that each triangular panel has three active points and three passive points as drawn in Figure 4.8. We will use barycentric coordinates (u, v, w) , calculated with respect to $\mathbf{a}, \mathbf{b}, \mathbf{c}$ to label those points. The three solid points $\mathbf{a}, \mathbf{b}, \mathbf{c}$ are

the active points, and they have barycentric coordinates

$$(4.22) \quad (1, 0, 0), (0, 1, 0), (0, 0, 1),$$

respectively. The three circled points $\mathbf{d}, \mathbf{e}, \mathbf{f}$ are the passive points, and their barycentric coordinates are

$$(4.23) \quad (0, 1/2, 1/2), (1/2, 0, 1/2), (1/2, 1/2, 0),$$

respectively.

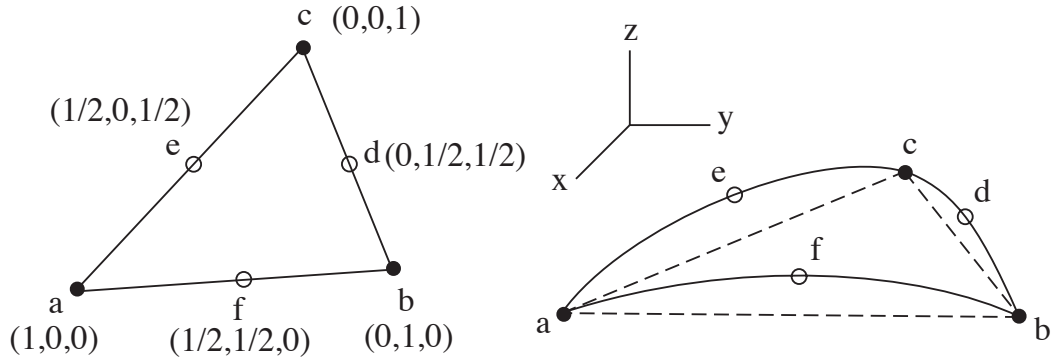


Figure 4.8: Barycentric space and physical space. On the left is a planar triangle with 6 points on them, labeled by their barycentric coordinates. On the right is the corresponding quadratic panel in the physical space.

In Figure 4.8, on the left we draw 6 points on a planar triangle with their barycentric coordinates, and on the right we draw the physical quadratic panel defined over those six points. In contrast to Figure 4.6, we emphasize the curved triangle formed by all 6 points and use solid curves for it because it plays an important role in the refinement process. The linear triangle formed by the passive points $\mathbf{a}, \mathbf{b}, \mathbf{c}$ was used in evaluating the Biot-Savart integral (4.1) and plays a less important role in refinement, and hence is dashed in this redrawing.

Now we describe the refinement process. The refinement criteria generalize those used for the 2D and axisymmetric cases to the fully 3D case. We follow a similar path in explaining them. An edge is the line segment connecting two active points

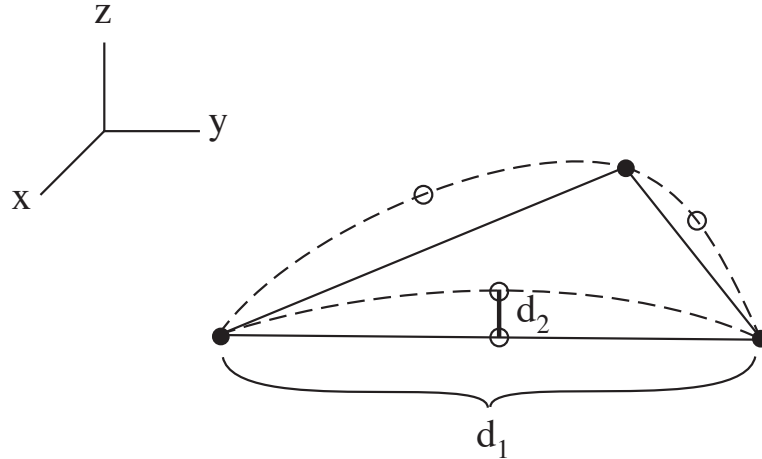


Figure 4.9: Two criteria are checked in the refinement process. d_1 is the edge length. d_2 is the distance between an edge's midpoint and the associated passive point.

on a panel, and we note that there is a passive point associated with each edge. We refer to Figure 4.9. After each time step, two quantities are checked for each edge, (1) the length d_1 of the edge. (2), the length d_2 between the edge's midpoint and the passive point associated with the edge. The algorithm uses two thresholds, ϵ_1 and ϵ_2 . If

$$(4.24) \quad d_1 > \epsilon_1,$$

then the edge length is too large and the discretization of the sheet surface is losing resolution. If

$$(4.25) \quad d_2 > \epsilon_2,$$

then the sheet is developing a large curvature locally. In either case, the edge will be split, i.e. the passive point becomes active. Note that these strategies are analogs of the 2D and axisymmetric cases as explained in Chapter III.

Figure 4.10 illustrates how a panel is subdivided and particles are inserted. As shown in Figure 4.10(a), if it is decided that edge **ac** will be refined, then panel **abc** is split into four new panels and the passive point **p** associated with edge **ac** becomes

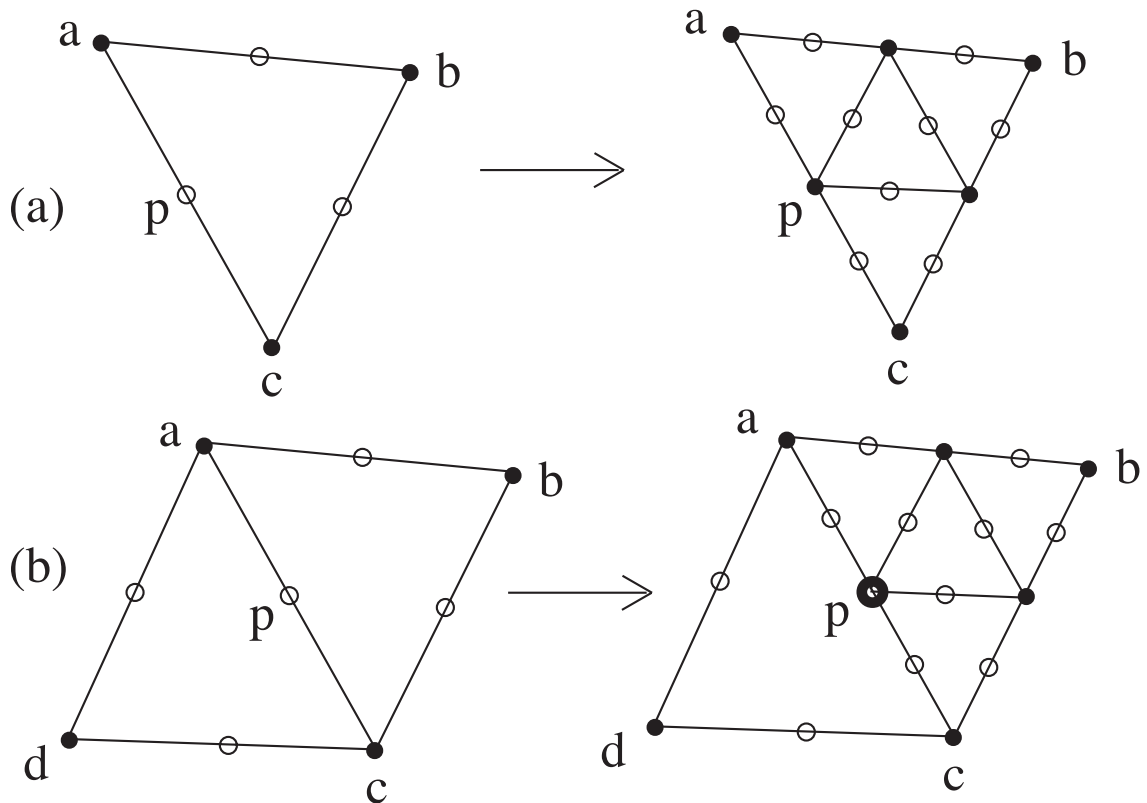


Figure 4.10: Panel subdivision and particle insertion. (a) It is decided that edge ac will be split, then the panel abc splits into four new panels and particle p becomes active for some of the new panels. (b) puts panel abc in the surrounding panels. Particle p remains passive for panel acd after the splitting and is plotted with a thick empty dot. Solid dots (\cdot) are active points. Empty dots (\circ) are passive points.

active for some of the new panels as shown in Figure 4.10(a). Figure 4.10(b) shows the panel abc in the surrounding environment. We can see that even though panel abc is split, its neighboring panel acd remains intact and particle p is still passive for panel acd . Passive points for new panels generated from splitting panel abc are obtained by interpolation using Bezier patches over both panel abc and panel acd as described in the previous subsection.

4.4 Tree-code for Evaluating the Sheet Velocity

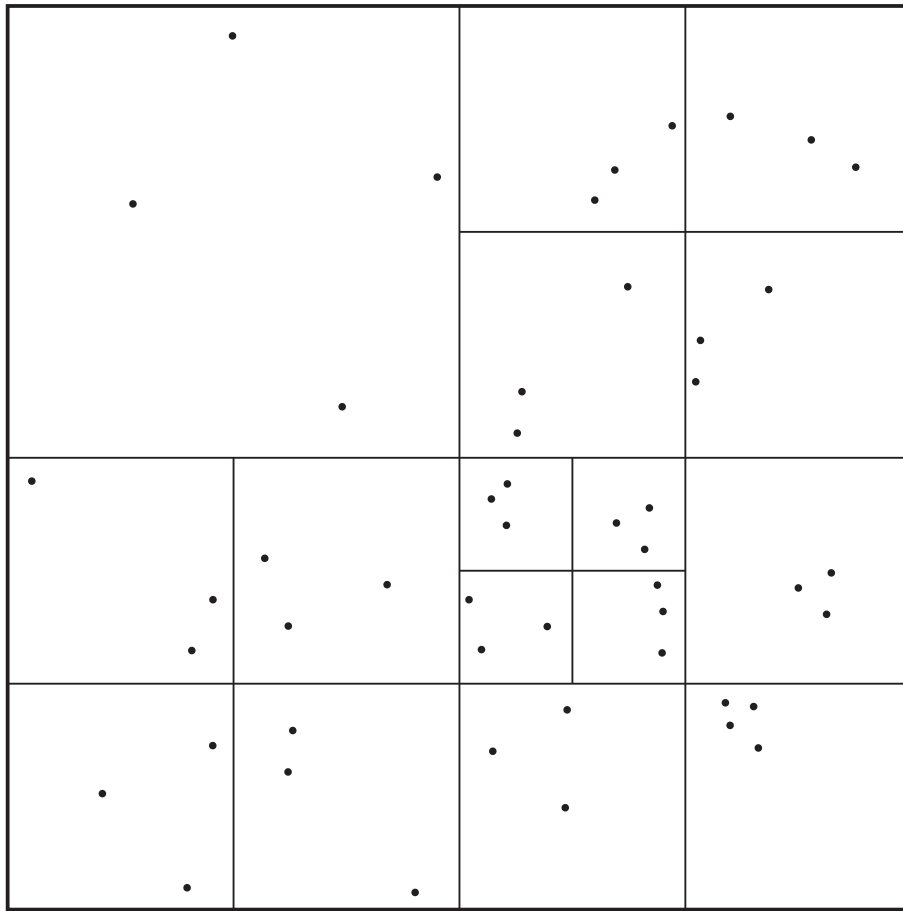
The focus of this thesis is on the triangular panel-particle method for vortex sheet motion, but a tree-code is used to evaluate velocities, and hence the following description is added for completeness.

Because the number of computational points N needed for a 3D vortex sheet simulation is generally large, a naive direct summation algorithm for evaluating the velocity field is not practical as it has operation count $O(N^2)$ and hence is too costly. Fortunately, there are a variety of fast tree-codes available for N -body problems, which reduces the operation count to $O(N\log N)$.

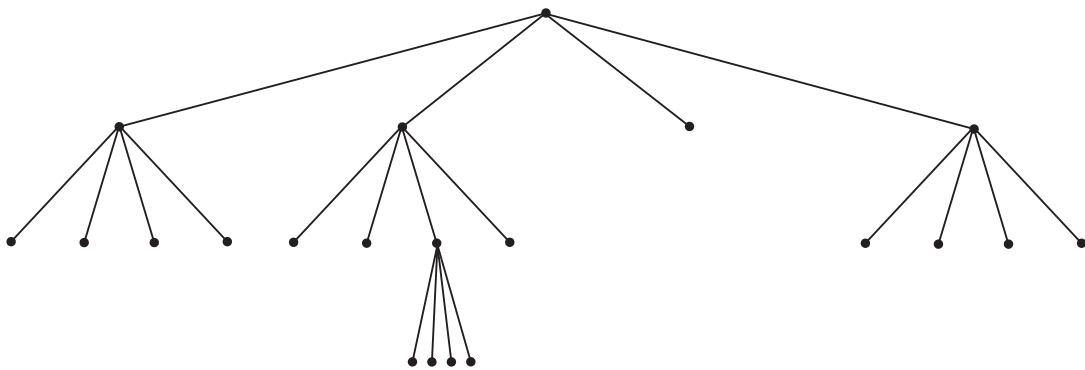
The fundamental idea of a tree-code for particle simulations is a divide-and-conquer strategy. A tree-code is often applied in particle simulations where every particle interacts with every other particle. The tree-code divides the domain containing all the particles into hierarchical clusters, with the root cluster containing all the particles. Rather than evaluating pair-wise particle interactions, a tree-code computes particle-cluster interactions when the size of a cluster is small compared to the distance between a particle and the cluster. Cluster-cluster interactions can also be used, and their effectiveness is under investigation by researchers.

The Barnes and Hut [5] tree-code divides the space evenly into four children for a two dimensional space. They approximate a cluster by a single particle at the cluster center. Figure 4.11 is a schematic of a tree structure with 4 levels in 2D.

Greengard and Rokhlin [21] developed the Fast Multipole Method (FMM) for the case in which the kernel is a harmonic function. A Laurent expansion in 2D and a spherical harmonic expansion in 3D were used in their algorithm. They used higher order expansions, in contrast to earlier fast algorithms. They introduced the



(a)



(b)

Figure 4.11: Tree formation. (a) physical tree in 2D space with four levels. (b) corresponding logical tree represented as a data structure.

idea of using both a far-field expansion and a near-field expansion to optimize the computational cost. Zhao [51] proposed a FMM using Cartesian Taylor expansions rather than spherical harmonics expansions for problems where the interaction kernel is the Newtonian potential.

The Rosenhead-Moore kernel (2.10) is not harmonic, and a Taylor expansion in Cartesian coordinates can be used. Draghicescu and Draghicescu [15] developed a tree-code using Cartesian Taylor expansion to compute a vortex sheet in a two dimensional flow, and they achieved an operation count of $O(N\log N)$.

The tree-code used in this thesis was developed by Lindsay [34] and Lindsay and Krasny [33]. They expanded the work of Draghicescu and Draghicescu [15] from 2D to 3D. More specifically, they derived and implemented a recurrence relation for the Cartesian Taylor coefficients for the regularized Biot-Savart kernel (2.10) in 3D. They also introduced a varying order expansion, which estimates the error and the execution time of an order p expansion and chooses an optimal p adaptively to reduce the computational cost. The tree-code in Lindsay [34] only used particle-cluster interactions.

The accuracy and efficiency of the tree-code are controlled by several parameters. First, when the root cluster is divided into cascading levels of clusters, it may not be optimal to reach the lowest level where every leaf only has one particle. Instead, the tree-code sets a parameter N_c so that any cluster containing less than N_c particles is not divided further. Second, the tree-code can in principle compute and use all the terms in the Taylor series expansion. But computing and storing a large number of Taylor coefficients can add an overhead that slows the algorithm in the end. A maximum allowable order of expansion P_{max} is set in the tree-code, and the code chooses adaptively whether to perform an expansion of order $P \leq P_{max}$ or a direct

summation adaptively. Third, there is error control available for the tree-code, and the code takes a tolerance ϵ as a parameter such that the error in the evaluated velocity is less than ϵ . For all the simulations to be presented in later chapters, we used the parameters $N_c = 500$, $P_{max} = 8$, and $\epsilon = 0.001$. We have tested these parameters to ensure that they provide sufficient accuracy, and yet are still efficient.

CHAPTER V

Vortex Ring Computations

Understanding the dynamics of vortex rings is important because ring structure appears frequently in nature. Fortunately, vortex rings can be generated in the lab and the results can be used as a benchmark for numerical simulations.

This chapter presents numerical simulations of two problems, (1) a single vortex ring undergoing azimuthal instability, and (2) the oblique collision of two vortex rings. In the first problem, perturbations grow along the vortex core of an initially axisymmetric vortex ring and cause the ring to break down. In the second problem, as two vortex rings collide at an oblique angle, vortex reconnection causes the two rings to merge into a single ring and then split again.

This chapter is organized as follows. For each of the two problems described above, first we discuss previous experimental studies, then we present simulations using the triangular panel-particle method described previously in the thesis.

5.1 Experiments on a Single Vortex Ring

Vortex rings are fundamental structures in fluid motion and they have been studied by many experimentalists, so a complete review is impossible. Shariff and Leonard [45] and Lim and Nickels [32] are comprehensive references for vortex rings. Now we

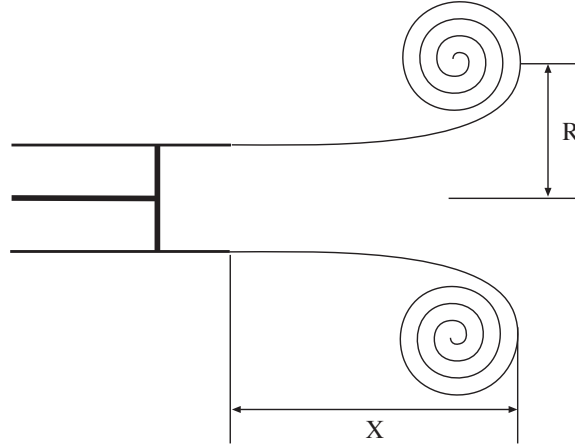


Figure 5.1: Schematic of the experiment by Didden [14]. An axisymmetric vortex ring is generated by forcing fluid out of a pipe. A cross section of the ring is drawn. The ring radius grows like $R \sim t^{2/3}$. The axial distance X between the the vortex core and the pipe exit grows like $X \sim t^{3/2}$.

first review experimental work on axisymmetric vortex rings.

In labs, vortex rings can be generated by forcing fluid out of a circular pipe as was illustrated in Figure 1.3. The fluid is often dyed to assist in observation. The distribution of vorticity in a vortex ring causes the material particles to rotate around the core, while propagating along an axis. This axis is not to be confused with the vortex core axis, which is a closed curve. To differentiate between them, as was shown in Figure 1.2 we call them the propagation axis and the core axis.

Figure 5.1 shows a schematic view of the experiment by Didden [14] in which an axisymmetric vortex ring was generated by forcing fluid out of a circular pipe. The vortex core axis was circular and the ring radius is denoted R . The axial distance between the core and the pipe exit is denoted X . The growth rates $R \sim t^{2/3}$ and $X \sim t^{3/2}$ were observed.

Auerbach [2] performed an experiment for a planar vortex pair and arrived at similar conclusions regarding the growth rates as Didden [14]. A planar vortex pair is a 2D analog of an axisymmetric vortex ring and they have similar cross sections.

The only difference is that in a planar vortex pair the vortex filaments are parallel straight lines while in an axisymmetric vortex ring the filaments are circles.

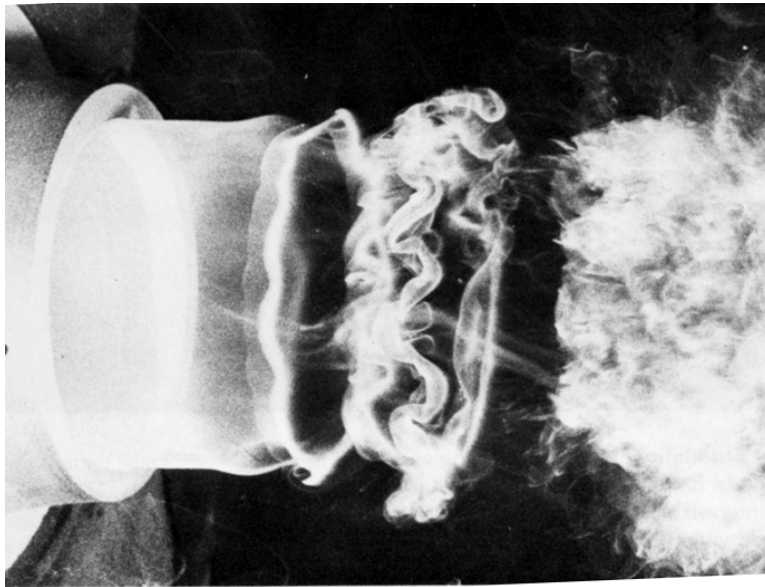


Figure 5.2: Photo from Van Dyke [17] visualizing an experiment in which the azimuthal instability of a vortex ring is studied. The vortex ring was initially axisymmetric, then the azimuthal perturbations cause it to lose axisymmetry and become turbulent.

It is well known that as a vortex ring propagates, it remains laminar initially but eventually sinusoidal perturbations develop along the azimuthal core axis and lead to turbulence. Figure 5.2 is a photo from Van Dyke [17], showing that the vortex ring has lost axisymmetry and is in an unstable stage. Beside measuring the growth rates of a vortex ring, Didden [14] also observed the azimuthal instability of vortex rings at later time similar to what is shown in Figure 5.2. We present in the next section numerical simulations of the azimuthal instability of a single vortex ring.

5.2 Computational Results on Vortex Ring Azimuthal Instability

To use a vortex sheet to simulate a vortex ring, we need to generate an initial mesh on the circular disk. The exponential map $w(z) = e^z$ is used in this process.

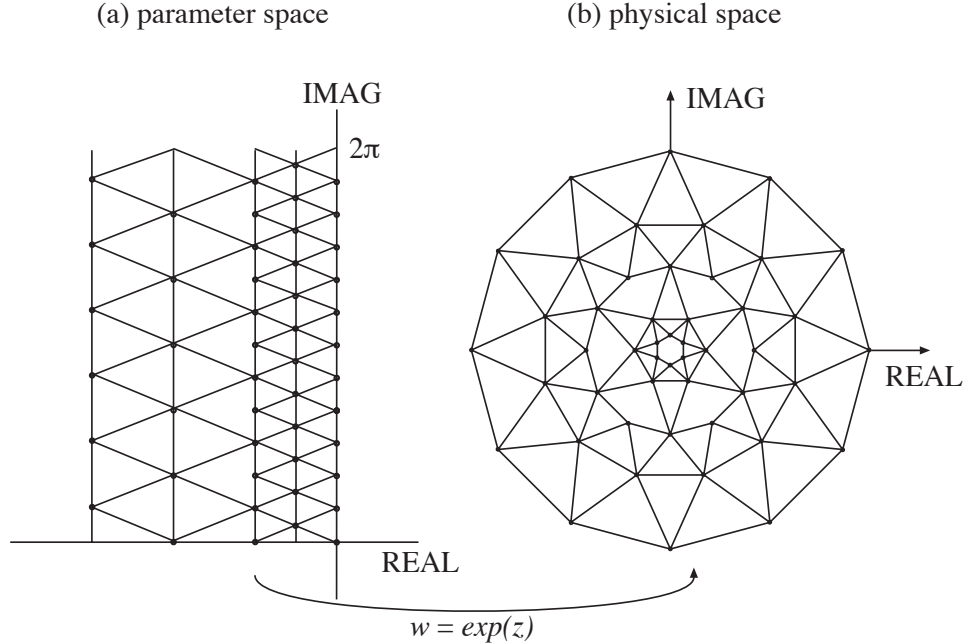


Figure 5.3: A Schematic of the conformal mapping $w(z) = e^z$ as applied to the generation of a triangular mesh on the unit disk. The physical mesh shown on the right is generated after one run of the refinement procedure described in section 4.3. More runs are needed if a finer mesh is desired.

Figure 5.3 shows a schematic of such a map. The function $w(z) = e^z$ is a conformal mapping that maps the half-infinite strip $D = (-\infty, 0] \times [0, 2\pi)$ in the complex plane into the unit disk.

A triangulation of the strip D leads to a triangulation of the disk, which is the initial physical space in the simulation of a single vortex ring. We can not take the entire domain D as it is infinite, but this problem can be solved as follows. We note that $w(z)$ maps the line segment $x = 0, 0 \leq y \leq 2\pi$ to the outer edge of the unit disk, and maps the region at infinity in D to the disk center. Since the circulation distribution on the disk is $\Gamma = \sqrt{1 - r^2}$ and $d\Gamma/dr = -r/\sqrt{1 - r^2}$ is the vortex sheet strength, there is essentially no vorticity at the disk center. So we can leave out a small region around the center. To do this, we ignore the region at infinity in D and take $\tilde{D} = [-\pi, 0] \times [0, 2\pi]$ as the parameter space. Then $w(z) = e^z$ maps \tilde{D} to the annulus with an inner radius of $e^{-\pi} = 0.0432$ and an outer radius of $e^0 = 1.0$.

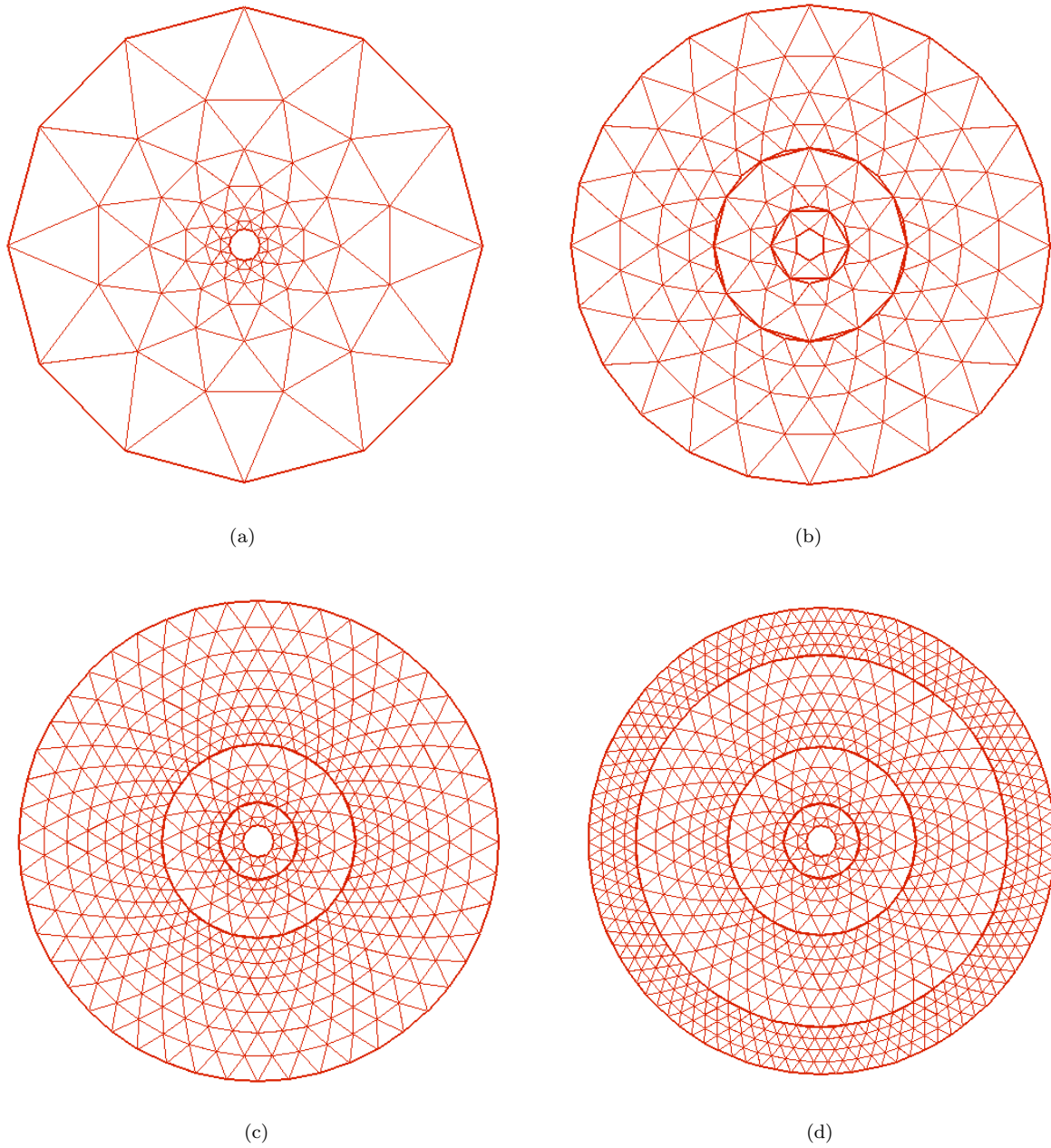


Figure 5.4: Initial mesh generation by repetitively applying the refinement process. Three repetitions are shown.

We triangulate \tilde{D} using equilateral triangles of the same size, and this leads to a triangulation of the unit disk. The refinement procedure as described in section 4.3 is repeatedly applied to this mesh to generate the initial computational mesh on the disk. The number of repetitions determines how fine the initial mesh is. Figure 5.4

shows this process with 3 repetitions.

For initial perturbations, we used two wave numbers, $k = 5$ and $k = 8$ as in Kaganovskiy [22]. The following functions are added to the z -coordinate of all computational points for the two modes at $t = 0$,

$$(5.1) \quad \epsilon(r, \theta) = 0.1 r^2 \sin(5\theta), \quad \epsilon(r, \theta) = 0.1 r^2 \sin(8\theta),$$

where $r^2 = x^2 + y^2$ and θ is the azimuthal angle in the cylindrical coordinates (r, θ, z) .

The smoothing parameter in the regularized Biot-Savart kernel (2.10) is $\delta = 0.1$. The time step is $\Delta t = 0.05$. Recall that in the refinement process, there are two tolerance parameters ϵ_1 and ϵ_2 as were defined in equation (4.24) and (4.25). These two parameters are set to be $\epsilon_1 = 0.1$ and $\epsilon_2 = 0.0025$ in the simulation. Those parameters are tested to ensure that the computations are fully resolved, and yet they are not too small to sacrifice efficiency.

Figure 5.5 shows a time sequence of the simulation for wave number $k = 5$, while the case $k = 8$ is shown in Figure 5.7. We note that all the pictures of the 3D simulations in this thesis are rendered by TecPlot version 10.0. In Figure 5.5, we can see that wave number $k = 5$ is stable and the initial perturbation does not grow much. Figure 5.7 shows that wave number $k = 8$ is unstable and the outer filament developed hairpins. We believe that whether a mode is stable depends on the smoothing parameter in the regularized Biot-Savart kernel (2.10).

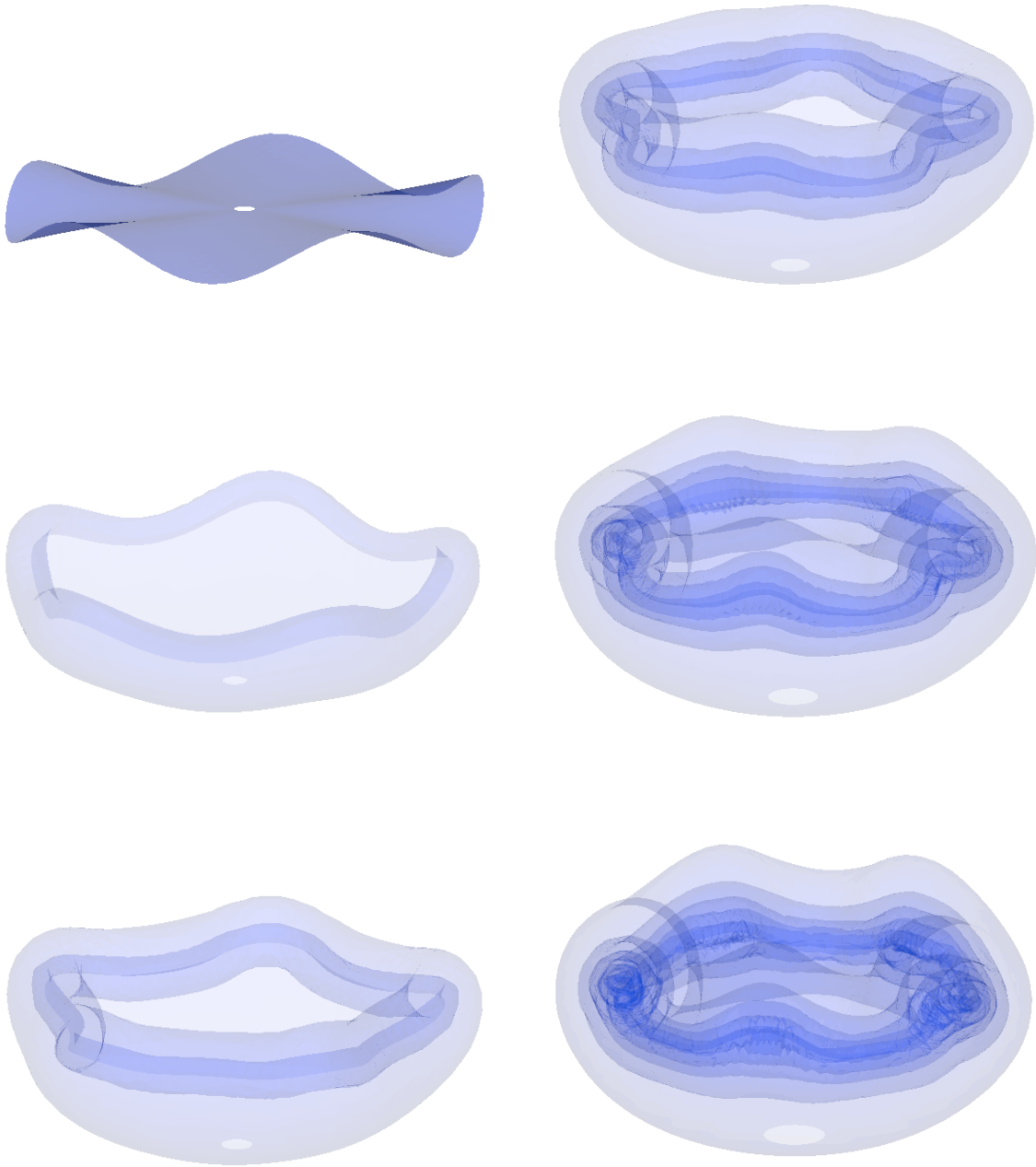
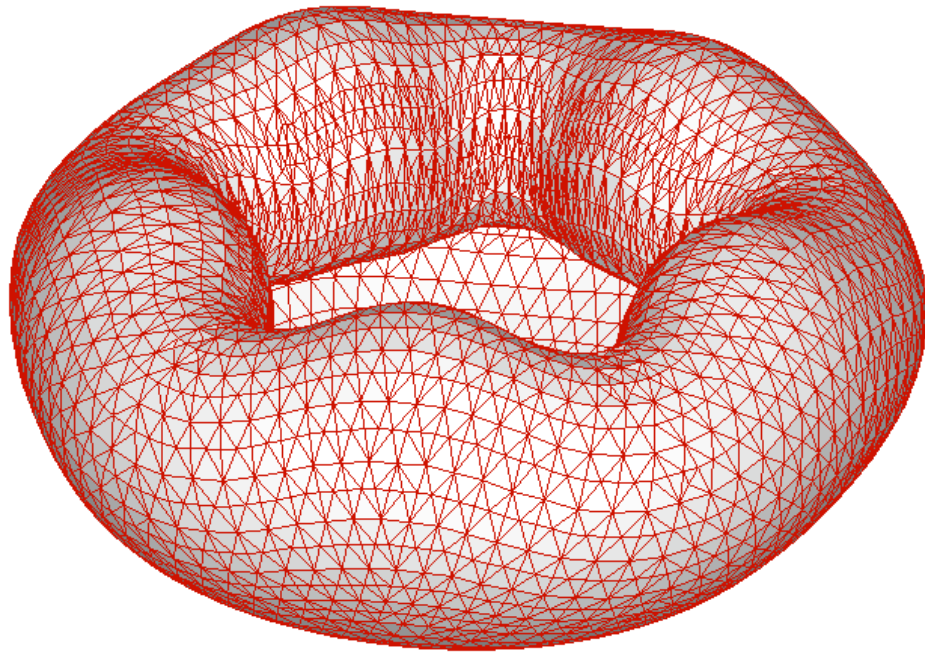
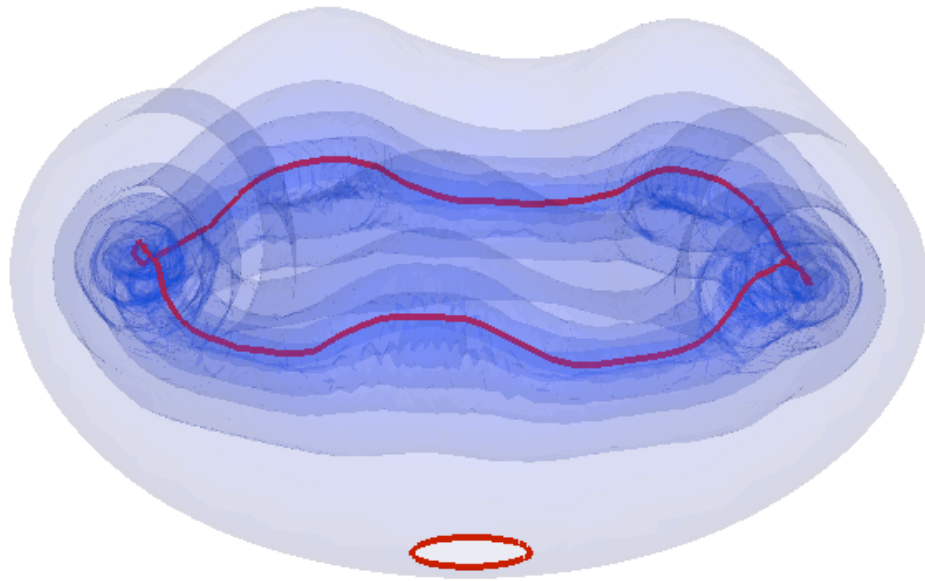


Figure 5.5: Time sequence of azimuthal instability of a single vortex ring at time $t = 0, 1, 2, 3, 4, 5$, ordered top to bottom, then left to right. The perturbation has wave number $k = 5$. As can be seen in the picture, the perturbation does not grow much from $t = 0$ to $t = 5$.



(a)



(b)

Figure 5.6: Final time $t = 5.0$ from the time sequence in Figure 5.5. (a) Mesh on the surface. (b) Transparent view. Two filaments are shown, the larger one is the outer edge, while the smaller one is inner edge after deleting a small center region in the initial mesh generation. The outer filament expanded by a large amount because circulation is concentrated there. In contrast, the inner filament did not expand much.

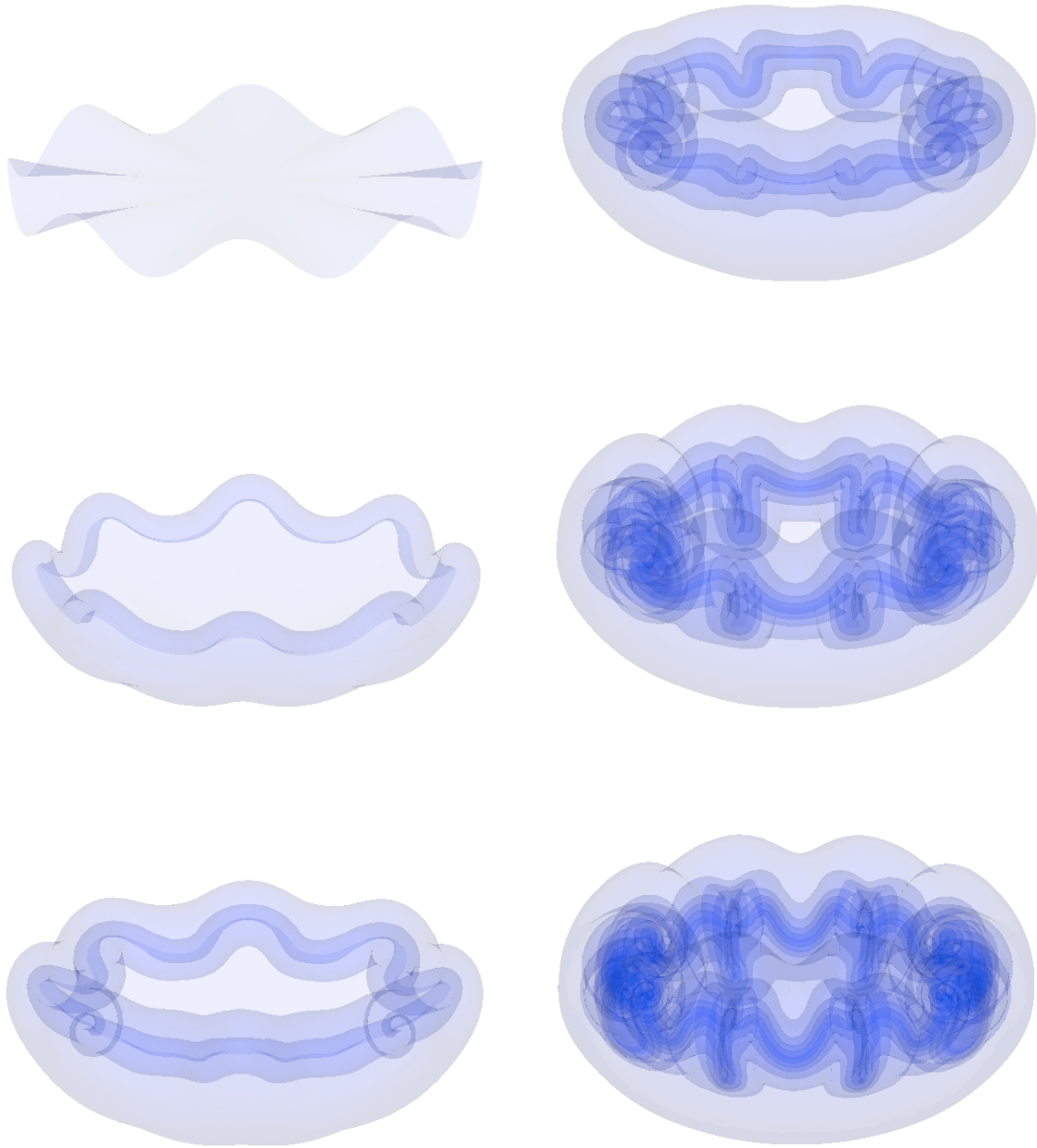


Figure 5.7: Time sequence of azimuthal instability of a single vortex ring at time $t = 0, 1, 2, 3, 4, 5$, ordered top to bottom, then left to right. The perturbation has wave number $k = 8$. As can be seen in the picture, the perturbation grows considerably from $t = 0$ to $t = 5$.

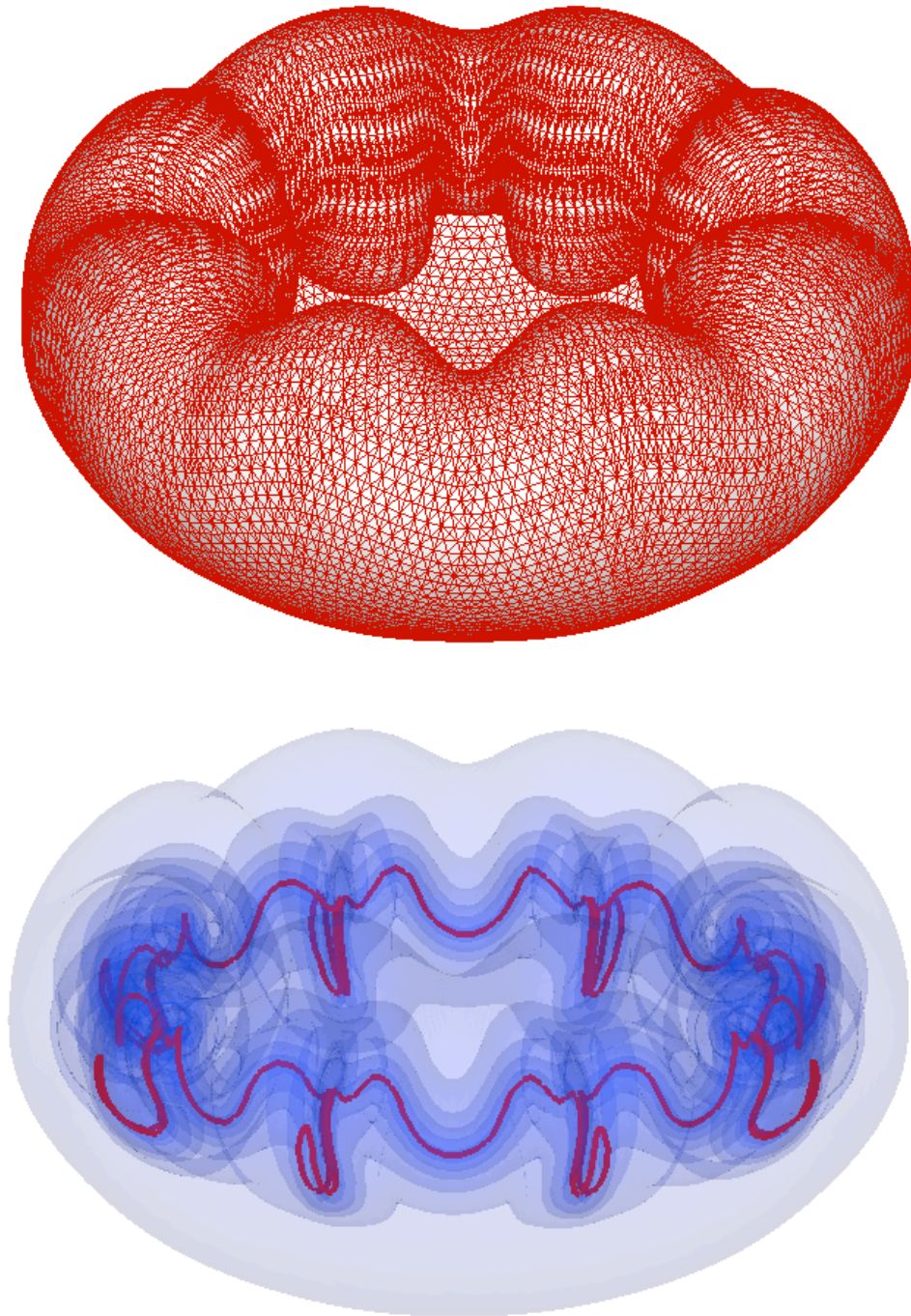


Figure 5.8: Final time $t = 5.0$ from the time sequence in Figure 5.7. (a) Mesh on the surface. (b) Transparent view. Only the outer filament is shown to assist visualization in contrast to the case $k = 5$, the disk center is filled by adding computational points. As can be seen from the picture, hairpins form on the outer edge.

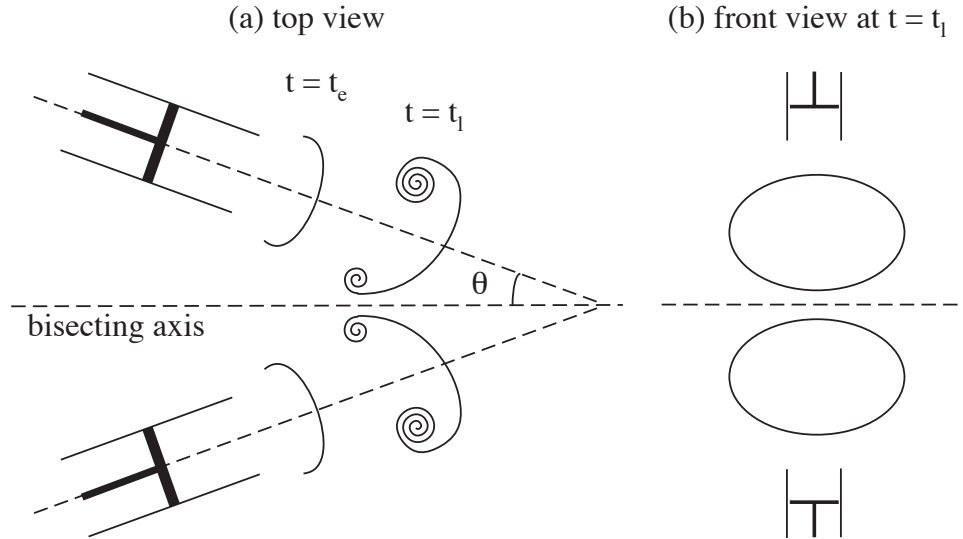


Figure 5.9: Schematic of experimental set-up for oblique collision of two vortex rings. θ is the collision angle. A top view is shown in (a). At an early time $t = t_e$, the two rings have little effect on each other and are axisymmetric. As the two rings come closer at a later time $t = t_l$, the axisymmetry is lost. A front view at the later time $t = t_l$ is shown in (b), where only the vortex core axes are drawn.

5.3 Experiments on Oblique Collision of Two Vortex Rings

Many experiments have been conducted on the interaction of two vortex rings, including Fohl and Turner [19], Kambe and Takao [23], Oshima and Asaka [38], Oshima and Izutsu [40], Schatzle [44], and Lim [30]. In this section we review experimental work on the oblique collision of two vortex rings. Figure 5.9 is a schematic of the experimental set-up showing two circular pipes whose axes are at an angle θ from the bisecting axis. A piston forces fluid out of each pipe causing an axisymmetric vortex ring to form. The experiment shows that the two rings stay axisymmetric at an early time $t = t_e$, but as they move closer, the axisymmetry is lost at a later time $t = t_l$. Figure 5.9(a) is a top view, if we look to the ring fronts in the direction of the bisecting axis, we would see the front view as shown in Figure 5.9(b).

When the two rings come close to each other, they deform due to viscous diffusion. The interaction between the two vortex rings leads to vortex reconnection which we

explain next.

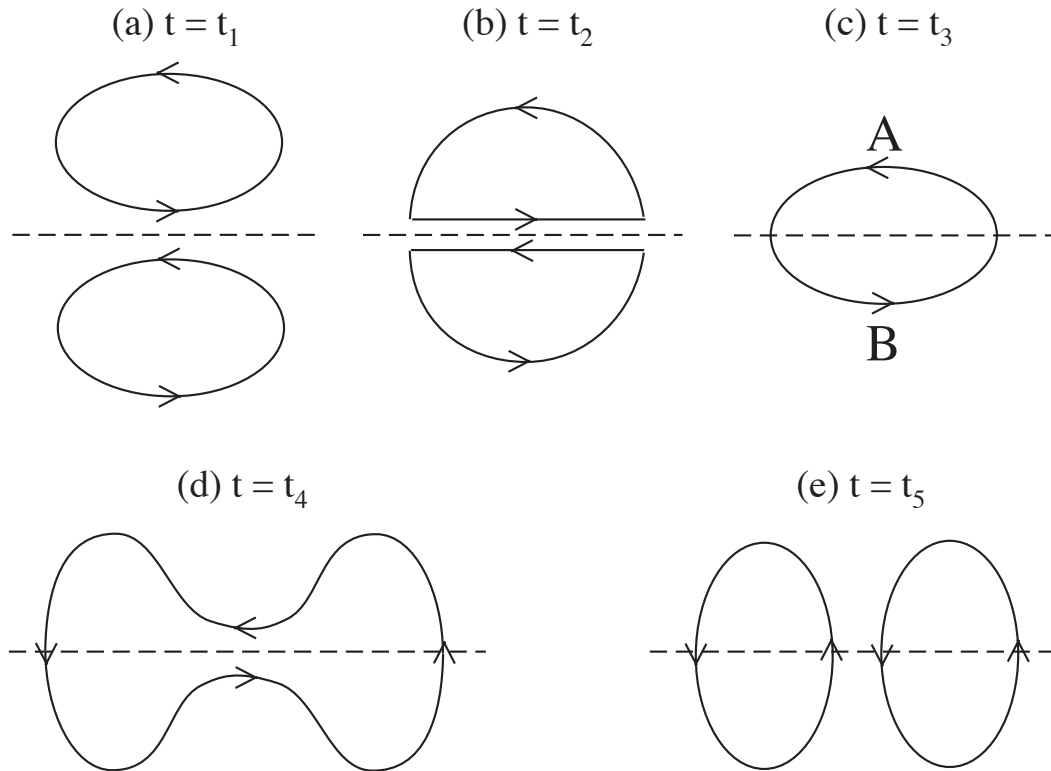


Figure 5.10: Schematic of two vortex rings colliding obliquely, front view. The dotted line denotes the bisecting plane between the two rings, the plane where collision occurs. As the two rings carrying opposite vorticity come close (a), the first vortex reconnection occurs (b) and they form one single ring (c). As time progresses further, a second reconnection occurs (d) and the single vortex ring splits into two counter rotating rings (e). Each new ring consists of one half from each of the original two rings.

Figure 5.10 shows a schematic time sequence of the reconnection of two rings. In this figure, we draw two closed vortex filaments to represent the vortex rings. Figure 5.10(a) shows that the rings propagate initially as two counter-rotating rings and move towards the plane of collision. After they come in contact, vorticity cancellation occurs since the vorticity is of opposite sign as shown in Figure 5.10(b). This interaction of vorticity merges the two rings into one single ring as shown in Figure 5.10(c). The portions of the vortex rings which are not in contact, denoted *A* and *B* in Figure 5.10(c), are still propagating towards each other and this leads to the picture in Figure 5.10(d). A second vortex reconnection occurs and the single vortex

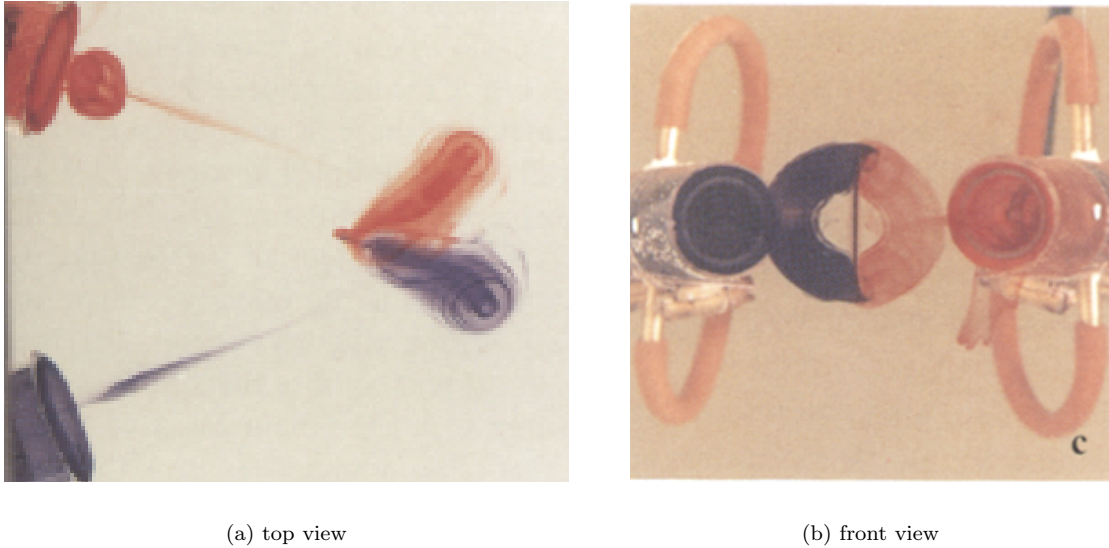


Figure 5.11: Flow visualization by Lim [30]. Two vortex rings are generated as fluid is forced out of circular pipes. The pipe axes are positioned so that the collision angle $\theta = 17.5^\circ$. The two rings eventually collide and then reconnect to form two new rings propagating in different planes.

ring breaks up into two new rings (e).

Fohl and Turner [19] conducted an experiment of two vortex rings colliding at an oblique angle. They observed that if the collision angle θ as shown in Figure 5.9 is greater than 16° , then the rings reconnect as depicted in Figure 5.10. However, for a smaller value of θ , they did not observe reconnection. Hence there is a critical angle $\theta_c = 16^\circ$ for reconnection.

Kambe and Takao [23], Oshima and Asaka [39], Oshima and Izutsu [40] also observed a critical angle. But Oshima and Asaka [39] found that a smaller critical angle $\theta_c < 16^\circ$ was needed for the two rings to reconnect and form two new rings if the two original rings have larger circulation.

Schatzle [44] conducted a similar experiment using a larger collision angle $\theta = 30^\circ$ and he observed vortex ring reconnection. He also found that the circulation of the rings decreases during the collision, and he attributed this to the effect of viscosity.

Lim [30] performed an experiment in which an axisymmetric vortex ring hits a wall at an oblique angle. He also did an experiment in which two axisymmetric vortex rings collide in free space at an oblique angle. Figure 5.11 is a photo from his experiment for the oblique collision of two rings. In this case, two vortex rings were generated using the pipe-piston apparatus. The collision angle in the experiment was $\theta = 17.5^\circ$. It was found that the two rings collide and merge into a single ring, and then the single ring splits into two new rings propagating in different planes.

Motivated by all of these experiments reviewed above, in the next section we will present the simulations of the oblique collision of two vortex rings.

5.4 Computational Results on Oblique Collision of Two Vortex Rings

In simulating this problem, we used the same initial mesh as in section 5.2 for the simulation of a single vortex ring undergoing instability. Since the problem is symmetric, only one of the two rings is computed, and the other is obtained by reflecting the data. We used the same initial circulation $\Gamma(r, 0) = \sqrt{1 - r^2}$ as was used in the single ring case, where r is the distance to the disk center.

Figure 5.12 shows a time sequence of the simulation. Initially the centers of the two rings are located at $(\pm 2.5, 0, 0)$, which is close to the experimental configuration in Lim [30]. The collision angle is $\theta = 17.5^\circ$, which is also what Lim [30] used. The smoothing parameter in the regularized Biot-Savart kernel (2.10) is $\delta = 0.2$ in contrast to the $\delta = 0.1$ used in the simulation of a single ring undergoing instability, because we found that using $\delta = 0.1$ would make the computations too costly for this case. The time step $\Delta t = 0.1$. The two parameters for refinement are $\epsilon_1 = 0.1$ and $\epsilon_2 = 0.0025$.

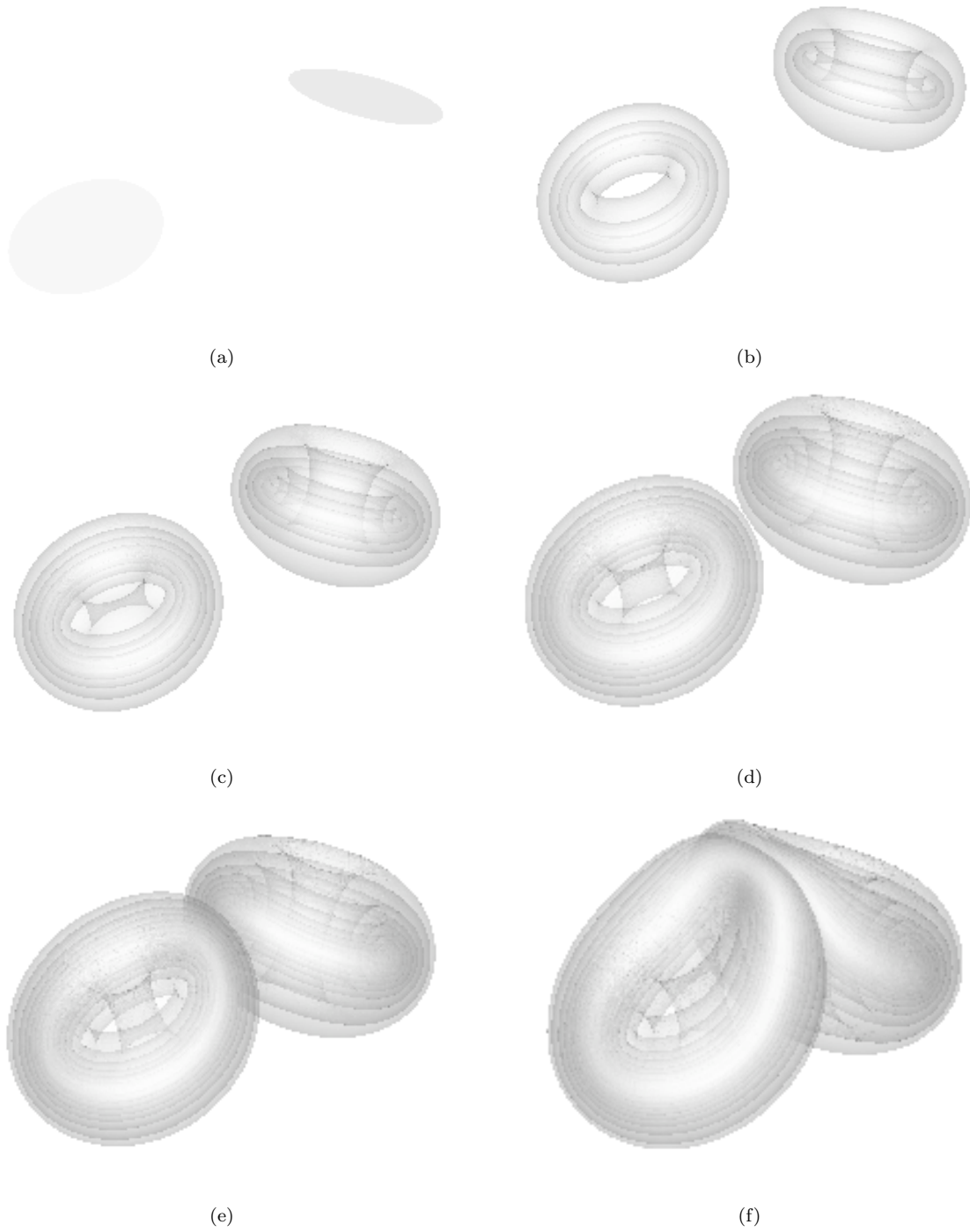


Figure 5.12: Time sequence of simulation of oblique collision of two vortex rings at time $t = 0, 8, 12, 16, 20, 24$, ordered top to bottom, then left to right.

We can see that as the two rings come close to each other, the axisymmetry is lost. Unfortunately, we could not go further because the computations became too costly at later times with more and more computational points. Figure 5.13 is a close-up of the final time $t = 24.0$ of the sequence in Figure 5.12. We present plots from the same viewpoints as in the experiment shown in Figure 5.11.

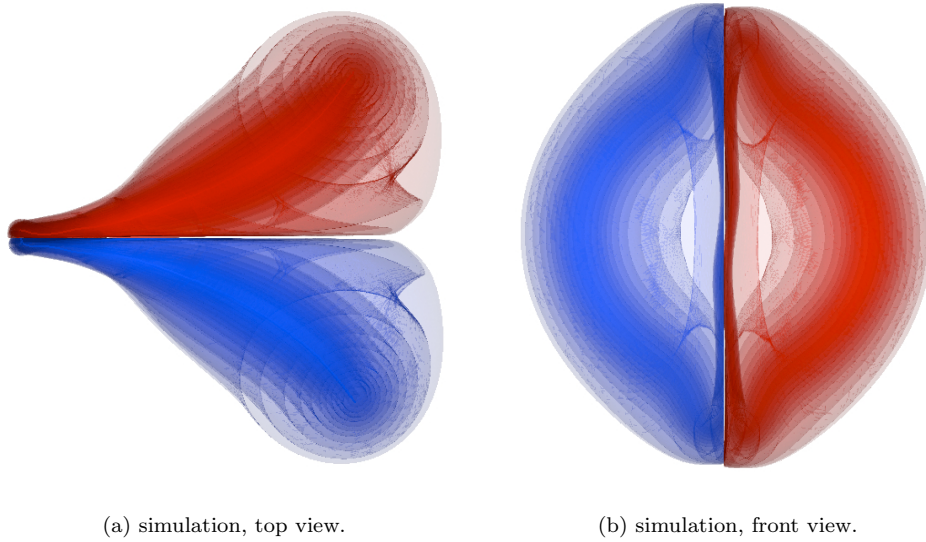


Figure 5.13: Oblique collision of two vortex rings.

CHAPTER VI

Vortex Sheet Computations in 3D Density-Stratified Flow

Density-stratified flow has many applications, for example, the ocean is slightly stratified in density because of different salinity at different depths. This chapter presents numerical studies of density-stratified flow using the vortex sheet model previously described.

This chapter is organized as follows. First we review relevant previous work on density-stratified flow, which includes both numerical and experimental studies. Then we present the numerical simulations using the method developed in this thesis.

6.1 Review of Previous Work on Density-Stratified Flows

First we review the numerical work on density-stratified flow by Baker, Meiron, and Orszag [3, 4], and Stock [46]. Then we discuss experimental work on density-stratified flow by Thomson and Newall [48] and Estevadeordal, Meng, Gogineni, Goss and Roquemore [18], in which a drop of heavy fluid settles in a background of lighter fluid.

6.1.1 Rayleigh-Taylor Instability

Rayleigh-Taylor instability is caused by density stratification. When a layer of heavy fluid lies above a lighter one, the interface is susceptible to small perturbations as the heavy fluid on top has the tendency to penetrate into the lighter fluid below. When the geometry of the problem is simple, an explicit dispersion relation can be derived by linear stability analysis [16].

Baker, Meiron, and Orszag [3] considered an interface between two fluids of different densities. The setting of their study was in free space and they modeled the interface as a vortex sheet. As the flow evolves, vorticity is generated on the interface due to the density jump. They derived the equation (2.31) for circulation generation on the sheet surface. Computational results were presented for the evolution of an interfacial wave. Baker, Meiron, and Orszag [4] later extended the model presented by Baker et al. [3] to the axisymmetric case and the fully 3D case.

Stock [46] presented a vortex-in-cell method for 3D vortex sheet simulations. He considered flows with small Atwood ratio A , in some cases with the Boussinesq approximation and in other cases with a full density jump accounted for. In one problem he studied a thermal, which is a volume of light fluid surrounded by ambient heavier fluid. In another computation he simulated a vortex ring hitting a planar density interface. He compared simulations for both head-on and oblique collision, and for both homogeneous and density-stratified flow.

6.1.2 Experimental Work on Density-Stratified Flow

Thomson and Newall [48] performed an experiment in which they released a spherical drop of heavy fluid in water. Figure 6.1 is a schematic of the process. The three

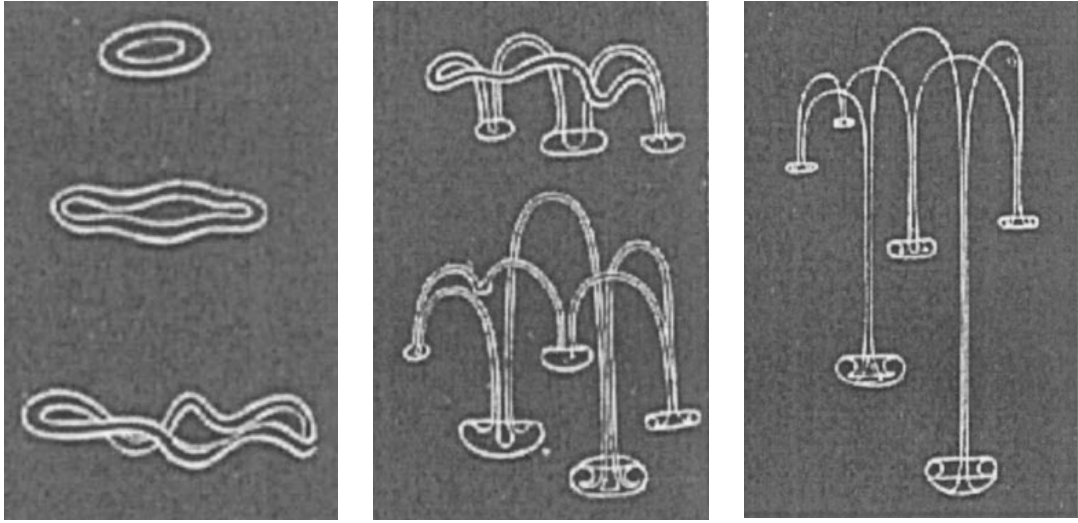


Figure 6.1: Schematic of an unstable vortex ring from the experiment by Thomson and Newall [48], picture taken from Walther and Koumoutsakos [50]. A drop of heavy fluid is released into water. The drop rolls up into a vortex ring which becomes unstable at a later time and secondary rings form. Only the vortex core is drawn. A time sequence is shown, ordered from top to bottom, and from left to right.

frames in the left panel are at earlier times, the two frames in the middle panels are at intermediate times, and the one frame in the right panel is at a later time. As the drop settles, it loses its spherical shape and the interface rolls up into a vortex ring. Since there is a density jump on the interface, vorticity is generated baroclinically as governed by equation (3.20) or (3.22). Vorticity is generated fastest where the interface is vertical since gravity points in that direction. In the initial stage, a large amount of vorticity is generated on the equator while the polar areas are still irrotational. As time progresses, the drop rolls up into a vortex ring while the density interface remains topologically a sphere.

More recently, Estevadeordal, Meng, Gogineni, Goss and Roquemore [18] performed a similar experiment. Figure 6.2 is the visualization of their experiment. In their experiment, they used water suspension of polystyrene to create a heavy drop. They observed a similar vortex ring instability as by Thomson and Newall [48]. In

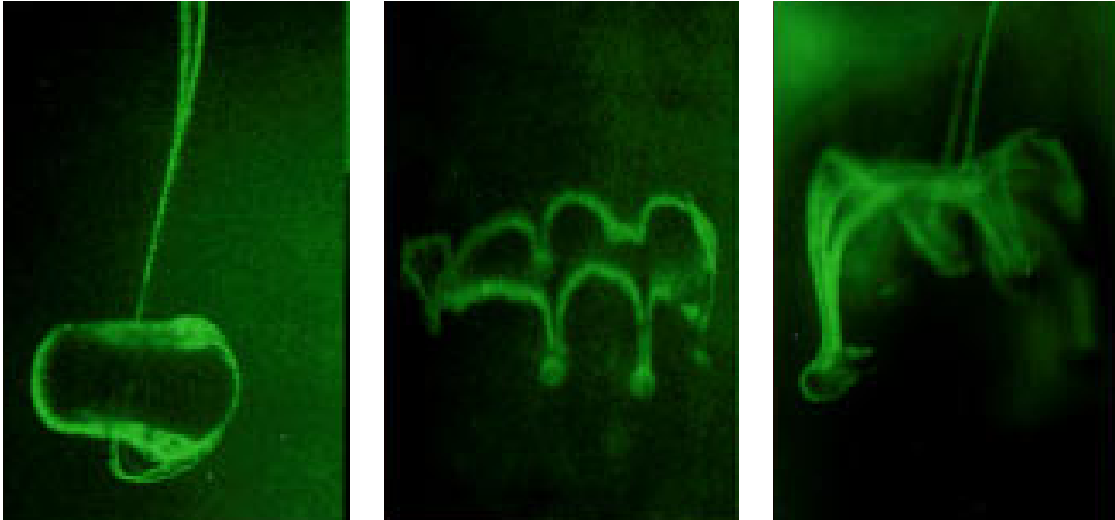


Figure 6.2: Visualization of the experiment by Estevadeordal et al. [18]. A drop of water suspension of polystyrene is released into water and a time sequence is shown. The drop rolls up into a vortex ring which later develops azimuthal instability and secondary rings form.

contrast to Thomson and Newall [48], Estevadeordal et al. [18] also performed another experiment in which the Atwood ratio is smaller. In this case they observed another instability that looks qualitatively different, which they called a bag-shaped instability. Next we present numerical simulations motivated by these experiments.

6.2 Computational Results

In this section we present numerical simulations of a drop of heavy fluid settling in a background of a lighter fluid. We make the Boussinesq approximation and assume that initially there is no vorticity in the flow. Since there is a density jump on the interface between the two fluids, vorticity is generated baroclinically on the surface. As in all the work contained in this thesis, we assume that the flow is inviscid, and hence the density interface can be modelled as a vortex sheet.

A triangular mesh on a sphere can be generated in a number of ways. For example, one can inscribe an icosahedron (a regular polygon consisting of 20 identical

equilateral triangles) in the sphere. Then one can divide each equilateral triangle into 4 smaller equilateral triangles and push all new points onto the sphere. If the mesh is not fine enough, this process is repeated. This approach was adopted by Stock [46] in simulating a thermal rising in a background of slightly heavier fluid.

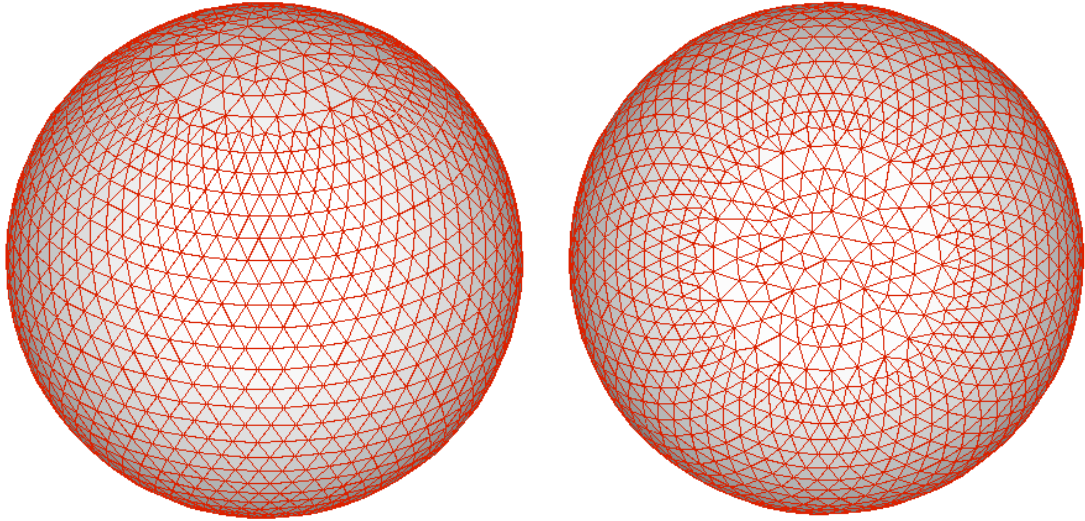


Figure 6.3: Initial mesh on a sphere. Two views are shown, perspective view on the left and top view on the right. The mesh is generated by the advancing front-method which uses the equator as the initial front.

We tried a mesh generated by repetitively dividing an icosahedron, but it generates artificial perturbations. In our simulations, the initial mesh on the sphere is generated using an advancing-front method. The initial front is on the equator, and it propagates to fill up the whole sphere. In the advancing stage, each edge in the front tries to find a candidate point on the sphere so that the point combines with the edge to form a triangle close to being equilateral. Figure 6.3 shows a perspective view of the initial mesh on the sphere and a top view.

We list the parameters used in the simulations. The initial radius of the sphere is $R = 0.5$ and the initial drop is centered at the origin $(0, 0, 0)$. The smoothing parameter for the Biot-Savart kernel (2.10) is $\delta = 0.1$, which is in contrast to the

case for simulating the oblique collision of two vortex rings, where $\delta = 0.2$ was used. The reason for doing this is because the radius of the sphere here is $R = 0.5$, while the radius of the disk was $R = 1.0$ for the vortex ring simulations. We note that a too small δ value causes the computation to be costly, while a too large δ value makes the vortex blob method invalid. The time step is $\Delta t = 0.05$. The parameters for the refinement process are $\epsilon_1 = 0.1$ and $\epsilon_2 = 0.0025$.

An initial perturbation of the form

$$(6.1) \quad \epsilon(r, \theta) = 0.1 r^2 \sin(5\theta),$$

where $r^2 = x^2 + y^2$ and θ is the azimuthal angle in cylindrical coordinates (r, θ, z) , is added to the z -coordinates of all computational points at $t = 0$. The initial condition for circulation is $\Gamma(\mathbf{x}, 0) = 0$.

Figure 6.4 shows a time sequence of the simulation. We can see that mode $k = 5$ appears to be stable, and the secondary vortex rings did not form as in the experiment shown in Figure 6.2. This may be caused by two reasons. First, the smoothing parameter δ we used is too large. A smaller δ value would make the problem more unstable and may force the secondary vortex rings to appear. Second, the wave number $k = 5$ is stable for $\delta = 0.1$. In future work, we will vary the wave number of the perturbation (6.1).

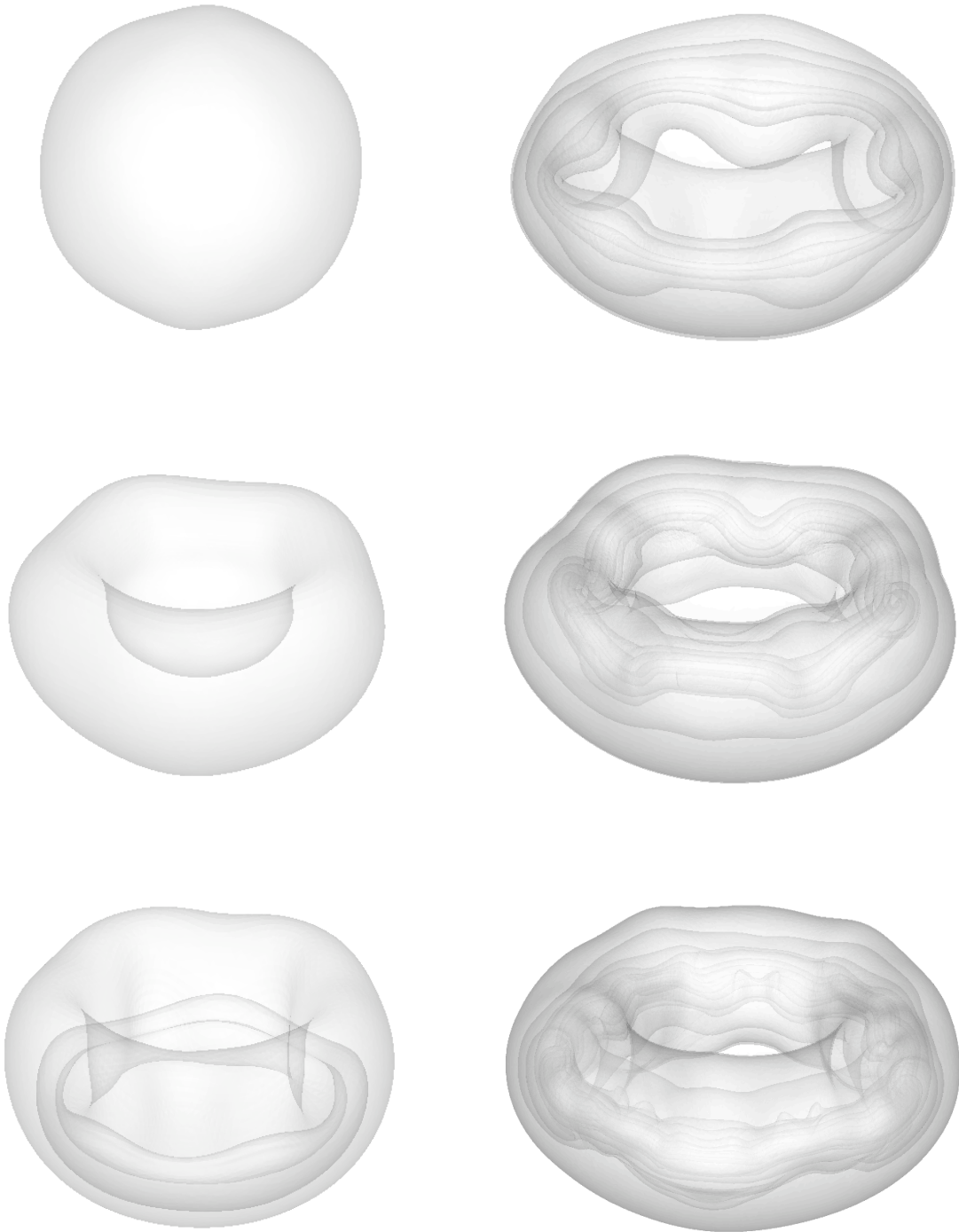


Figure 6.4: Time sequence of simulation for a spherical drop of heavy fluid settling in a background of lighter fluid using the vortex sheet model. The plotted times are $t = 0, 2, 3, 4, 5, 6$, ordered from top to bottom, then from left to right. An initial perturbation of wave number $k = 5$ is added. The initial spherical drop rolls up into a vortex ring but mode $k = 5$ appears to be stable.

CHAPTER VII

Summary and Future Work

7.1 Summary

A new panel method was presented for computing vortex sheet motion for homogeneous and density-stratified flow in 2D, axisymmetric, and 3D geometry. The computations were motivated by experiments in the literature. The algorithm uses a triangular panel-particle method to evolve the sheet surface. The velocities are computed with a Cartesian tree-code.

In Chapter I we introduced vortex sheets, vortex rings, and the work contained in this thesis. Chapter II contains mathematical background of fluid dynamics relevant to the vortex sheet model. That chapter also gave a brief review of the literature on computations of vortex sheet motions. Chapter III described the numerical methods and presented results for vortex sheets in 2D and axisymmetric flows, including both homogeneous and density-stratified cases. Chapter IV explained the discrete panel representation of vortex sheets in a fully 3D flow, and described in detail the numerical methods used in the simulations. The tree-code for computing particle velocity was briefly explained. Chapter V presented results for vortex sheets in 3D homogeneous flow, including a case in which a single vortex ring undergoes azimuthal instability, and a case in which two vortex rings collide at an oblique angle. Chapter

VI presented results for vortex sheets in 3D density-stratified flow, in which a heavy drop of fluid settles in a background of lighter fluid. In this case, vorticity is generated baroclinically on the density interface.

7.1.1 Contributions of Thesis

First, a local quadrature method was successfully implemented. Previously, most methods for computing vortex sheets used a global parametric description. In contrast, the scheme developed here avoids the use of a global parameter space in both the quadrature and panel-particle refinement. This has the potential to provide superior resolution when the sheet surface becomes geometrically complex.

Second, a hierarchical triangular panel-particle representation was developed for 3D vortex sheets. In general, the vortex sheet will expand and distort as it evolves, so mesh refinement is needed to maintain resolution. The hierarchical panel structure makes the mesh refinement easier to implement, and also makes the code simpler, but still accurate. Each panel has a set of active points and a set of passive points. The active points are used in the quadrature. The passive points are used in the refinement procedure, which includes panel subdivision and particle insertion.

Third, a comparison was made between the Boussinesq approximation and the full density jump for density-stratified flow in 2D and axisymmetric case. It can be seen from the numerical results that the full density jump formulation converges to the Boussinesq approximation as the Atwood ratio tends to 0 at a fixed time.

7.1.2 Comparison with Previous Methods and Difficulties

The computation of 3D vortex sheet motion was previously studied using a variety of methods by many authors, including Brady, Leonard, and Pullin [7], Lindsay and Krasny [33], Kaganovskiy [22], and Stock [46], among others. As the sheet surface evolves, stretching and twisting occur which require some method of refinement to maintain resolution. This issue was addressed in all of the work above. The approach adopted in Brady et al. [7] was an advancing-front method, which remeshes the sheet surface after each time step. Lindsay and Krasny [34] inserted a new filament between neighboring ones if they separate too far from each other. On each filament, new particles were inserted if neighboring particles separate too far. Kaganovskiy [22] used a hierarchical quadrilateral panel method in which panels could be locally refined, so that an entire new filament did not have to be added. Hence his method saves computational cost compared with Lindsay and Krasny [33]. Stock [46] used a triangular mesh and a vortex-in-cell method to compute velocity, and refined the sheet representation by splitting edges when they become too long. In our method we represent the sheet surface using a hierarchical triangular panel structure, in which each panel has active points and passive points. The active points are used in computing the vorticity required by the Biot-Savart integral (4.1) and the passive points assist in the refinement procedure.

The challenge faced by all methods for refining on a 3D vortex sheet surface is that as the sheet evolves, non-uniform stretching and twisting occur. If we pick two orthogonal directions on the sheet surface, the stretching rates can vary drastically in these directions. Figure 7.1(a) shows a panel that is equilateral at an early time, but later loses its regularity because of non-uniform stretching.

We can also see twisting of filaments on the sheet surface. Figure 7.1(b) depicts

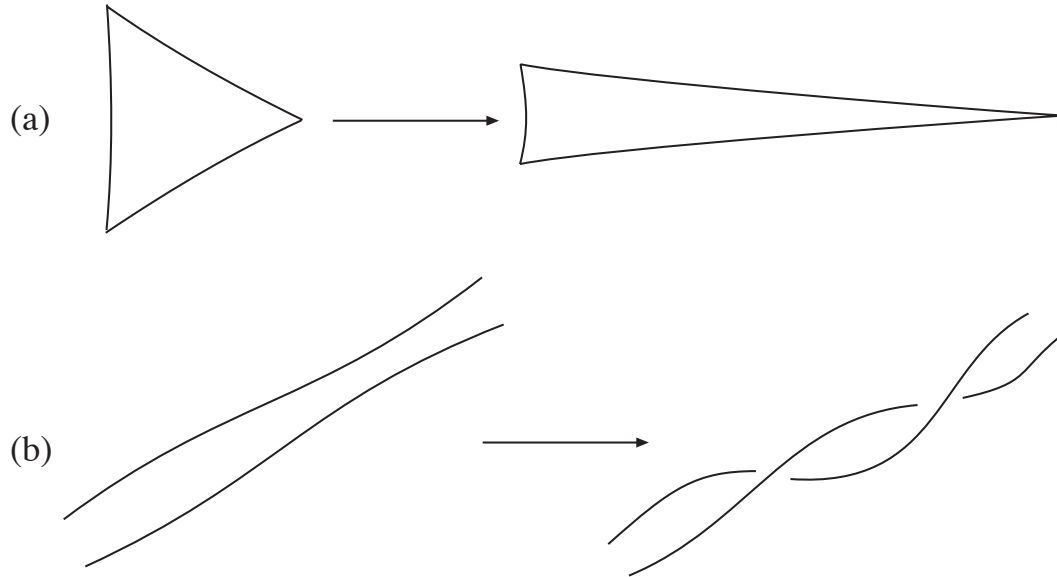


Figure 7.1: Difficulties in resolving 3D vortex sheets. (a) shows a case in which the sheet is stretched with different rates in different directions, resulting in a slender triangle. (b) shows two filaments that are almost parallel initially, but they may twist around each other at a later time.

this phenomenon schematically. Two vortex filaments are almost parallel initially, but the distance varies like a small wave. At points where they are close there is a larger tendency for them to rotate around each other, while at points where they are distant there is a less tendency for them to rotate. This non-uniformity causes the two filaments to twist around each other and makes the sheet surface difficult to resolve.

7.2 Directions of Future Work

The work presented in this thesis can be extended in a number of ways. The typical running time of our algorithm for simulations of 3D flow takes about ten hours, so there is a potential to cut the running time significantly by parallelizing the algorithm. The major part of the running time is devoted to the tree-code which evaluates the velocity, and the refinement process accounts for much less of the run-

ning time. Hence it appears that parallelizing the tree-code will be more effective in cutting the computational cost. Next we present more detailed descriptions of possible future directions of research.

7.2.1 Higher Order Quadrature

We recall that each panel has a set of active points, which are the three vertices, and a set of passive points, which are the midpoints of the edges. The three active points form a linear triangle, while active points and passive points together form a 6-point quadratic triangle. When the panel was used to compute vorticity, only the linear triangle was used and the quadrature was second-order accurate. If we use both active points and passive points, it is possible to write down a quadrature that is third-order accurate in space. This appears promising for three reasons, (1) a higher-order accurate scheme is always desirable as it allows for a smaller mesh size to be used, (2) each panel already has enough information for implementing such a higher-order scheme, and (3) the advantage of higher-order schemes was verified in Chapter III for 2D and axisymmetric flows.

In the refinement process, it is possible to do it in the following manner. Recall that when a panel is split, it breaks into four new panels. Alternatively, we may only activate a passive point on an edge only when criterion (4.24) or (4.25) is satisfied on that edge. Figure 7.2 shows a schematic of this idea. To implement it, we need to derive a quadrature for 4 and 5 point panels.

Another direction to consider is using panels with three active points and four passive points, as shown in Figure 7.3. The extra passive point is put over the centroid of the linear triangle formed by the three active points. The rationale for this is that even though the curvature on edges of the panel may be small, the curvature

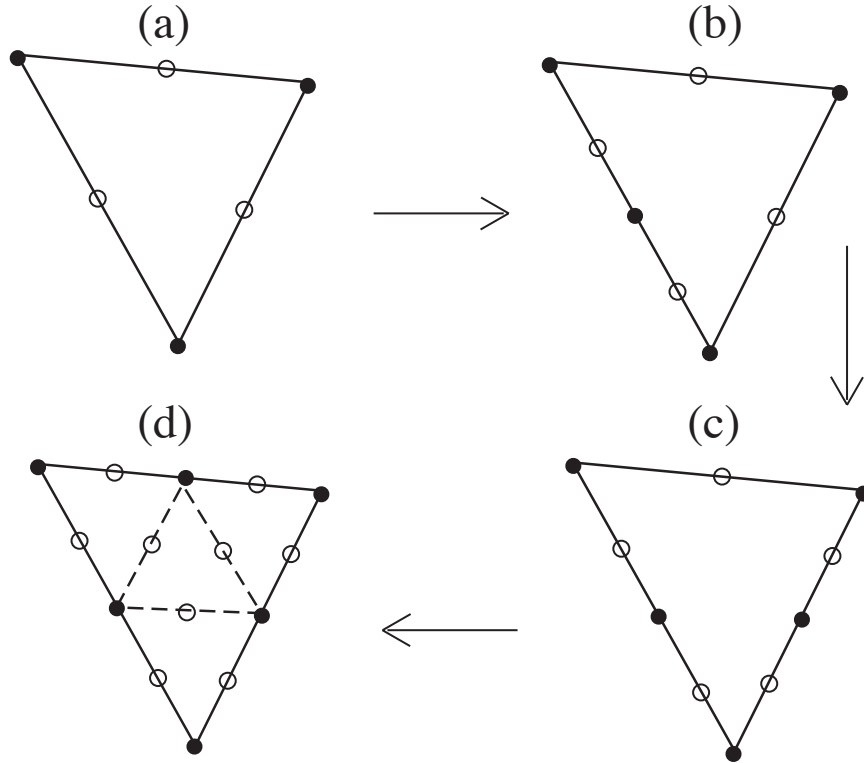


Figure 7.2: Schematic of 4 and 5-point panels. In the refinement process, we may not split a panels into 4 new panels immediately when criterion (4.24) or (4.25) is satisfied on any edge. But rather we can active a passive point when the criterion is satisfied on the corresponding edge. New quadrature schemes need to be derived for 4-point panel (b) and 5-point panel (c).

near the centroid could be large. If the distance between the centroid of the base triangle and the corresponding passive point, the panel is split into four new panels.

7.2.2 Full Density Jump for Density-Stratified Flow in 3D

For density-stratified flow, the Boussinesq approximation is only valid when the Atwood ratio is small, i.e. when the relative density jump is small. Equations governing the baroclinic generation of vorticity on the interface for the full density jump case were derived by Baker, Meiron, and Orszag [3] and presented in equation (2.31). Computational results in 2D and axisymmetric flows were presented in Chapter III for the case when full density jump is accounted for. We not that a full density jump

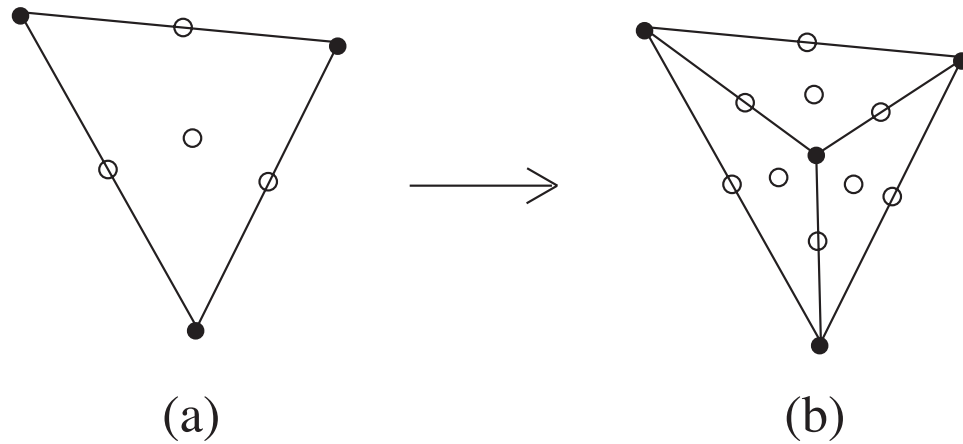


Figure 7.3: A panel with three active points and four passive points. The extra passive point corresponds to the centroid of the triangle determined by the three active points.

can also be simulated in 3D and it is more physically correct when the Atwood ratio is large. The difficulty with such a 3D computation is that without the Boussinesq approximation, since the evolution equation of the vorticity generation is implicit, it requires much more work to solve.

7.2.3 Head-on Collision of Two Vortex Rings

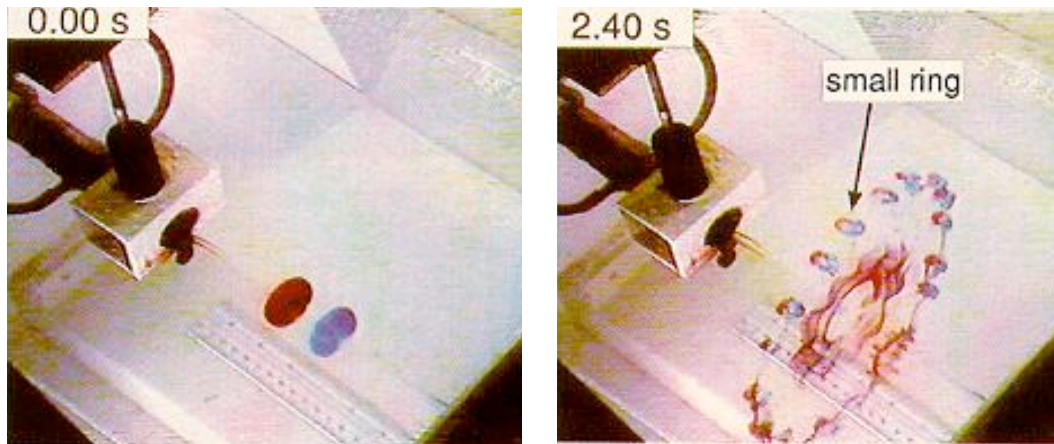


Figure 7.4: Visualization of the experiment by Lim and Nickels [31]. In the experiment, two axisymmetric vortex rings are generated by forcing fluid out of circular tubes. The two rings stay axisymmetric initially, but the axisymmetry is lost as they come into contact. After the contact, the two core axes expand rapidly and smaller rings form on the outer edge.

Figure 7.4 shows an experiment performed by Lim and Nickels [31] in which two vortex rings collide head-on. As the two rings come into contact, their core axes expand rapidly and smaller ringlets form on the outer edges. The experiment showed that different Reynolds numbers produce perceivably different results. We simulated this case and the result stays axisymmetric if no initial perturbations are added. The main difficulty here is to find perturbations so that ringlets of similar shapes form as in the experiment.

BIBLIOGRAPHY

BIBLIOGRAPHY

- [1] C.R. Anderson. A vortex method for flows with slight density variations. *J. Comput. Phys.*, 61(3):417–444, 1985.
- [2] D. Auerbach. Experiments on the trajectory and circulation of the starting vortex. *J. Fluid Mech.*, 183:185–198, 1987.
- [3] G.R. Baker, D.I. Meiron, and S.A. Orszag. Generalized vortex methods for free-surface flow problems. *J. Fluid Mech.*, 123:477–501, 1982.
- [4] G.R. Baker, D.I. Meiron, and S.A. Orszag. Boundary integral methods for axisymmetric and three-dimensional Rayleigh-Taylor instability problems. *Physica D*, 12(1-3):19–31, 1984.
- [5] J. Barnes and P. Hut. A hierarchical $O(N \log N)$ force-calculation algorithm. *Nature*, 324(6096):446–449, 1986.
- [6] G.K. Batchelor. *An Introduction to Fluid Dynamics*. Cambridge University Press, 1967.
- [7] M. Brady, A. Leonard, and D.I. Pullin. Regularized vortex sheet evolution in three dimensions. *J. Comput. Phys.*, 146(2):520–545, 1998.
- [8] R.E. Caflisch. Mathematical analysis of vortex dynamics. In R.E. Caflisch, editor, *Mathematical Aspects of Vortex Dynamics*, pages 1–24. SIAM, Philadelphia, PA, 1988.
- [9] A.J. Chorin. Numerical study of slightly viscous flow. *J. Fluid Mech.*, 57:785–796, 1973.
- [10] A.J. Chorin and P.S. Bernard. Discretization of vortex sheet, with an example of roll-up. *J. Comput. Phys.*, 13(3):423–429, 1973.
- [11] A.J. Chorin and J.E. Marsden. *A Mathematical Introduction to Fluid Mechanics*. Springer-Verlag, 1993.
- [12] G.H. Cottet and P.D. Koumoutsakos. *Vortex Methods, Theory and Practice*. Cambridge University Press, 2000.
- [13] W.J.A. Dahm, C.M. Scheil, and G. Tryggvason. Dynamics of vortex interaction with a density interface. *J. Fluid Mech.*, 205:1–43, 1989.
- [14] N. Didden. On the formation of vortex rings: rolling-up and production of circulation. *Angew. Math. Phys.*, 30(1):101–116, 1979.
- [15] C.I. Draghicescu and M. Draghicescu. A fast algorithm for vortex blob interactions. *J. Comput. Phys.*, 116(1):69–78, 1995.
- [16] P.G. Drazin. *Introduction to Hydrodynamic Stability*. Cambridge University Press, 2002.
- [17] M. Van Dyke. *An Album of Fluid Motion*. The Parabolic Press, 1982.

- [18] J. Estevadeordal, H. Meng, S.P. Gogineni, L.P. Goss, and W. Roquemore. 3-d visualization of vortex-ring and bag-shaped instabilities using holography. *Physics of Fluids*, September special section (Gallery of Fluid Motion), 1997.
- [19] T. Fohl and J.S. Turner. Colliding vortex rings. *Physics of Fluids*, 18(4):433–436, 1975.
- [20] T.N.T. Goodman and H.B. Said. A C-1 triangular interpolant suitable for scattered data interpolation. *Comm. Applied Num. Meth.*, 7(6):479–485, 1991.
- [21] L. Greengard and V. Rokhlin. A fast algorithm for particle simulations. *J. Comput. Phys.*, 73(2):325–348, 1987.
- [22] L. Kaganovskiy. *Adaptive Panel Method for Particle Simulation of Three Dimensional Vortex Sheet Motion*. PhD thesis, University of Michigan, 2006.
- [23] T. Kambe and T. Takao. Motion of distorted vortex rings. *J. Phys. Soc. Japan*, 31(2):591–599, 1971.
- [24] Y. Kaneda. A representation of the motion of a vortex sheet in a three-dimensional flow. *Physics of Fluids A*, 2(3):458–461, 1990.
- [25] J. Katz and A. Plotkin. *Low-Speed Aerodynamics*. Cambridge University Press, 2001.
- [26] R. Krasny. Desingularization of periodic vortex sheet roll-up. *J. Comput. Phys.*, 65(2):292–313, 1986.
- [27] R. Krasny and M. Nitsche. The onset of chaos in vortex sheet flow. *J. Fluid Mech.*, 454:47–69, 2002.
- [28] A. Leonard. Vortex methods for flow simulation. *J Comput. Phys.*, 37(3):289–335, 1980.
- [29] A. Leonard. Computing three-dimensional incompressible flows with vortex elements. *Ann. Rev. Fluid Mech.*, 17:523–559, 1985.
- [30] T.T. Lim. An experimental study of a vortex ring interacting with an inclined wall. *Experiments in Fluids*, 7(7):453–463, 1989.
- [31] T.T. Lim and T.B. Nickels. Instability and reconnection in the head-on collision of two vortex rings. *Nature*, 357(6375):225–227, 1992.
- [32] T.T. Lim and T.B. Nickels. *Fluid Vortices*, chapter Vortex rings, pages 95–153. Kluwer Academic Publishers, 1995.
- [33] K. Lindsay. *A Three-Dimensional Cartesian Tree-code and Applications to Vortex Sheet Roll-up*. PhD thesis, The University of Michigan, 1997.
- [34] K. Lindsay and R. Krasny. A particle method and adaptive treecode for vortex sheet motion in three-dimensional flow. *J. Comput. Phys.*, 172(2):879–907, 2001.
- [35] D.W. Moore. Spontaneous appearance of a singularity in the shape of an evolving vortex sheet. *Proc. Roy. Soc. London A*, 365(1720):105–119, 1979.
- [36] M. Nitsche. *Axisymmetric Vortex Sheet Roll-up*. PhD thesis, University of Michigan, 1992.
- [37] M. Nitsche and R. Krasny. A numerical study of vortex ring formation at the edge of a circular tube. *J. Fluid Mech.*, 276:139–161, 1994.
- [38] Y. Oshima. Head-on collision of two vortex rings. *J. Phys. Soc. Japan*, 44(1):328–331, 1978.
- [39] Y. Oshima and S. Asaka. Interaction of two vortex rings along parallel axes in air. *J. Phys. Soc. Japan*, 42(2), 1977.

- [40] Y. Oshima and N. Izutsu. Cross-linking of two vortex rings. *Physics of Fluids*, 31(9):2401–2404, 1988.
- [41] C. Pozrikidis. Theoretical and computational aspects of the self-induced motion of three-dimensional vortex sheets. *J. Fluid Mech.*, 425:335–366, 2000.
- [42] L. Rosenhead. The formation of vortices from a surface of discontinuity. *Proc. Roy. Soc. London A*, 134(823):170–192, 1931.
- [43] P.G. Saffman. *Vortex Dynamics*. Cambridge University Press, 1992.
- [44] P.R. Schatzle. *An Experimental Study of Fusion of Vortex Rings*. PhD thesis, California Institute of Technology, 1987.
- [45] K. Shariff and A. Leonard. Vortex rings. *Ann. Rev. Fluid. Mech.*, 24:235–279, 1992.
- [46] M. Stock. *A Regularized Inviscid Vortex Sheet Method for Three Dimensional Flows With Density Interfaces*. PhD thesis, University of Michigan, 2006.
- [47] G.I. Taylor. Formation of vortex ring by giving an impulse to a circular disk and then dissolving it away. *J. Applied Physics*, 24(1):104–104, 1953.
- [48] J.J. Thomson and H.F. Newall. On the formation of vortex rings by drops falling into liquids, and some allied phenomena. *Proc. Roy. Soc. Ser. A*, 39:417–436, 1885.
- [49] G. Tryggvason, W.J.A. Dahm, and K. Sbeih. Fine structure of vortex sheet rollup by viscous and inviscid simulations. *J. Fluids Eng.*, 113(1):31–36, 1991.
- [50] J.H. Walther and P. Koumoutsakos. Three-dimensional vortex methods for particle-laden flows with two-way coupling. *J. Comput. Phys.*, 167(1):39–71, 2001.
- [51] F. Zhao. An $O(N)$ algorithm for three dimensional N -body simulation. Master’s thesis, Massachusetts Institute of Technology, 1987.